

10

Classical Treatments of Line Transfer

In this chapter we discuss some of the early approaches to the line-formation problem; these provide background for the more modern treatments to be presented in following chapters. A fuller discussion of these older methods and of their application to stellar spectra can be found in (684, Chap. 7; 638, Chaps. 15–17; 15, Chaps. 12–16; 11, Chap. 8; 256, Chaps. 14–16). It is essential to be familiar with such methods because of the large body of literature based upon them. More important, one must understand the physical basis of the classical treatments in order to evaluate the reliability of spectroscopic diagnostics derived from them, and to realize the conceptual differences inherent in recent work.

10-1 Characterization of the Problem

In the usual classical approach one notes, at the outset, the existence of two different line-formation processes: scattering and absorption. We have discussed these two categories in Chapter 2, and described there the physical differences between them. It is usually supposed that a fraction $(1 - \varepsilon)$ of the

photons absorbed are simply *scattered* so that the excited electron returns directly to its original lower level, and normally it is assumed that the scattering is *isotropic* and *coherent* (actually *complete redistribution* is a much better approximation). Then the scattering contribution to the emission coefficient is

$$\eta_v^s = (1 - \varepsilon)\chi_i\phi_v J_v \quad (10-1)$$

$$\text{where } \chi_i = (\pi e^2/mc)f_{ij}[n_i - (g_i/g_j)n_j] \quad (10-2)$$

is the line absorption coefficient in the transition between levels i and j . The remaining fraction ε of the photons is assumed to be *destroyed* and converted to thermal energy by various processes (cf. §2-1). One then argues that this loss into the thermal pool must be balanced exactly by *thermal emission*, which contributes to the total emission coefficient an amount

$$\eta_v' = \varepsilon\chi_i\phi_v B_v(T) \quad (10-3)$$

In the limit of strict LTE, $\varepsilon \equiv 1$, and all the emission is thermal.

In addition, there are contributions to the opacity and emissivity from continuum thermal processes and electron scattering. Thus the transfer equation is

$$\mu(\partial I_v/\partial z) = -(\kappa_c + \sigma + \chi_i\phi_v)I_v + \kappa_c B_v + \sigma J_v + \varepsilon\chi_i\phi_v B_v + (1 - \varepsilon)\chi_i\phi_v J_v \quad (10-4)$$

We have ignored the v -dependence of κ_c and σ because most lines are so narrow that these coefficients vary only negligibly over the line in comparison with the swift variation of ϕ_v . If we write $d\tau_v \equiv -(\kappa_c + \sigma + \chi_i\phi_v)dz$, and let $\rho \equiv \sigma/(\kappa_c + \sigma)$, and

$$\beta_v \equiv \chi_i\phi_v/(\kappa_c + \sigma) \quad (10-5)$$

we have

$$\mu(\partial I_v/\partial \tau_v) = I_v - \{(1 - \rho) + \varepsilon\beta_v\}B_v + [\rho + (1 - \varepsilon)\beta_v]J_v/(1 + \beta_v) \quad (10-6)$$

Or, defining

$$\lambda_v \equiv [(1 - \rho) + \varepsilon\beta_v]/(1 + \beta_v) \quad (10-7)$$

the transfer equation becomes

$$\mu(\partial I_v/\partial \tau_v) = I_v - \lambda_v B_v - (1 - \lambda_v)J_v \quad (10-8)$$

E. A. Milne and A. S. Eddington developed equation (10-8) as an approximation to the line-transfer problem, and customarily it bears their name.

Excellent discussions of the physical implications of this equation have been given by Milne (416, p. 169ff) and Strömgren (613).

From a physical point of view, equation (10-8) provides a rather severe idealization of line formation and may be criticized on several counts. (1) Line-scattering is not, in fact, coherent. This inadequacy is overcome if we write, instead of equation (10-8),

$$\mu \left(\frac{\partial I_v}{\partial \tau_v} \right) = I_v - \lambda_v B_v - \frac{\rho J_v}{1 + \beta_v} - \frac{(1 - \varepsilon)\beta_v}{(1 + \beta_v)\phi_v} \int R(v', v) J_{v'} dv' \quad (10-9)$$

where $R(v', v)$ is an appropriate redistribution function (cf. §2-1 and Chap. 13). (2) To solve equations (10-8) or (10-9), both the parameter ε and the occupation numbers n_i and n_j must be known. In classical treatments it is often assumed that LTE holds, so that $\varepsilon = 1$ and $n_i = n_i^*$, $n_j = n_j^*$. It must be stressed, however, that this merely an *assumption* and, as will be seen in Chapters 11 and 12, the assumption is often unjustified and may yield results seriously in error. In many treatments, an ad hoc value is chosen for ε , but the occupation numbers are still assumed to have their LTE values. Such an approach is internally *inconsistent*, for when scattering occurs in a line, the level-populations depend upon the radiation field via the equations of statistical equilibrium. (3) An equation of the form of (10-8) was derived by Milne for a strict two-level atom, and his analysis yields a unique (and correct) value for the parameter ε (416, pp. 172–178). However, as mentioned above, coherent scattering is *not* an accurate approximation. More important, analysis of the equations of statistical equilibrium for general (i.e., multilevel) atomic models shows (cf. Chapters 11 and 12) that other *kinds* of terms appear in the source function; these may depend upon the radiation fields in *other* transitions (continua and lines), and thus in principle couple *all* the lines in the spectrum together. In short, both equations (10-8) and (10-9) are seriously incomplete from a physical point of view, and this should be borne in mind during the discussion that follows in this chapter.

10-2 The Milne–Eddington Model

DEFINITION

Let us now consider the Milne–Eddington equation [equation (10-8)] under the simplifying assumptions that λ_v , ε , and ρ are all constant with depth, and that the Planck function B_v is a linear function on the continuum optical depth scale τ ; i.e.,

$$B_v = a + b\tau = a + [b\tau_v/(1 + \beta_v)] \equiv a + p_v\tau_v \quad (10-10)$$

Under these conditions an *exact* solution may be obtained (158) but this differs only slightly from the approximate solution derived below.

Taking the zero-order moment of equation (10-8) we find

$$(dH_v/d\tau_v) = J_v - (1 - \lambda_v)J_v - \lambda_v B_v = \lambda_v(J_v - B_v) \quad (10-11)$$

Aside from the definition of λ_v , equation (10-11) is the same as equation (6-4), and from the analysis in §6-1 we know that the solution, in the Eddington approximation, is

$$J_v = a + p_v\tau_v + (p_v - \sqrt{3}a) \exp[-(3\lambda_v)^{\frac{1}{2}}\tau_v]/[\sqrt{3} + (3\lambda_v)^{\frac{1}{2}}] \quad (10-12)$$

and the emergent flux is

$$H_v(0) = (3)^{-\frac{1}{2}} J_v(0) = \frac{1}{3} [p_v + (3\lambda_v)^{\frac{1}{2}}a]/(1 + \lambda_v^{\frac{1}{2}}) \quad (10-13)$$

Equation (10-12) shows that *thermalization* ($J_v \rightarrow B_v$) occurs only at depths of the order of $\lambda_v^{-\frac{1}{2}}$. Recalling the definition of λ_v , we see that this depth is $(1 - \rho)^{-\frac{1}{2}}$ in the continuum ($\beta_v = 0$), and $\varepsilon^{-\frac{1}{2}}$ in a strong line ($\beta_v \rightarrow \infty$). In both cases thermalization occurs at a depth $p^{-\frac{1}{2}}$, where p is the probability that a photon is destroyed and converted to thermal energy each time it interacts with the material; these results are compatible with the random-walk arguments given in Chapter 6. Note that these results apply only for *coherent* scattering (cf. Chapter 11).

Equation (10-13) may be used to compute the profile of a line in a stellar atmosphere. In the continuum, $\beta_v = 0$; then $\lambda_v = (1 - \rho)$, and the *continuum flux* is

$$H_c(0) = \frac{1}{3} [b + a\sqrt{3(1 - \rho)}]/[1 + (1 - \rho)^{\frac{1}{2}}] \quad (10-14)$$

Thus the *residual flux* in the line is, by equation (8-2),

$$R_v = \left[\frac{p_v + (3\lambda_v)^{\frac{1}{2}}a}{1 + \lambda_v^{\frac{1}{2}}} \right] \left[\frac{1 + (1 - \rho)^{\frac{1}{2}}}{b + a\sqrt{3(1 - \rho)}} \right] \quad (10-15)$$

There are four important results that can be derived from this classical theory, which provided the conceptual orientation of much of the early work on line formation. Let us now examine these briefly.

SCATTERING LINES

Consider the case where $\rho = 0$, so that there is no scattering in the continuum. Further, suppose that $\varepsilon = 0$, so that there is pure scattering in the

lines. Then $\lambda_v = (1 + \beta_v)^{-1}$ and the residual flux in the line is

$$R_v = 2 \left[\frac{b}{1 + \beta_v} + a \left(\frac{3}{1 + \beta_v} \right)^{\frac{1}{2}} \right] \left[\left(1 + \sqrt{\frac{1}{1 + \beta_v}} \right) (\sqrt{3}a + b) \right]^{-1} \quad (10-16)$$

If we consider the case of a very strong line and take the limit $\beta_v \rightarrow \infty$, we obtain $R_v = H_v(0)/H_c(0) = 0$, which shows that the core of a very strong line formed by scattering can be completely dark; this result is in contrast to the case of a line formed by absorption, as is shown below.

Exercise 10-1: Writing $\beta_v = \beta_0 H(a, v)$, where H denotes the usual Voigt function, plot residual flux profiles from equation (10-16) for scattering lines with $\beta_0 = 1, 10, 100, 1000, 10^4$, and $(b/a) = 1, 2$, and 3, assuming $a = 10^{-3}$.

Exercise 10-2: In the Schuster-Schwarzschild model, the lines are assumed to be confined to a finite layer (the "reversing layer") of thickness t_v , illuminated from below by an incident intensity I_0 . In the reversing layer the continuum opacity is zero, and the lines are pure scatterers. Using the two-stream approximation ($I \equiv I^+$ for $0 \leq \mu \leq 1$; $I \equiv I^-$ for $-1 \leq \mu \leq 0$; and $\mu = \pm \frac{1}{2}$ in the transfer equation) show that (a) $H_v \equiv \frac{1}{2}(I_v^+ - I_v^-) = \text{constant} = \frac{1}{2}I_0/(1 + t_v)$, and (b) $J_v(t_v) = H_v(1 + 2t_v)$, $0 \leq t_v \leq t_v$.

ABSORPTION LINES

Again assume $\rho = 0$, but now set $\varepsilon = 1$ (LTE in the line); then $\lambda_v \equiv 1$, and

$$R_v = [\sqrt{3}a + b(1 + \beta_v)^{-1}] / (\sqrt{3}a + b) \quad (10-17)$$

In this case, as $\beta_v \rightarrow \infty$, the flux in the line does *not* go to zero, but approaches a finite value

$$R_0 = R_v(\varepsilon = 1, \beta_v \rightarrow \infty) = [1 + (b/\sqrt{3}a)]^{-1} \quad (10-18)$$

This is to be expected, for as $\beta_v \rightarrow \infty$, only the surface layers of the star are seen, and the emergent flux is then determined by the surface value of the Planck function, which will be nonzero. In contrast, in the scattering case, photons are constantly diverted out of the pencil of radiation, and in the limit $\beta_v \rightarrow \infty$, none survive to emerge at the surface.

Exercise 10-3: Repeat exercise 10-1 for an absorption line, using equation (10-17).

It is convenient to re-express equations (10-17) and (10-18) in terms of the Planck function and its gradient. Assume that on a *mean* optical depth scale,

$$B_v(\bar{\tau}) = B_v(T_0) + (\partial B_v / \partial \bar{\tau})_0 \bar{\tau} \equiv B_0 + B_1 \bar{\tau} \quad (10-19)$$

Using the Eddington-approximation result for the grey temperature distribution, namely $T^4 = T_0^4(1 + \frac{3}{2}\bar{\tau})$, it is easy to show that

$$B_1 = \frac{3}{8} X_0 B_0 \quad (10-20)$$

where

$$X_0 \equiv u_0 / (1 - e^{-u_0}) \quad (10-21)$$

and $u_0 \equiv (hv/kT_0)$. Thus the parameters in equation (10-10) are: $a \equiv B_0$,

$$b = \frac{3}{8} X_0 B_0 (\bar{\kappa}/\kappa) \quad (10-22)$$

$$\text{and } p_v = \frac{3}{8} X_0 B_0 (\bar{\kappa}/\kappa) / (1 + \beta_v) \quad (10-23)$$

where $\bar{\kappa}$ and κ are the mean opacity, and the monochromatic continuum opacity at the line wavelength, respectively. Then equation (10-18) becomes

$$R_0 = \{1 + [\sqrt{3}X_0(\bar{\kappa}/\kappa)/8]\}^{-1} \quad (10-24)$$

Exercise 10-4: Derive equations (10-20) through (10-23).

For the sun, $T_0 \sim 4800^\circ\text{K}$ from a grey model, and if we choose $\lambda = 5000 \text{ \AA}$, then $u_0 \sim 6$, $X_0 \sim 6$, and $\kappa \approx \bar{\kappa}$, so that equation (10-24) predicts

$$R_0 = \left(1 + \frac{3}{4} \sqrt{3} \right)^{-1} = 0.44 \quad (10-25)$$

This value is in fair agreement with the depths of many of the stronger lines observed in that region of the solar spectrum. Some lines, however, are much deeper, particularly resonance lines such as the sodium D-lines; this fact led to the conceptual identification of resonance lines as "scattering" lines and subordinate lines (e.g., $H\alpha$) as "absorption" lines. It was believed that the central intensities of the latter group reflected information about the surface temperature of the atmosphere. Such a division of lines into two groups is intuitively not unreasonable, for we expect that in a resonance line the most probable route of exit from the upper state is, in fact, a direct decay to the lower state. In contrast, for subordinate lines a large number of possibilities will, in general, exist, and the photons may effectively be removed from the line and destroyed. It must be emphasized, however, that this characterization is only schematic and often does violence to the actual physics of line-formation. For example, we shall find in Chapter 11 that the boundary value

of the source function of the $H\alpha$ line (a subordinate line) has essentially nothing to do with the temperature of the outer atmospheric layers.

CENTER-TO-LIMB VARIATION

The specific intensity emergent at frequency ν , on the disk at an angle $\theta = \cos^{-1} \mu$ from disk center, is given by

$$\begin{aligned} I_\nu(0, \mu) &= \int_0^\infty S_\nu(\tau_\nu) e^{-(\tau_\nu/\mu)} \mu^{-1} d\tau_\nu \\ &= \int_0^\infty [B_\nu + (1 - \lambda_\nu)(J_\nu - B_\nu)] \exp(-\tau_\nu/\mu) \mu^{-1} d\tau_\nu \quad (10-26) \end{aligned}$$

where the form of S_ν has been taken from equation (10-8). Substituting from equation (10-12) we find

$$I_\nu(0, \mu) = (a + p_\nu \mu) + \left[\frac{(p_\nu - \sqrt{3}a)(1 - \lambda_\nu)}{\sqrt{3}(1 + \sqrt{\lambda_\nu})(1 + \sqrt{3}\lambda_\nu\mu)} \right] \quad (10-27)$$

In the continuum, $\beta_\nu = 0$, and again taking $p = 0$,

$$I_c(0, \mu) = a + b\mu \quad (10-28)$$

The residual intensity $r_\nu(\mu) \equiv I_\nu(0, \mu)/I_c(0, \mu)$ and the absorption depth $a_\nu(\mu) = 1 - r_\nu(\mu)$ follow immediately from equations (10-27) and (10-28).

Consider first a pure absorption line, for which $\varepsilon = 1$ and $\lambda_\nu \equiv 1$. Then

$$r_\nu(\mu) = [1 + (b/a)\mu/(1 + \beta_\nu)]/[1 + (b/a)\mu] \quad (10-29)$$

Here we see that as the limb is approached (i.e., as $\mu \rightarrow 0$), $I_\nu \rightarrow I_c$, and the line vanishes. This is compatible with the physical picture sketched above, for as the limb is reached, only the very surface can be seen at any frequency. For $\varepsilon = 1$, the same source function (the surface value of the Planck function) is observed throughout the profile, and the contrast between line and continuum disappears. On the other hand, if $\varepsilon = 0$ (a pure scattering line), $\lambda_\nu = (1 + \beta_\nu)^{-1}$, and taking the limit as $\beta_\nu \rightarrow \infty$, equation (10-27) reduces to $I_\nu(0, \mu) \equiv 0$ for all μ 's; thus the cores of pure scattering lines always remain dark, even at the limb, and there is a clear distinction between the center-to-limb behavior of absorption and scattering lines. A few representative values of the variation of line-depth with disk-position are given in Table 10-1 for several values of ε and β_ν . In this table $(b/a) = 3$; negative values imply emission, and are an artifact of the approximations made in solving the transfer equation.

TABLE 10-1
Center-to-Limb Variation in the Milne-Eddington Model

ε	β_ν	$a_\nu(\mu)$					A_ν (Flux)
		$\mu = 1$	0.5	0.3	0		
1.0	0.01	0.007	0.006	0.005	0.000	0.006	
	0.1	0.068	0.055	0.043	0.000	0.058	
	1.0	0.375	0.300	0.237	0.000	0.317	
	10.0	0.682	0.545	0.431	0.000	0.576	
	100.0	0.743	0.594	0.469	0.000	0.628	
	∞	0.750	0.600	0.474	0.000	0.634	
0.3	0.01	0.007	0.005	0.004	-0.002	0.006	
	0.1	0.066	0.051	0.037	-0.019	0.054	
	1.0	0.378	0.306	0.246	0.026	0.322	
	10.0	0.723	0.633	0.565	0.334	0.653	
	100.0	0.798	0.713	0.648	0.438	0.731	
	∞	0.808	0.723	0.659	0.452	0.741	
0.1	0.01	0.007	0.005	0.004	-0.003	0.006	
	0.1	0.066	0.049	0.035	-0.024	0.053	
	1.0	0.379	0.308	0.250	0.035	0.324	
	10.0	0.751	0.687	0.639	0.483	0.700	
	100.0	0.847	0.799	0.765	0.658	0.809	
	∞	0.860	0.815	0.783	0.684	0.824	
0.0	0.01	0.007	0.005	0.003	-0.004	0.006	
	0.1	0.066	0.049	0.034	-0.027	0.053	
	1.0	0.379	0.310	0.252	0.039	0.325	
	10.0	0.778	0.732	0.698	0.589	0.742	
	100.0	0.931	0.920	0.912	0.885	0.922	
	∞	1.000	1.000	1.000	1.000	1.000	

In the solar spectrum, some lines do weaken towards the limb while others do not, or weaken only slightly. This observed behavior again led to the classification of lines into "absorption" or "scattering" categories, though in some cases the categorization made on the basis of limb-darkening was in conflict with that based on central intensities. Furthermore, some studies [e.g., that by Houtgast, reviewed in (596)] have shown that neither category is adequate because in some lines the effects of noncoherent scattering dominate. In short, the approach described here is quite schematic, and one must recognize that it simply does not contain much of the essential physics.

SCHUSTER MECHANISM

In the above discussion, the continuum has been assumed to be purely thermal. When continuum scattering is taken into account, several interesting

effects are found; these were first discussed by Schuster in one of the fundamental papers of radiative transfer theory (562). To emphasize the role of continuum scattering, set $\rho = 1$ (a realistic value for, say, O-stars); then $\lambda_v = \varepsilon\beta_v/(1 + \beta_v)$ and equation (10-15) becomes

$$R_v = \left[\frac{1}{1 + \beta_v} + \left(\frac{a}{b} \right) \left(\frac{3\varepsilon\beta_v}{1 + \beta_v} \right)^{\frac{1}{2}} \right] \left[1 + \left(\frac{\varepsilon\beta_v}{1 + \beta_v} \right)^{\frac{1}{2}} \right]^{-1} \quad (10-30)$$

First, consider the case with $\varepsilon = 0$; then $R_v = 1/(1 + \beta_v)$, and the line is a pure absorption feature. This occurs because both the lines and continuum are formed by scattering, and the scattering length in the line is larger. On the other hand, suppose $\varepsilon = 1$; then it is obvious from equation (10-30) that in the line core, as $\beta_v \rightarrow \infty$, $R_v \rightarrow (\sqrt{3}a/2b)$. Thus the line can appear in absorption or emission depending on the ratio (a/b) ; the more shallow the temperature gradient (i.e., the smaller the value of b), the brighter is the line compared to the continuum. The reason for this is that because $\varepsilon = 1$, the source function in the line is everywhere equal to the thermal value while, in the continuum, scattering causes J_v (and thus S_v) to drop below B_v .

If (a/b) is greater than the critical value $(a/b) = 2/\sqrt{3}$, the line is in emission for all values of β_v (i.e., at all frequencies in the profile). If (a/b) just equals the critical value, then both the extreme wing ($\beta_v \rightarrow 0$) and the very core of the line ($\beta_v \rightarrow \infty$) lie at the level of the continuum, and all other points in the profile are in emission. If (a/b) is less than the critical value the line may have weak emission wings and a central reversal into an absorption core. If $(a/b) < 1/\sqrt{3}$, the line is everywhere in absorption.

This interplay of scattering and absorption, which gives rise to either absorption or emission lines depending on the temperature gradient, is known as the *Schuster mechanism*; a thorough discussion of the various possible cases was given by Schuster himself (562). From time to time it has been suggested that this mechanism could be responsible for emission lines observed in certain early-type spectra, but on the basis of recent critical discussions (238; 280) this seems unlikely.

10-3 The Theoretical Curve of Growth

Using equation (10-15) one could, in principle, compute the profile of a spectrum line and, by integration over frequency, determine its equivalent width. Such a procedure is laborious, however, and requires the use of a computer. It is instructive, therefore, to consider a simple model that allows the equivalent width to be computed analytically. In this way we can construct what is known as a *curve of growth*, which gives the equivalent width directly in terms of the number of absorbing atoms that produce the line.

To begin with, we assume that the line formation occurs in a layer to which we can assign a unique temperature and electron pressure. This assumption is normally valid in laboratory work, but in the stellar-atmospheres situation there are usually strong gradients in both temperature and pressure. Thus the choice of an appropriate temperature and pressure is difficult and, at best, can refer only to some ill-defined mean value in the line-forming region. Having made this choice, we can compute (assuming LTE) the populations of the atomic levels and, hence, the continuous opacity κ_c and the line opacity in a transition ($i \rightarrow j$),

$$\chi_{ij}(v) = (\pi e^2/mc) f_{ij} n_i^* (1 - e^{-hv/kT}) \phi_v \equiv \chi_{ij} \phi_v \quad (10-31)$$

The line profile is assumed to be given by the Voigt function [equation (9-34)]

$$H(a, v) = (a/\pi) \int_{-\infty}^{\infty} e^{-y^2} [(v - y)^2 + a^2]^{-1} dy$$

where $v \equiv \Delta v/\Delta v_D$, $a \equiv \Gamma/(4\pi \Delta v_D)$, and $\Delta v_D = v\xi_0/c$; here ξ_0 is the most probable velocity of the atoms in the material. We then write $\chi_{ij}(v) = \chi_0 H(a, v)$ where $\chi_0 \equiv \chi_{ij}/(\pi^{\frac{1}{2}} \Delta v_D)$. We assume that both Δv_D and the parameter a are fixed in the region of line-formation, and employ the Milne-Eddington model in which the ratio $\beta_v \equiv \chi_{ij}(v)/\kappa_c$ is independent of depth. (The assumption of depth-independent β_v is actually a fairly good approximation for some spectrum lines; e.g., Mg II $\lambda\lambda 4481$ and Si II $\lambda\lambda 4128, 4131$. Indeed for these lines both χ_0 and κ_c may vary over orders of magnitude in the atmosphere while their ratio remains nearly constant.) Finally, we assume the line is formed by absorption processes in LTE; the flux is then easily computed as

$$F_v = 2 \int_0^{\infty} B_v [T(\tau)] E_2 \left[\int_0^{\tau} (1 + \beta_v) d\tau \right] (1 + \beta_v) d\tau \quad (10-32)$$

As before, we adopt $B_v[T(\tau)] = B_0 + B_1\tau$, where τ is the continuum optical depth. Then, having taken β_v to be constant with depth, we have

$$\begin{aligned} F_v &= 2 \int_0^{\infty} (B_0 + B_1\tau) E_2[(1 + \beta_v)\tau](1 + \beta_v) d\tau \\ &= B_0 + \frac{2}{3} B_1/(1 + \beta_v) \end{aligned} \quad (10-33)$$

From equation (10-33) the continuum flux is clearly $F_c = B_0 + \frac{2}{3}B_1$, so that the line-depth in the flux profile is

$$A_v = [\beta_v/(1 + \beta_v)] \left[1 + \frac{3}{2} (B_0/B_1) \right]^{-1} \quad (10-34)$$

It is convenient to work in terms of the parameter A_0 , the central depth of an infinitely opaque line. Taking the limit of equation (10-34) as $\beta_v \rightarrow \infty$ we find

$$A_0 = \left[1 + \frac{3}{2} \left(B_0/B_1 \right) \right]^{-1} \quad (10-35)$$

which is essentially the result stated in equation (10-18). Then equation (10-34) may be rewritten

$$A_v = A_0 \beta_v / (1 + \beta_v) \quad (10-36)$$

The *equivalent width* may now be computed by integration of the line-depth over frequency to obtain

$$W_v = \int_0^\infty A_v dv = 2A_0 \Delta v_D \int_0^\infty \beta(v) [1 + \beta(v)]^{-1} dv \quad (10-37)$$

where it has been assumed that the line is symmetrical about its center. But $\beta(v) = (\chi_0/\kappa_c)H(a, v) \equiv \beta_0 H(a, v)$, and if we define the *reduced equivalent width* $W^* \equiv W/(2A_0 \Delta v_D)$, we have

$$W^*(a, \beta_0) = \int_0^\infty \beta_0 H(a, v) [1 + \beta_0 H(a, v)]^{-1} dv \quad (10-38)$$

Before we attempt to evaluate this integral, let us consider qualitatively how the line develops as more and more atoms absorb. At the start, with only a few absorbers, each will be able to remove photons from the radiation field, and the line strength should be proportional to the number of absorbing atoms. Only the Doppler core (where the opacity is highest) will contribute to the line strength; the line wings will be transparent and will not reduce the emitted flux. As yet more atoms absorb in the line, the core, at some point, becomes completely opaque, and the intensity there reaches its limiting value given by equation (10-35). Now, essentially all the photons that can be absorbed in the core already have been, and so long as the line-wings remain transparent, the addition of more absorbers does little to increase the equivalent width of the line, which is said to be *saturated*. Finally, when enough absorbers are present, the opacity in the wings becomes appreciable, and the equivalent width again increases as the contribution of the line wings grows. These different behaviors are shown in Figure 10-1. On the basis of the above discussion, we see that there are three basically distinct regimes in the curve of growth; these will be treated individually.

The Voigt profile can be represented schematically [equation (9-45)] as $H(a, v) \sim e^{-v^2} + \pi^{-\frac{1}{2}} a v^{-2}$; here it is assumed that the first term applies only in the core for $v \leq v^*$, and the second only in the wings for $v \geq v^*$, where v^* is chosen as the transition point where the two terms are equal.

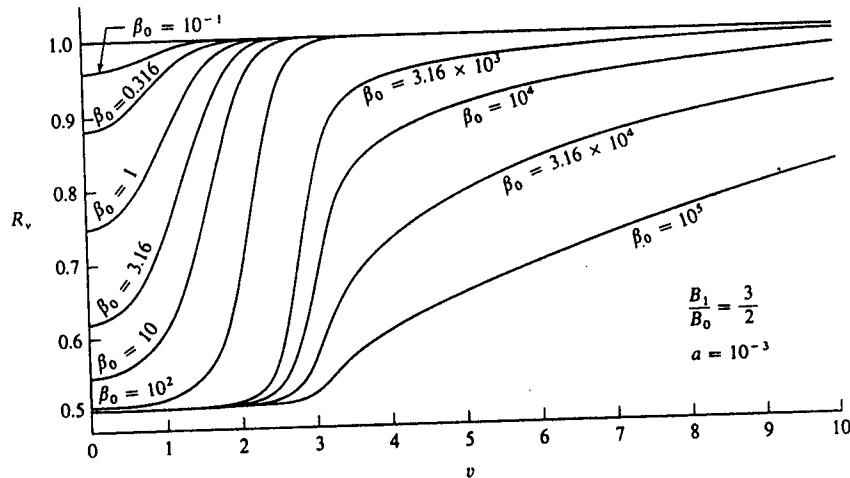


FIGURE 10-1
Development of a spectrum line with increasing number of atoms along the line of sight. The line is assumed to be formed in pure absorption. For $\beta_0 \lesssim 1$, the line strength is directly proportional to the number of absorbers. For $30 \lesssim \beta_0 \lesssim 10^3$ the line is saturated, but the wings have not yet begun to develop. For $\beta_0 \gtrsim 10^4$ the line wings are strong and contribute most of the equivalent width.

Consider now the contribution from the core only, and write $\beta(v) = \beta_0 e^{-v^2}$, assuming that $\beta_0 < 1$. Then equation (10-38) becomes

$$\begin{aligned} W^* &= \beta_0 \int_0^\infty e^{-v^2} [1 + \beta_0 e^{-v^2}]^{-1} dv \\ &= \beta_0 \int_0^\infty e^{-v^2} (1 - \beta_0 e^{-v^2} + \dots) dv \end{aligned} \quad (10-39)$$

$$\text{or } W^* = \frac{1}{2} \pi^{\frac{1}{2}} \beta_0 [1 - (\beta_0/\sqrt{2}) + (\beta_0^2/\sqrt{3}) - \dots] \quad (10-40)$$

For small values of β_0 (weak lines) the linear term dominates, and the equivalent width of the line is directly proportional to the number of absorbers present. This is known as the *linear part* of the curve of growth. Note that β_0 varies as Δv_D^{-1} , as does W^* , hence the equivalent width W is *independent* of Δv_D on the linear part of the curve.

In the *saturation part* of the curve of growth, β_0 is so large that the line core has reached its limiting depth, but not yet large enough that the line wings contribute to the equivalent width. Again $\beta(v) = \beta_0 e^{-v^2}$, and if we

let $u = v^2$, then $dv = \frac{1}{2}u^{-\frac{1}{2}}du$, and equation (10-38) becomes

$$\begin{aligned} W^* &= \frac{1}{2} \int_0^\infty \beta_0 e^{-u} (1 + \beta_0 e^{-u})^{-1} u^{-\frac{1}{2}} du \\ &= \frac{1}{2} \int_0^\infty (1 + e^{u-a})^{-1} u^{-\frac{1}{2}} du \end{aligned} \quad (10-41)$$

where we have set $\beta_0 = e^a$. This integral may be rewritten [see (160, 389)] as

$$2W^* = \int_0^a u^{-\frac{1}{2}} du + a \int_0^\infty \frac{[\alpha(1+t)]^{\frac{1}{2}} dt}{1 + e^{\alpha t}} - \alpha \int_0^a \frac{[\alpha(1-t)]^{\frac{1}{2}} dt}{1 + e^{\alpha t}} \quad (10-42)$$

Following Sommerfeld, one may replace the upper limit in the third integral by ∞ (because $\alpha \gg 1$) and expand $[\alpha(1+t)]^{\frac{1}{2}}$ as a power series in t around $t = 0$. The results may be written in closed form in terms of the Riemann zeta function, and one obtains finally the asymptotic expression

$$W^* \approx \sqrt{\ln \beta_0} \{1 - [\pi^2/24(\ln \beta_0)^2] - [7\pi^4/384(\ln \beta_0)^4] - \dots\} \quad (10-43)$$

The above expansion is only semiconvergent and must always be truncated after a finite number of terms; in practice, the series is useful for $\beta_0 \gtrsim 55$. From equation (10-43) we can see clearly that on the *saturation*, or *flat*, part of the curve of growth, the equivalent width grows extremely slowly with increasing numbers of absorbers, namely $W^* \propto \sqrt{\ln \beta_0}$. The weak dependence of W^* on β_0 implies that W on this part of the curve is essentially proportional to Δv_D . It is easy to understand why this should be so: the *depth* of the line profile is fixed at A_0 , hence the integrated absorption must be proportional to the linewidth; i.e., to Δv_D (cf. Figure 10-1). Similarly the dependence of W on β_0 can be understood by recognizing that to produce a significant depression in the continuum, the optical depth in the line must exceed unity before the continuum reaches unit optical depth. This occurs at frequencies $v < v_0$ where $\beta_0 e^{-v_0^2} \approx 1$; clearly v_0 , which measures the width of the dark core (and hence determines W^*), varies as $\sqrt{\ln \beta_0}$.

Finally, for very large numbers of absorbers, the line wings become opaque enough to provide the dominant contribution to the equivalent width. Here we adopt $H(a, v) \sim a/(\pi^2 v^2)$, and writing $C \equiv \beta_0 a \pi^{-\frac{1}{2}}$ we find from equation (10-38)

$$W^* = \int_0^\infty (1 + v^2/C)^{-1} dv = \frac{1}{2} \pi \sqrt{C} = \frac{1}{2} (\pi a \beta_0)^{\frac{1}{2}} \quad (10-44)$$

Thus $W \propto \beta_0^{\frac{1}{2}}$, giving rise to what is called the *damping* or *square-root* part of the curve of growth. Again, note that both a and β_0 each contain a factor of Δv_D ; hence W is independent of Δv_D on this part of the curve.

The entire curve of growth is shown in Figure 10-2. Notice that the larger the value of the damping parameter a , the sooner the wings dominate W ,

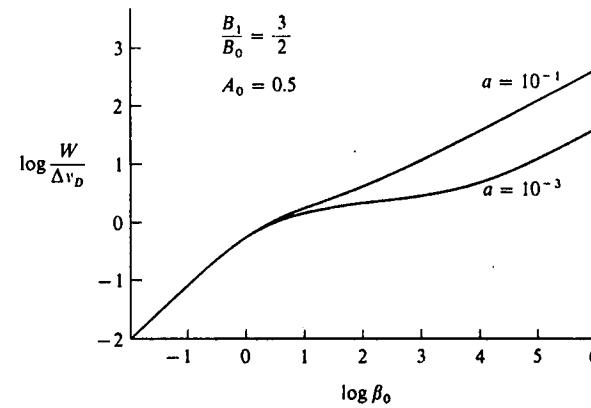


FIGURE 10-2
Curves of growth for pure absorption lines. Note that the larger the value of a , the sooner the square-root part of the curve rises away from the flat part.

and hence the sooner the damping part of the curve rises away from the flat part. Numerous curves of growth have been computed by various authors. A particularly useful set has been published by Wrubel for a wide range of the temperature-distribution parameters B_0 and B_1 , and under different assumptions concerning the atmospheric model (i.e., Milne-Eddington or Schuster-Schwarzschild) and the transfer problem (i.e., absorption or scattering lines); see (687; 688; 689).

10-4 The Empirical Curve of Growth

The curve of growth has long been one of the astronomer's favorite tools for performing an analysis of a stellar atmosphere, and the literature of the various applications of this approach is enormous. The reasons for the popularity of the curve of growth are that it provides estimates of several key parameters with speed and ease, and that it makes use of equivalent widths alone, which can be well-determined observationally even for faint stars where profiles would be impossible to measure accurately.

As described in §10-3, the theoretical curve of growth gives $\log(W/\Delta v_D) = \log(W_\lambda/\Delta \lambda_D) = \log(W_\lambda c/\lambda \xi_0)$ as a function of $\log \beta_0$. Here ξ_0 is the total random velocity of the atoms forming the line, and

$$\beta_0 = \frac{\xi_0}{\kappa_c} = \left(\frac{\pi^{\frac{1}{2}} e^2 f}{mc \Delta v_D} \right) \frac{n_{ijk}^*(1 - e^{-hv/kT})}{k_c(1 - e^{-hv/kT})} = \left(\frac{\pi^{\frac{1}{2}} e^2}{mc} \right) (f \lambda) \left(\frac{n_{ijk}^*}{\xi_0 k_c} \right) \quad (10-45)$$

Here k_c , the continuum opacity uncorrected for stimulated emissions, has been introduced for convenience (and continuum scattering has been ignored). The population n_{ijk}^* , of excitation-state i , of ionization-stage j , of chemical species k , is assumed to be given by the Boltzmann-Saha equations as described in §5-1.

In a stellar spectrum one can usually observe lines from several multiplets of a given ion, and one or more ionization stages of a given element, for each of several elements. Let us first consider only lines from a definite ion of a single element. Because of the factor $\exp(-\chi_{ijk}/kT)$ in the Boltzmann excitation formula, each multiplet has its own curve of growth. In view of equation (5-8) we may write

$$\log \beta_0 = \log(g_{ijk}f\lambda) - \theta\chi_{ijk} + \log C_{jk} \quad (10-46)$$

where $\theta \equiv 5040/T$, χ is expressed in eV, and

$$C_{jk} \equiv [N_{jk}/U_{jk}(T)](\pi^2 e^2/mc)(\xi_0 k_c)^{-1} \quad (10-47)$$

Clearly the value of β_0 will be affected by the choice for the temperature (θ) in the atmosphere, and will be different for each multiplet (because of differences in χ_{ijk}), and for each line (because of differences in f -values).

To construct an empirical curve of growth, we plot the value of $\log(W_\lambda/\lambda)$ versus $\log(gf\lambda)$ for each line. Now if we assume that there is a unique relation between β_0 and W_λ , we attempt to force all points for the different lines to define a single curve as nearly as possible. To do this, we adjust θ , and choose the value that minimizes the scatter around a mean curve. This value is called the *excitation temperature*, θ_{exc} , and is considered to be the characteristic temperature of the line-forming region. It should be realized that it may not always be possible to derive a meaningful excitation temperature, for different lines will actually be formed in different regions of the atmosphere. For example, one would expect that lines from levels with high excitation potentials will be formed deeper in the atmosphere where temperatures are higher. Similarly, we would expect the average excitation temperature to be higher for higher stages of ionization. Such refinements can be taken into account by more elaborate calculations that use model atmospheres, but they are normally ignored in curve-of-growth work.

There are other complications that arise in practice: there are errors both in the values of W_λ and f , and these introduce scatter into the curve. Also, lines arising from only a limited range of excitation potentials may be observable, and θ_{exc} may not be very well determined over this short baseline.

Once the empirical curve, corrected for excitation effects, has been established, it may be compared with theoretical curves. To superimpose the two curves, a shift (both in abscissa and ordinate) of the empirical curve relative

to the theoretical is normally required. From this fitting procedure we can deduce three essential bits of information.

(1) The ordinate of the empirical curve is $\log(W_\lambda/\lambda)$, while that of the theoretical curve is $\log(W_\lambda/\Delta\lambda_D) = \log(W_\lambda/\lambda) - \log(\xi_0/c)$. Thus when the two curves are superimposed, the difference in the ordinates yields $\log(\xi_0/c)$, and thus the velocity parameter ξ_0 . The value derived can be compared with the most probable thermal velocity at the excitation temperature T_{exc} , namely $\xi_{therm} = (2kT_{exc}/Am_H)^{1/2}$ where A is the atomic weight of the element. It is usually found that ξ_0 as inferred from the curve of growth exceeds ξ_{therm} , sometimes by a large factor. To explain this difference, it has been customary to postulate the existence of additional nonthermal motions of the stellar material, which are usually referred to as *microturbulence*. It is assumed that these motions occur on scales that are small compared to a photon mean-free-path and hence constitute, in effect, an additional source of line-broadening. If these small-scale mass motions have a Gaussian distribution around some most probable speed ξ_{turb}^2 , then

$$\xi_0 = [(2kT_{exc}/Am_H) + \xi_{turb}^2]^{1/2} \quad (10-48)$$

"Turbulent" velocities have been derived for many stars by this method of analysis; the most dramatic results are obtained for supergiants where velocities in excess of the sound speed in the gas have been obtained. It should be realized, however, that such diagnoses are not on entirely firm ground because the introduction of a velocity field drastically affects the details of line formation (cf. Chapter 14). Indeed, with the high velocities sometimes derived, one must inquire whether the excitation state of the gas is affected by interchange of energy between mass motions and the internal energy of the material. Very little work has been done on this difficult problem, and our knowledge about small-scale stellar velocity fields remains rudimentary, almost to the point of merely recognizing their existence.

(2) The difference between the abscissae of the empirical and theoretical curves of growth yields

$$\log C = \log \beta_0 - [\log(gf\lambda) - \theta_{exc}\chi] \quad (10-49)$$

To proceed further, we need an estimate of the electron density. This is derived from a theoretical model of the atmosphere. Once we know n_e , we may compute k_c , and as we already know ξ_0 , we find N_{jk} , the number of atoms of chemical species k in ionization stage j directly from C , via equation (10-47). Then by use of the Saha ionization formula we can convert N_{jk} to N_k , the number of atoms of chemical species k in all ionization states. More precisely, we obtain the abundance $\alpha_k = (N_k/N_H)$, as k_c is usually dominated by hydrogen or H^- , and thus is proportional to N_H . In short, the horizontal

shift between the two curves of growth yields the abundance of the element. This method of analysis has been applied to a wide variety of stars, and has shown that certain stars (e.g., Population II stars and peculiar stars) have abundances that differ markedly from solar values, which, in turn, are fairly typical of Population I stars. The uncertainties in a curve of growth abundance analysis should be clear: it has been assumed that the Saha–Boltzmann relations are valid; depth variations of the relevant parameters (called *stratification effects*) have been ignored; and a schematic solution of the transfer problem has been employed. The accuracy of the results is, therefore, limited.

(3) The horizontal and vertical shifts described above make use of the linear and flat parts of the curve respectively. For a given set of theoretical curves, a comparison between the observed and computed damping parts determines the value of $a = \Gamma/(4\pi \Delta v_D)$, and hence Γ ; this in turn may be compared with the value predicted by line-broadening theory.

Let us now turn to a brief discussion of a few typical results. The solar spectrum has been analyzed extensively with curve-of-growth techniques; one of the most outstanding early treatments was by H. N. Russell (542), who derived element abundances (from eye-estimates of line-strengths!) that are in remarkably good agreement with current estimates. A very interesting study using curves of growth was carried out by K. O. Wright (686) who analyzed the Sun and three other solar-type stars. This study is by no means the most recent available [see, e.g., (182)], but it is a classic example of the procedure, so we shall consider it here. From an extensive set of equivalent-width measurements and laboratory f -values, an empirical curve of growth was constructed using lines of Fe I and Ti I. In all, some 75 lines of Fe I arising from states with $0 \leq \chi \leq 1.6$ eV, and 137 lines of Ti I with $0 \leq \chi \leq 2.5$ eV, were used to obtain the curve shown in Figure 10-3. Slightly different excitation temperatures were found for the two atoms, namely $T_{\text{exc}} = 4850^{\circ}\text{K} \pm 150^{\circ}\text{K}$ for Fe I and $T_{\text{exc}} = 4550^{\circ}\text{K} \pm 150^{\circ}\text{K}$ for Ti I. These values are about what we would expect for a radiative-equilibrium model atmosphere. As can be seen, the curve is well defined, though it is true that the linear part is defined mainly by Ti I lines and the damping part by Fe I lines. It would be more satisfactory if lines of each atom were found in both the linear and damping portions of the curve.

The vertical shift of the empirical curve, relative to a theoretical curve by Menzel, yields a velocity parameter $\xi_0 = 1.6 \text{ km s}^{-1}$. As the thermal velocity for these atoms in the solar atmosphere is about 1.2 km s^{-1} , this implies a microturbulent velocity of about 1.0 km s^{-1} . By a fit to the damping part of the theoretical curves, $\log a = -1.4$ was obtained. Adopting an average wavelength of 4500 \AA for the lines, this yields $\Gamma = 1.7 \times 10^9 \text{ s}^{-1}$, which is very nearly a factor of 10 larger than the classical damping constant Γ_c . It is clear that the main source of the line broadening must be collisions.

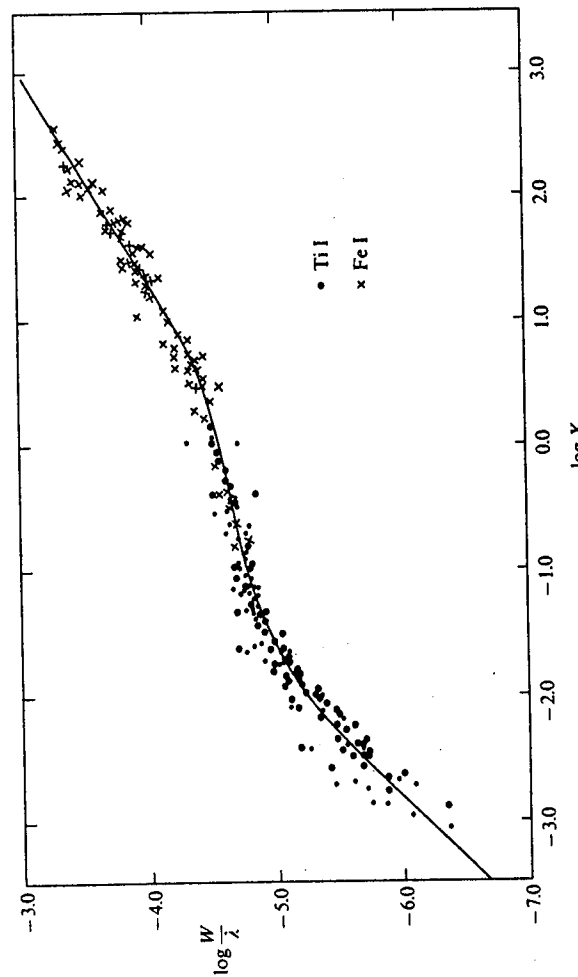


FIGURE 10-3
Empirical curve of growth for solar Fe I and Ti I lines. Abscissa is based on laboratory f -values. From (686).

and because hydrogen is mostly un-ionized in the solar photosphere, the most likely process is van der Waals interactions between hydrogen and the radiating atom. An approximate result for Γ_6 was obtained previously [equation (9-71)], namely $\Gamma_6 \approx 8.1 C_6^{\frac{1}{2}} v^{\frac{1}{2}} N_H$ where $C_6 \approx [13.6/(\chi_{\text{ion}} - \chi_i)]^2 \times 10^{-32}$ [equation (9-76)]. For a typical value $(\chi_{\text{ion}} - \chi_i) = 6 \text{ eV}$, $C_6 \approx 5.2 \times 10^{-32}$; typical values for v and N_H are 10^6 cm s^{-1} and 10^{17} cm^{-3} , so $\Gamma_6 \approx 10^9$, which is in basic agreement with the empirical value. The damping part of the empirical curve is found to have a slope (on a logarithmic scale) closer to 0.6 than 0.5. The likely explanation is that lines of widely differing strengths are formed in different layers, so that the parameters describing them (e.g., damping widths) are not identical, as was assumed in constructing the curve of growth.

Many other analyses of the solar spectrum have been made. An improvement over the basic curve of growth method is obtained by using a *saturation function* (505) that accounts for the fact that the line cores and wings are actually formed in different layers of the atmosphere. This is conveniently done in the *method of weighting functions*, which is described in detail in (261, Chap. 4), and which has been applied in one of the classic abundance analyses of the solar spectrum (252).

An important application of the solar curve of growth is in *differential abundance analyses* of stars with respect to the Sun. Excellent examples of this approach for G-type subdwarfs (extremely metal-deficient stars) and for Population II K-giants can be found in (13) and (294) respectively. An advantage of this approach is that oscillator strengths, which are often poorly known, cancel out of the analysis to first order. Also, because the temperatures of these stars are close to the solar value, one might hope that their atmospheric structures are at least roughly similar to the Sun's. If this is the case, then other effects, such as line-blending, stratification, departures from LTE, etc. might also cancel out to first order.

The fundamental assumption made in a differential analysis is that the *stellar curve of growth*, $\log(Wc/\lambda\xi_0)^*$ versus $\log \beta_0^*$, is identical to the *solar curve*, $\log(Wc/\lambda\xi_0)^{\odot}$ versus $\log \beta_0^{\odot}$. In practice we do not know β_0^* or ξ_0^* , and thus we cannot construct the stellar curve directly. What is known for each line is $\log(W/\lambda)^*$ and the value of $\log \beta_0^{\odot}$ for that line from its observed solar equivalent width. From the definition of β_0 [see equation (10-45)], we have

$$\log\left(\frac{\beta_0^{\odot}}{\beta_0^*}\right) = \log\left(\frac{N_{jk}^{\odot}}{N_{jk}^*}\right) + \chi_{ijk}(\theta_{\text{exc}}^* - \theta_{\text{exc}}^{\odot}) + \log\left(\frac{\xi_0^* k_c^* U^*}{\xi_0^{\odot} k_c^{\odot} U^{\odot}}\right) \quad (10-50)$$

If we define $[X] \equiv \log(X^{\odot}/X^*)$ for any quantity X , then equation (10-50) may be rewritten as

$$[\beta_0] = [N_{jk}] + \chi_{ijk} \Delta\theta - [\xi_0] - [k_c] - [U] \quad (10-51)$$

Thus, if we plot $\log(W/\lambda)^*$ for lines of a given ion, say Fe I, versus $\log \beta_0^{\odot}$ instead of $\log \beta_0^*$, lines of different excitation potentials will scatter around a mean curve if there is a difference in excitation temperature between the star and the sun. Therefore, we plot $\log(W/\lambda)^*$ versus $(\log \beta_0^{\odot} - \chi_{ijk} \Delta\theta)$ and choose $\Delta\theta$ to minimize the scatter. For the G-subdwarfs it is found (13) that $\Delta\theta \lesssim 0.05$, while for Population II K-giants $\Delta\theta$ is about 0.25 to 0.35 (294). After the effect of $\Delta\theta$ is eliminated, the empirical curve for the star is superimposed upon the solar curve, in which $\log(Wc/\lambda\xi_0)^{\odot}$ is plotted versus $\log \beta_0^{\odot}$. The *vertical* shift gives directly $[\xi_0]$ while the *horizontal* shift yields the average value of $\delta \equiv [N_{jk}] - [\xi_0 k_c U]$ for the ion under consideration. For the G-subdwarfs ξ_0 is found to correspond closely to a pure thermal value (no turbulence), while for the K-giants there is appreciable turbulence. As the temperatures of these stars are fairly close to the solar value, the partition-function ratio is usually set to unity, and the value of δ depends primarily upon abundances, and upon differences in ionization and continuous opacity. Because H^- is the main contributor to k_c in the temperature range under consideration, the value of $[k_c]$ will essentially equal $[n_e]$. We can determine $[n_e]$ from an analysis of the ionization equilibrium using information from two stages of ionization of the same element k . If we have observations for two stages of ionization (say "0" and "1"), we may write

$$\delta_{jk} = [N_{jk}] - [\xi_0 k_c], \quad (j = 0, 1) \quad (10-52)$$

Using these two values of δ we can derive

$$\begin{aligned} \Delta &\equiv \delta_{1k} - \delta_{0k} = [N_{1k}] - [N_{0k}] \\ &= \log(N_{1k}^{\odot}/N_{0k}^{\odot}) - \log(N_{1k}^*/N_{0k}^*) \end{aligned} \quad (10-53)$$

As $\log(N_{1k}^{\odot}/N_{0k}^{\odot})$ is known, the observed value of Δ yields $\log(N_{1k}^*/N_{0k}^*)$. But if we assume that the temperature is specified by θ_{exc}^* (which is known), then Saha's equation gives $\log(N_{1k}^* n_e^*/N_{0k}^*)$; hence we may determine $\log n_e^*$ and $[n_e]$. Estimates of $[n_e]$ can be obtained from several different elements, and a mean value taken. Knowledge of $[n_e]$ allows us to evaluate $[k_c]$ and $\log(N_{jk}^*/N_{jk}^*)$. Hence finally we can calculate the ratio of the abundance of the element in the star to its abundance in the Sun as

$$\begin{aligned} \log(N_k^{\odot}/N_k^*) &= \log(N_k^{\odot}/N_{jk}^{\odot}) + \log(N_{jk}^*/N_k^*) + \log(N_{jk}^{\odot}/N_{jk}^*) \\ &= \log(N_k^{\odot}/N_{jk}^{\odot}) + \log(N_{jk}^*/N_k^*) + \delta + [\xi_0 k_c U] \end{aligned} \quad (10-54)$$

because all four terms on the righthand side of the second equality are now known.

The results of the two analyses mentioned above lead to the striking conclusion that the abundances of the heavy elements in Population II stars are lower than their abundances in the Sun by a factor of the order

of 10^2 ! This is a fact of tremendous significance for the construction of a picture of the evolution of the Galaxy, and it implies that the heavy elements in Population I stars such as the Sun are the result of nucleosynthesis in earlier generations of stars. The errors in abundances derived from curve-of-growth studies are typically of the order of a factor-of-two uncertainty; although such errors are serious, and motivate the development of more precise methods, they do not change the qualitative results for Population II stars mentioned above.

10-5 LTE Spectrum Synthesis with Model Atmospheres

The curve of growth approach introduces a large number of simplifying approximations, which seriously limit the accuracy of the results obtained. Considerable improvement is achieved if the *physical assumption* of LTE is retained, but now a *model atmosphere* is employed to represent the depth-variation of all physical parameters. Given such a model, one may compute both κ_c and $\chi_i \phi_i$ as functions of depth, allowing fully for the variation of the temperature, ionization-excitation equilibrium, Doppler widths, damping parameters, etc. It is then possible to compute the optical depth

$$\tau_v(z) = \int_z^{z_{\max}} [\kappa_c(z') + \chi_i(z') \phi_i(z')] dz' \quad (10-55)$$

and hence the emergent flux in a line at frequency v

$$F_v = 2 \int_0^\infty B_v [T(\tau_v)] E_2(\tau_v) d\tau_v \quad (10-56)$$

by direct numerical quadrature, with as much mathematical accuracy as desired.

The first step in this method is to select the model atmosphere that most closely resembles the stellar atmosphere to be analyzed. This choice is made by comparing observed and computed values of certain key features in the spectrum. Typically the comparison is made for (1) continuum features such as the overall energy distribution, the Balmer jump D_B , or a color such as $(b - y)$; (2) line profiles of the hydrogen lines (which are density-sensitive); (3) ratios of line-strengths for lines of two ionization stages of a given element. For example, in B-stars, the continuum parameters determine mainly the effective temperature T_{eff} ; the hydrogen lines determine mainly $\log g$; the ratio of, say, Si III $\lambda 4552$ to Si II $\lambda 4128$, 31 is a function of both T_{eff} and $\log g$ (the *ratio* is insensitive to the element abundance). Examples of fits of computed and observed energy distributions are shown in Figures 7-4 through 7-6 and in Figure 7-8. Figure 10-4 shows a fit to the

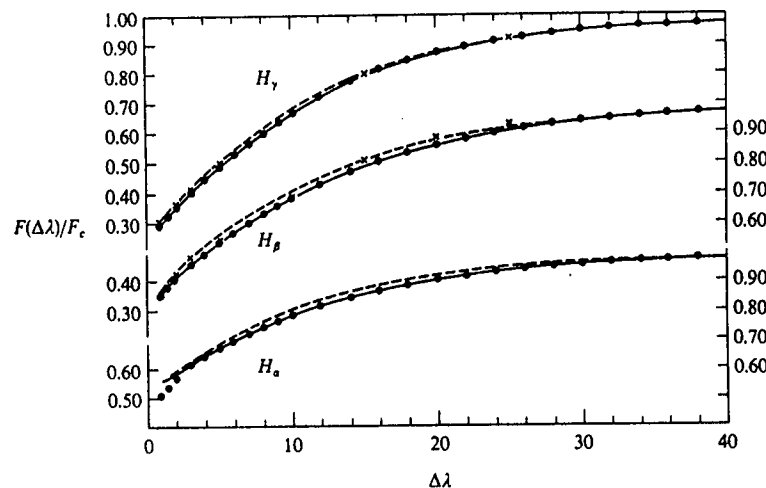


FIGURE 10-4
Hydrogen Balmer-line profiles in Vega. Solid dots: observed profiles from (509). Crosses: observed profiles from (71). Abscissa: $\Delta\lambda$ in Å. Curves are computed profiles from a model with $T_{\text{eff}} = 9650^{\circ}\text{K}$ and $\log g = 4.05$. From (555), by permission.

observed hydrogen line profiles in the standard star Vega (555). Often a plot is made, in a diagram of T_{eff} versus $\log g$, of the loci of (T_{eff}, g) values for which the computed value of a given parameter [say D_B or $W(H_\gamma)$] equals the observed value. The loci for different criteria will intersect, and thus define an optimum value of (T_{eff}, g) . Ideally the curves would intersect at a single point; in practice they will intersect within a small area, which introduces an uncertainty into both T_{eff} and g . Examples of this procedure for the normal B-star γ Peg and the He star HD 184927 are given in (508) and (299), respectively.

Having chosen a model atmosphere, it becomes possible to carry out an abundance analysis. One now replaces the curve of growth by a computation of the equivalent width, of each line under consideration, as a function of element-abundance relative to hydrogen. Knowledge of the observed equivalent width of each line thus leads to an estimate of the element abundance; these estimates may be suitably weighted and averaged over all lines to yield a final abundance estimate.

Although the choice of the model atmosphere used in the abundance analysis is based on continuum and hydrogen-line criteria, there is usually some ambiguity in $(T_{\text{eff}}, \log g)$. Often the results of the abundance analyses for several elements can be used to narrow the range of uncertainty in

$(T_{\text{eff}}, \log g)$, and to choose a more refined model, much in the same way as atmospheric properties may be inferred from a curve-of-growth analysis. For example, after the analysis is completed, the derived abundances for many lines may be examined to see if they show a correlation with excitation potential; such a correlation would be expected if the temperatures in the atmosphere are incorrectly chosen. The elimination of any such correlations may, therefore, lead to an improved choice of T_{eff} for the model. Similarly, for a given element, identical abundances should be derived from all ionization stages. Differences that are found between ionization stages contain information about errors in the choice of temperatures and pressures, and thus about T_{eff} and $\log g$ for the model. Finally, one can examine the derived abundances to see if they show a correlation with equivalent width. If, for example, stronger lines systematically lead to larger abundances, the velocity parameter may have been underestimated, and thus information about turbulent velocities to be included in the model can be derived. (As we shall see in Chapter 11, however, departures from LTE must also be considered when a determination of the velocity parameter from strong lines is attempted.) Naturally, errors in the observed equivalent widths, in f -values, and in other atomic parameters will introduce scatter; hence the procedure outlined above may not be completely unambiguous. Nevertheless, examination of the correlations just mentioned can often lead to a significantly better choice for the model. Finally, if the derived abundances are very different from those used in construction of the model (as they might be for, say, Ap stars), it may be necessary to recompute models with appropriate abundances, re-derive T_{eff} and $\log g$, and perform the analysis over.

An example of the model-atmosphere method of abundance analysis is that for the two bright A-stars Vega and Sirius in (609). The results of this work show that Vega has very nearly solar abundances of the heavy elements, while Sirius has abundances a factor of 4 to 10 higher. In many respects Sirius mildly resembles the group of A-stars called *metallic-line A-stars* (Am stars) because of the strength of the metal lines in their spectra. The present literature of abundance analyses (and estimates of atmospheric parameters such as T_{eff} and $\log g$) by both curve-of-growth and model-atmosphere techniques is vast; extensive lists of references to research papers on the subject for both normal and peculiar stars can be found in (12; 70, 57–204; 144; 450, 157–237; 493; 523; 552; 560; 658). The work thus far described makes use primarily of equivalent widths. For some stars, for which very high-quality spectroscopic data are available, a detailed point-by-point synthesis of the spectrum is possible. An example of such a synthesis for the Sun (538) is shown in Figure 10-5. Analyses of this kind can lead to accurate abundances and to the identification of hitherto unnoticed weak blends in the spectrum; applications of spectrum synthesis to the calibration of photometric systems were described in §7-4.

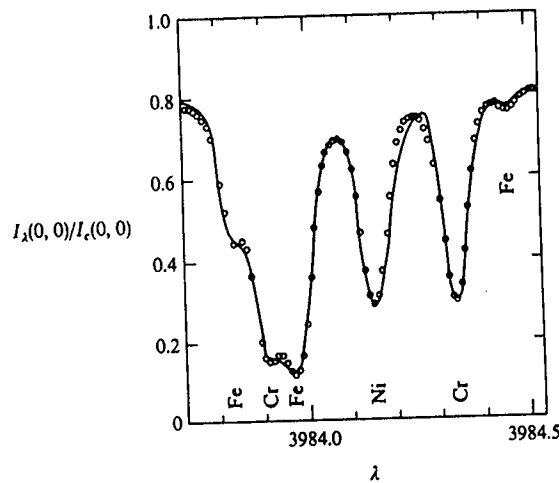


FIGURE 10-5
Spectrum synthesis for solar Fe, Cr, and Ni lines. *Curve:* observed intensity; *open circles:* computed intensity. *Ordinate:* emergent specific intensity at disk-center relative to continuum; *abscissa:* wavelength in Å. From (538) by permission.

All of the methods described in this chapter make the assumption of LTE. As we shall see in Chapters 11 and 12, however, this assumption is often a poor description of the physics of line-formation, and can lead to results containing serious systematic errors. Let us now, therefore, turn to the problem of solving the combined equations of radiative transfer and atomic statistical equilibrium fully consistently.

11

Non-LTE Line Transfer: The Two-Level Atom

Much of the progress in understanding the physics of line-formation has come from a study of solutions of the *combined* transfer and statistical equilibrium equations: the so-called non-LTE approach. In this chapter we shall consider some schematic line-formation problems that are simple enough to be solved readily, but which, nevertheless, provide a good description of the physically important processes—and yield considerable insight. It will be obvious that some of the assumptions made are oversimplifications, and are not valid in actual stellar atmospheres, for which elaborate numerical calculations are required to yield accurate results. On the other hand, the real goal is to *understand* the answers, not merely obtain them. This can be done only with a clear grasp of the prototype cases discussed in this chapter, which provide a *conceptual* framework of great usefulness for the interpretation of results from computations with complicated model atoms and detailed model atmospheres.

11-1 Diffusion, Destruction, Escape, and Thermalization

The most important difference between the LTE and non-LTE treatments of line-formation is the way in which the coupling between the gas and radiation

is handled. In the LTE approach, it is *assumed* that the *local* values of two thermodynamic variables (T and N) are sufficient to determine completely the excitation and ionization state of the gas (and hence transfer quantities such as χ_v , η_v , and S_v), independently of the state of the gas at other points. (This remark is strictly true only when the temperature structure is *given*; if it is determined by the condition of radiative equilibrium, then there is a coupling among different points in the atmosphere—see §7-2—but not in the sense we are concerned with here.) It has been emphasized in previous chapters that the excitation and ionization state of the gas is, in fact, strongly influenced by the radiation field, which, in turn, is determined by the state of the gas throughout large volumes of the atmosphere, via the transfer equation. In actuality the two problems of radiative transfer and statistical equilibrium are inextricably coupled, and must be considered *simultaneously*.

Much of the basic physics of line-formation can be understood by consideration of the characteristic lengths for photon diffusion, destruction, and thermalization, which are related to photon escape and destruction probabilities. For simplicity we shall suppose that the atom consists of a ground state (denoted l) and a single excited state (denoted u). The distance over which a line photon will, on the average, move in the atmosphere between successive interactions with the material (absorptions) can be represented by the average *mean-free-path* l . The mean-free-path for a photon emitted at a given frequency is the distance interval whose optical thickness at that frequency is about unity—i.e., $l_v \approx 1/\chi_v = (\chi_{lu}\phi_v + \chi_c)^{-1}$ where χ_{lu} and χ_c are the line and overlapping continuum opacities, and ϕ_v is the line profile. For complete redistribution, the probability of emission at frequency v is ϕ_v , so $l = \langle l_v \rangle = \int l_v \phi_v dv$. It is obvious that photons emitted in the core travel relatively small distances, while those in the wings can travel much greater distances, up to a distance corresponding to unit optical thickness in the continuum.

When a photon is absorbed in the line and excites an atom to the upper state, it is *usually* re-emitted in a radiative de-excitation and travels another mean-free-path. This process may occur *again and again* before the photon is ultimately *destroyed*, and has its energy deposited into the thermal pool, either by a collisional de-excitation or by an absorption in the overlapping continuum. Thus there exists a characteristic length L , the *destruction length*, over which a photon may travel before it is destroyed. The destruction length has a more basic physical significance than the mean-free-path, for it measures the distance over which a photon emitted at a given point retains its identity and hence can “communicate” information about conditions at that point to another. Thus L determines an *interaction region*: the volume containing those points that can influence one another via photon exchange.

The relative sizes of L and l depend upon the photon *destruction probability* P_d , which gives the average probability that the photon is destroyed

when it next interacts with the material. The probability for photon destruction by collisions following absorption in the line is $C_{ul}/(A_{ul} + C_{ul})$ where C_{ul} is the rate of collisional de-excitation and A_{ul} is the spontaneous emission rate; now $C_{ul} \propto n_e$, so that it is clear that the contribution by collisions to the total destruction probability becomes large (i.e., approaches unity) in the deeper, denser regions of a stellar atmosphere, and can be quite small in the uppermost layers. If we assume that all photons absorbed in the continuum are destroyed thermally, the contribution of continuum processes to P_d is the average of $\chi_c/(\chi_{lw}\phi_v + \chi_c)$ over the line profile. The continuum sets an upper bound on both l and L because a photon cannot travel more than a unit optical depth in the continuum before it is absorbed—and when it is, it is also destroyed.

At great depths in the atmosphere, P_d approaches unity because of large densities (and hence collision rates) and because of the strength of the overlapping continuum. Then $L \rightarrow l$, for the photon is almost surely destroyed when it is next absorbed. Assuming that the continuum is already optically thick, it is clear that the radiation field becomes very strongly coupled to local conditions and *thermalizes* to its local thermodynamic equilibrium value. In contrast, when the destruction probability is very small, $L \gg l$, and the interaction region may become *enormous* compared to the volume over which a photon can diffuse in a single flight. In this case, the radiation field is dominated by *nonlocal* influences, and represents the result of physical conditions that may be quite inhomogeneous. For example, within the volume there may be large variations of the kinetic temperature that imply strong variations of thermodynamic properties and of the Planck function. The radiation field may then depart *markedly* from its local equilibrium value, and this departure will extend throughout the entire interaction region.

The importance of these notions becomes manifest when we consider a sequence of test points approaching the surface of the atmosphere. At the deepest points we obtain equilibrium. But as we approach the surface, the distance L grows, and eventually the interaction volume contains the boundary itself (more precisely, extends above the depth at which $\tau = 1$ anywhere in the line). Then a new phenomenon enters the picture: photons *escape* from the medium into space. It follows that the radiation field, at test points whose interaction regions extend into space beyond the surface, must be depressed *below* the value it would have had if there were no boundary, for no radiation is emitted in the region void of material, and photon escapes are therefore uncompensated. This effect leads to a deficiency in the radiation throughout an entire interaction volume, and hence extends to depths at least of the order of L . But of course the radiation field at these points influences that at points that lie yet another destruction length L deeper, and therefore there is a “compounding” of the effect, which leads to

a departure of the radiation field from its equilibrium value at positions far below the surface.

The depth at which the radiation field (or source function) ultimately approaches closely its equilibrium value is the *thermalization depth* Λ ; this concept, introduced by Jeffries (333), has proven to be extremely fruitful. To obtain a quantitative estimate of Λ we define the *escape probability* $P_e(\tau)$ as the probability, averaged over the line, that a photon emitted at line optical depth τ escapes from the medium before being absorbed along its path of flight. The mechanism competing with photon escape is photon destruction; the former induces a departure from equilibrium while the latter leads to coupling to the local thermal pool. We therefore compare P_e with P_d . Deep within the atmosphere where $P_e(\tau) \ll P_d$, photons are surely thermalized before they can escape, hence $S \rightarrow B$; at the surface where $P_e(\tau) \gg P_d$, photons escape freely before thermalization, hence S will depart from B . It is therefore reasonable, on physical grounds, to identify the thermalization depth Λ as that point at which $P_e(\Lambda) = P_d$. Defined in this way, Λ is essentially the greatest depth from which photons have a significant chance to escape before being destroyed.

Now the escape probability (and hence Λ) depends sensitively (a) upon the nature of photon redistribution over the line profile upon emission, and (b) upon the amount of background continuum absorption. The probability for photon absorption is highest at line center. If photons are emitted *coherently*, then those absorbed at line center will be re-emitted there, and hence will tend to be trapped by the large line-core optical depth up to the very uppermost layers, where the line finally becomes optically thin; this will tend to prevent serious departures of the line-core radiation field (which contributes heavily to the total photoexcitation rate) from its equilibrium value up to the shallowest layers of the atmosphere. In contrast, if photons are *completely redistributed* over the line profile, then there is a significant chance that after a number of scatterings a photon absorbed at line-center will be emitted in the line-wing where the opacity is low, and the probability of escape is high. Photons that would have been trapped, if emitted coherently, now freely escape from the atmosphere, depressing the line-core intensity (and photoexcitation rate) in much deeper layers in the atmosphere. The radiation field in the line as a whole now responds to the fact that the boundary lies within a mean-free-path at some frequencies, even if not at others. The role of the continuum is obviously important in the case of complete redistribution, for it sets a lower bound on the total opacity, and hence an upper bound on the depth from which escapes become possible at *any* frequency, no matter how far out in the line-wing. It is thus clear that we should expect the thermalization depth to be much larger, and the surface departures from equilibrium larger, when the scattering process is non-coherent instead of coherent; further, we expect the magnitude of these

effects to be larger, the more highly developed the line-wings are relative to the core. We shall find these expectations are fulfilled by the detailed analysis given below.

It has been possible to extract practically all of the physical flavor of the problem using the qualitative arguments given above. Let us now turn to a mathematical discussion to obtain quantitative results, and to extend the analysis to cases where such heuristic discussion becomes less effective.

11-2 The Two-Level Atom without Continuum

THE SOURCE FUNCTION

Consider a schematic atomic model consisting of only two levels, l and u , between which radiative and collisional transitions can occur. This model is obviously very incomplete, but it nevertheless provides a fairly good description of the real situation for some lines. In particular, *resonance lines* arising from the ground state are well described by this model when the coupling of the lower and upper levels to the continuum (and of the upper level to other levels) is weak. For the present, assume that the *only* sources of opacity and emission at the line frequency are from the line itself; then the transfer equation is

$$\mu(dI_v/dz) = [-n_l B_{lu} I_v + n_u (A_{ul} + B_{ul} I_v)] \phi_v (hv/4\pi) \quad (11-1)$$

Here we have assumed *complete redistribution* so that the absorption and emission profiles are identical. Define the optical depth scale in terms of the frequency-integrated line opacity (which characterizes the average opacity in the line as a whole), $d\tau \equiv -\chi_{lu} dz$ where

$$\chi_{lu} = (n_l B_{lu} - n_u B_{ul})(hv/4\pi) = (\pi e^2/mc) f_{lu} [n_l - (g_l/g_u) n_u] \quad (11-2)$$

Then $\mu(dI_v/d\tau) = \phi_v (I_v - S_l)$ (11-3)

where $S_l = n_u A_{ul} / (n_l B_{lu} - n_u B_{ul}) = (2hv^3/c^2) [(n_l g_u / n_u g_l) - 1]^{-1}$ (11-4)

the second equality following from application of the Einstein relations [cf. equations (4-8) and (4-9)]. As the factor v^3 varies only negligibly over the sharply peaked profile ϕ_v , S_l is called the *frequency-independent* source function; when the emission profile differs from the absorption profile, S_l becomes explicitly frequency-dependent (see §2-1 and §13-4). Equation (11-4) is an *implicit* form for the source function because the level-populations depend upon the radiation field; this dependence can be displayed *explicitly* by incorporating information from the equations of statistical equilibrium that determine n_l and n_u .

The statistical equilibrium equation for level l is

$$n_l \left(B_{lu} \int \phi_v J_v dv + C_{lu} \right) = n_u \left(A_{ul} + B_{ul} \int \phi_v J_v dv + C_{ul} \right) \quad (11-5)$$

This equation can be used to write an expression for (n_l/n_u) . Upon substituting this expression into equation (11-4), making use of the detailed-balance result that $C_{lu} = (n_u/n_l) * C_{ul}$, and using the Einstein relations, we obtain quite directly

$$S_l = \left[\int \phi_v J_v dv + \varepsilon' B_v \right] / (1 + \varepsilon') \equiv (1 - \varepsilon) J_v + \varepsilon B_v \quad (11-6)$$

$$\text{where } \varepsilon' \equiv C_{ul} (1 - e^{-hv/kT}) / A_{ul} \quad (11-7)$$

$$\text{and } \varepsilon \equiv \varepsilon' / (1 + \varepsilon') \quad (11-8)$$

Exercise 11-1: Derive equation (11-6) in detail.

Each of the terms in equation (11-6) admits a straightforward physical interpretation. The source function contains a *noncoherent scattering term* J and a *thermal source term* $\varepsilon' B_v$. The thermal source term represents photons that are *created* by collisional excitation, followed by radiative de-excitation. The term ε' in the denominator is a *sink term* that represents those photons that are *destroyed* by a collisional de-excitation following a photoexcitation. These two terms describe completely the coupling of the radiation field to the local thermal state of the gas. The scattering term may be viewed as a *reservoir term* that represents the end result of the *cumulative* contributions of the source and sink terms *over the entire interaction region*.

It is clear that, if densities are made sufficiently large, then the collision rate C_{ul} may eventually exceed A_{ul} , so that ε' becomes $\gg 1$; then $S_l \rightarrow B_v(T)$, and LTE is recovered. However, in virtually all situations of astrophysical interest, $\varepsilon' \ll 1$ in regions of line-formation, and, in general, the source function cannot be expected to have a value close to the Planck function. This state of affairs was partially recognized in the classical theory by the division of lines into the categories of "absorption" and "scattering" lines; this division, however, was largely ad hoc, and the thermal coupling parameter had to be guessed from heuristic arguments. In the present analysis the coupling parameter follows directly, and uniquely, from the statistical equilibrium equation. Further, in the classical treatments of "pure" scattering lines, it was sometimes incorrectly argued that the small thermal terms could be discarded. The important point to bear in mind is that, even if the thermal term $\varepsilon' B$ is small compared to the scattering term J locally, when integrated over the entire interaction region it accumulates to a value of importance;

moreover, at depths greater than the thermalization depth the intensity must ultimately couple to the thermal pool. Indeed, if the thermal terms are discarded, the transfer equation becomes *homogeneous* in the radiation field and the scale of the solution is *unknown*; this scale is, in fact, *fixed by the (small) thermal terms* at the point of thermalization.

SOLUTION OF THE TRANSFER EQUATION

Having obtained an expression for the source function, let us now consider the solution of the transfer equation. It is convenient to work with the dimensionless frequency-variable x , measured from line center in units of Doppler widths (or damping widths for Lorentz profiles). In terms of this variable we shall write Doppler profiles as

$$\phi(x) = \pi^{-\frac{1}{2}} e^{-x^2} \quad (11-9a)$$

Voigt profiles as

$$\phi(x) = a\pi^{-\frac{1}{2}} \int_{-\infty}^{\infty} e^{-y^2} [(x - y)^2 + a^2]^{-1} dy \quad (11-9b)$$

and Lorentz profiles as

$$\phi(x) = (1/\pi)/(1 + x^2) \quad (11-9c)$$

which are all normalized such that

$$\int_{-\infty}^{\infty} \phi(x) dx = 1 \quad (11-10)$$

We will absorb a factor of Δv_D [or $(\Gamma/4\pi)$ for a Lorentz profile] into the definition of χ and write $d\tau \equiv -\chi_l(z) dz$, where now $\chi_l \equiv \chi_{lu}/\Delta v_D$, χ_{lu} being given by equation (11-2). Then

$$S_l(\tau) = [1 - \varepsilon(\tau)] \int_{-\infty}^{\infty} \phi(\tau, x) J(\tau, x) dx + \varepsilon(\tau) B(\tau) \quad (11-11)$$

and the transfer equation becomes

$$\mu[dI(\tau, x)/d\tau] = \phi(\tau, x)[I(\tau, x) - S_l(\tau)] \quad (11-12)$$

We now introduce discrete angle and frequency meshes $\{\mu_m\}$ and $\{v_n\}$, and replace *integrals* with *quadrature sums*:

$$\int_{-\infty}^{\infty} \phi(x) f(x) dx \rightarrow \sum_{n=-N}^N a_n f(x_n) \quad (11-13a)$$

and

$$\int_{-1}^1 f(\mu) d\mu \rightarrow \sum_{m=-M}^M b_m f(\mu_m) \quad (11-13b)$$

where the points are chosen symmetrically—i.e., $x_{-n} = -x_n$ and $\mu_{-m} = -\mu_m$ (also $a_{-n} = a_n$ and $b_{-m} = b_m$). Then the source function can be written in the same discretized form as was used in Chapter 6 [cf. equation (6-24a)],

$$S_d = (1 - \varepsilon_d) \sum_n a_n \sum_m b_m u_{dmn} + \varepsilon_d B_d \quad (11-14)$$

and the transfer equation can be reduced to the standard *second-order differential equation* form:

$$\mu_m^2 (d^2 u_{mn}/dt^2) = \phi_n^2 (u_{mn} - S) \quad (11-15)$$

where $u_n \equiv \frac{1}{2}[I_n(+\mu) + I_n(-\mu)]$. Equation (11-15) can be discretized on a mesh $\{\tau_d\}$, and solved numerically using either the Feautrier or Rybicki schemes discussed in §6-3. All of the relevant parameters (ε , B , and ϕ) may be depth-dependent without causing any difficulty in the calculation.

Alternatively, the transfer equation can be written in *integral equation* form. The formal solution of equation (11-12) is

$$J(\tau, x) = \frac{1}{2} \int_0^\infty S_l(t) E_1 \left| \int_\tau^t \phi(t', x) dt' \right| \phi(t, x) dt \quad (11-16)$$

For a depth-dependent profile, the argument of the E_1 function will depend upon both τ and t ; this greatly complicates the analysis, so we shall consider only the case of a depth-independent profile, in which case only the *displacement* ($t - \tau$) enters:

$$J(\tau, x) = \frac{1}{2} \phi(x) \int_0^\infty S_l(t) E_1 |(t - \tau)\phi(x)| dt \quad (11-17)$$

Substituting this expression for J into equation (11-11) yields an integral equation for S_l ,

$$S_l(\tau) = [1 - \varepsilon(\tau)] \int_0^\infty S_l(t) K_1 |t - \tau| dt + \varepsilon(\tau) B(\tau) \quad (11-18)$$

where the *kernel function* K_1 is given by

$$K_1(s) \equiv \frac{1}{2} \int_{-\infty}^{\infty} E_1(\phi_x s) \phi_x^2 dx = \int_0^\infty E_1(\phi_x s) \phi_x^2 dx \quad (11-19)$$

Exercise 11-2: Fill in the missing steps in the derivation of equation (11-18).

Exercise 11-3: (a) Show that the normalization of $K_1(s)$ is $\int_0^\infty K_1(s) ds = \frac{1}{2}$.
 (b) Using the result in (a), show that, for $\tau \rightarrow \infty$, where $S_i(\tau)$ must be a slowly-varying function and hence can be removed from the integral, $S_i(\tau) \rightarrow B$.

Numerical methods for solving equations of the form of (11-18) are discussed in detail in (52) and (18, Chap. 8); in most respects these resemble the Rybicki method of solving the differential equations, though Rybicki's method is simpler to apply when the profile is depth-dependent. In essence the solution is obtained by introducing a functional representation of $S(\tau)$ on a discrete grid $\{\tau_d\}$; these functions are integrated *analytically* against the kernel to construct a final matrix system of the form

$$\mathbf{S} = \mathbf{KS} + \mathbf{L} \quad (11-20)$$

where $\mathbf{S} = (S_1, \dots, S_d, \dots, S_D)^T$ represents the depth-variation of the source-function. The system is then solved by standard numerical techniques.

One of the advantages of the integral-equation formulation is that it displays explicitly the intimate dependence of the source function upon the mathematical behavior of the kernel function, and considerable insight can be gained by analytical study of the kernel. In particular, the *asymptotic form* of $K_1(s)$, for $s \gg 1$, shows that a characteristic feature of line-formation problems with noncoherent scattering is an extremely *long-range interaction* of one part of the atmosphere with another. Recall that for *coherent scattering* the appropriate kernel function in the formal solution is $E_1 |t - \tau|$ [cf. equation (2-57) and Exercise 2-10]. This kernel decays very rapidly, falling off as $\exp(-|t - \tau|)/|t - \tau|$, thereby limiting severely the range of depth-points that are directly coupled together in the scattering process. In contrast, the asymptotic behavior of $K_1(s)$ is found to be (53, Appendix I) $K_1(s) \sim 1/\{4s^2[\ln(s/\pi^{\frac{1}{2}})]^{\frac{1}{2}}\}$ for Doppler profiles, $K_1(s) \sim a^{\frac{1}{2}}/(6s^{\frac{1}{2}})$ for Voigt profiles, and $K_1(s) \sim 1/(6s^{\frac{1}{2}})$ for Lorentz profiles. Clearly the range of these kernel functions is very large compared to that for coherent scattering, and this implies that the radiation fields at widely separated points in the medium become mutually interdependent.

The physical reason for the long range of the noncoherent kernel functions is, of course, the redistribution of photons into the transparent line-wings. In the coherent case, any photon absorbed in the core will be re-emitted there, and hence always encounters high opacity and remains trapped. In the noncoherent case it has a probability of being emitted in the wings where, because of the lower opacity, it can travel over a large geometrical distance, and a correspondingly large integrated line optical depth, before it is again absorbed.

THE THERMALIZATION DEPTH

Let us now consider the behavior of the source function in an atmosphere in which ε and B are constant with depth. Naturally this is a very schematic case, but it provides useful insight. One of the most important characteristics of the problem to be determined is the *thermalization depth* at which the line source function approaches closely the Planck function B . Expressions for the thermalization depth can be derived by a wide variety of methods including (a) analysis of the asymptotic behavior of the solution of the integral equation (11-18) (53); (b) calculation of the distribution of the distances photons can travel from their points of creation to their places of destruction (545; 322); and (c) calculations of the probability distributions for photon escape from a given point of origin in the medium (214; 215; 216). One of the simplest and most appealing derivations can be made on the basis of the physical arguments given in §11-1: that the thermalization depth Λ must be near that point in the atmosphere where the probability of *photon escape*, $P_e(\Lambda)$, following a given scattering event is equal to P_d , the probability of *photon destruction* (28).

For the strict two-level atom with no overlapping continuum opacity, the probability of destruction per scattering event is just

$$P_d = C_{ul}/(A_{ul} + C_{ul}) = \varepsilon \quad (11-21)$$

where ε is as defined by equations (11-7) and (11-8) (ignoring stimulated emission for simplicity). The escape probability can be calculated by summing $\exp(-\tau\phi_x/\mu)$, the probability of escape at frequency x along a ray at angle $\cos^{-1}\mu$ to the normal, over all angles and frequencies, with weight ϕ_x (the probability for emission at frequency x within the profile):

$$\begin{aligned} P_e(\tau) &= \frac{1}{2} \int_{-\infty}^{\infty} dx \phi_x \int_0^1 e^{-\tau\phi_x/\mu} d\mu = \frac{1}{2} \int_{-\infty}^{\infty} dx \phi_x \int_1^{\infty} e^{-(\tau\phi_x)v} v^{-2} dv \\ &= \frac{1}{2} \int_{-\infty}^{\infty} E_2(\tau\phi_x)\phi_x dx \end{aligned} \quad (11-22)$$

For $\tau \gg 1$, the exponential integral is approximately zero for $|x| \leq x_1$, where $\phi(x_1)\tau \equiv 1$, and unity for $|x| > x_1$. Physically this states that photons are trapped in the core, where $\tau\phi_x > 1$, but in the wing where $\tau\phi_x \leq 1$, they escape freely. We may thus approximate $P_e(\tau)$ as

$$P_e(\tau) \approx \int_{x_1}^{\infty} \phi(x) dx \quad (11-23)$$

The above integral is easy to evaluate for $x_1 \gg 1$ (which it will be when $\tau \gg 1$). By direct substitution of equations (11-9) we find

$$P_e(\tau) = \frac{1}{2} \operatorname{erfc}(x_1) \approx e^{-x_1^2}/(2\pi^{1/2}x_1) \quad (\text{Doppler}) \quad (11-24a)$$

$$P_e(\tau) \approx a/(\pi x_1) \quad (\text{Voigt}) \quad (11-24b)$$

$$P_e(\tau) \approx 1/(\pi x_1) \quad (\text{Lorentz}) \quad (11-24c)$$

In deriving equation (11-24b), use was made of the asymptotic form of the Voigt function [cf. equation (9-45)]. Now the condition $\phi(x_1)\tau = 1$ implies

$$x_1 = [\ln(\tau/\pi^{1/2})]^{\frac{1}{2}} \quad (\text{Doppler}) \quad (11-25a)$$

$$x_1 = (a\tau/\pi)^{\frac{1}{2}} \quad (\text{Voigt}) \quad (11-25b)$$

$$x_1 = (\tau/\pi)^{\frac{1}{2}} \quad (\text{Lorentz}) \quad (11-25c)$$

Hence, substituting equations (11-25) into (11-24), setting $P_e(\Lambda) = P_d = \varepsilon$, and solving for Λ we find

$$\Lambda \approx c/\varepsilon \quad (\text{Doppler}) \quad (11-26a)$$

$$\Lambda \approx a/\varepsilon^2 \quad (\text{Voigt}) \quad (11-26b)$$

$$\Lambda \approx 1/\varepsilon^2 \quad (\text{Lorentz}) \quad (11-26c)$$

where c is a number of order unity that depends implicitly upon ε ; other factors of order unity have been suppressed.

Exercise 11-4: Show that for a profile with asymptotic form $\phi(x) \sim cx^{-\alpha}$, with $\alpha > 1$, the thermalization depth varies as $\Lambda \sim \varepsilon^{-\beta}$, where $\beta = \alpha/(\alpha - 1)$.

The striking feature of the results given by equations (11-26) is that the thermalization depth for a line with small ε is *enormous*. Recall that for coherent scattering the thermalization depth $\sim \varepsilon^{-\frac{1}{2}}$ (cf. §6-1 and 10-2). It is clear that the effects of noncoherence, with their attendant increase of photon diffusion in the line wings, greatly increase the depth in the atmosphere over which the source function can depart from the local Planck function. In fact, intercomparison of equations (11-26a) through (11-26c) shows immediately that an increase in the relative importance of the line-wing within the profile leads directly to an increase in the thermalization depth. It is worth stressing, however, that the above results do explicitly depend upon the assumptions of (a) no background opacity and (b) complete redistribution. We shall see later in this section that the effect of a background opacity can greatly reduce Λ .

In Chapter 13 we shall find that in the case of resonance lines, the scattering in strong *radiation-damping* wings is nearly *coherent*, and Λ is better approximated by equation (11-26a) than (11-26b).

From a mathematical point of view, equations (11-26) show that any *iterative* solution of the transfer equation starting from LTE is *futile* for small ε (much more so than the cases already discussed in §6-1!), and only *direct* solutions of the transfer equation will yield correct values.

BOUNDARY-VALUE AND DEPTH-VARIATION OF THE SOURCE FUNCTION

Having shown above that the source function may be decoupled from the Planck function over great depths in the atmosphere, let us now inquire what value the source function attains near the boundary of a semi-infinite atmosphere. If ε and B are taken to be constant with depth, the transfer equation (11-12) is easily solved by the method of discrete ordinates (53; 476). Writing $\lambda_n \equiv 1/\phi(x_n)$ we have the coupled system of equations

$$\lambda_n \mu_m (dI_{mn}/d\tau) = I_{mn} - \frac{1}{2} (1 - \varepsilon) \sum_{n'=-N}^N a_{n'} \sum_{m'=-M}^M b_{m'} I_{m'n'} - \varepsilon B \quad (11-27)$$

Considering first the homogeneous equation ($B \equiv 0$) and seeking a solution of the form $I_{mn} = g_{mn} \exp(-k\tau)$ one finds that

$$I_{mn} = c(1 + k\lambda_n \mu_m)^{-1} e^{-k\tau} \quad (11-28)$$

where the constants k are roots of the characteristic equation

$$2(1 - \varepsilon) \sum_{n=1}^N a_n \sum_{m=1}^M b_m (1 - k^2 \lambda_n^2 \mu_m^2)^{-1} = 1 \quad (11-29)$$

Exercise 11-5: (a) Verify equation (11-28). (b) Show that equation (11-29) is the appropriate characteristic equation for the system (11-27).

For $\varepsilon = 0$, the root $k^2 = 0$ is a solution. For $\varepsilon > 0$, k^2 must be greater than zero. As in our earlier use of the discrete-ordinate method (§3-3, §7-4) we may delimit the roots by the poles at $k^2 = 1/\lambda_n^2 \mu_m^2$, and if we label these poles in the order of *decreasing* values of $(\lambda_n \mu_m)$ we may write

$$0 < k_1^2 < (\lambda \mu)_1^{-2} < k_2^2 < \cdots < k_{MN}^2 < (\lambda_N \mu_M)^{-2} \quad (11-30)$$

which shows that the roots may be determined rapidly by a systematic search on appropriate finite intervals. As can be seen, it is convenient to label the roots with a subscript α , $1 \leq \alpha \leq MN$. By an analysis of the characteristic

equation similar to that used in deriving equation (3-65) one may readily show that

$$\prod_{\alpha=1}^{MN} (k_\alpha \lambda_n \mu_m)^2 = \varepsilon \quad (11-31)$$

We shall use this result below. For $B = \text{constant}$, a particular solution of equation (11-27) is $I_{mn} = B$. Thus the general solution must have the form

$$I_{mn} = B \left[1 + \sum_{\alpha=1}^{MN} L_\alpha e^{-k_\alpha \tau} (1 + k_\alpha \lambda_n \mu_m)^{-1} \right] \quad (11-32)$$

where the ascending exponentials have been discarded to keep the solution bounded at infinity. The surface boundary condition is, as usual, $I_{mn}(-\mu_m) = 0$. If we define

$$\mathcal{S}(x) \equiv 1 + \sum_{\alpha=1}^{MN} L_\alpha (1 - k_\alpha x)^{-1} \quad (11-33)$$

then the surface boundary condition may be expressed as $\mathcal{S}(\lambda_n \mu_m) = 0$ for ($m = 1, \dots, M$) and ($n = 1, \dots, N$). This set of linear equations may be solved numerically for the L_α 's. Substituting equation (11-32) into the expression for S_l on the right-hand side of equation (11-27), and making use of the characteristic equation (11-29) one finds

$$S_l(\tau) = B \left(1 + \sum_{\alpha=1}^{MN} L_\alpha e^{-k_\alpha \tau} \right) \quad (11-34)$$

In particular, at the surface,

$$S_l(0) = B \left(1 + \sum_{\alpha=1}^{MN} L_\alpha \right) = B \mathcal{S}(0) \quad (11-35)$$

Now, by an analysis similar to that used to derive equations (3-70) and (7-104) one may show that

$$\mathcal{S}(x) = \left[\prod_{\alpha=1}^{MN} k_\alpha \prod_{n=1}^N \prod_{m=1}^M (\lambda_n \mu_m - x) \right] / \prod_{\alpha=1}^{MN} (1 - k_\alpha x) \quad (11-36)$$

from which it follows, using equation (11-31) that

$$\mathcal{S}(0) = \prod_{\alpha=1}^{MN} (k_\alpha \lambda_n \mu_m) = \varepsilon^{\frac{1}{2}} \quad (11-37)$$

Exercise 11-6: (a) Derive equation (11-31). (b) Derive equation (11-34). (c) Derive equation (11-36).

By substitution of equation (11-37) into (11-35), we obtain finally the extremely important result

$$S_l(0) = \varepsilon^{\frac{1}{2}} B \quad (11-38)$$

This result is independent of the order of the quadrature sum and the form of the profile, and hence is general. The basic physical content of the results obtained thus far is contained in equations (11-38) and (11-26). It may be summarized in words as follows: when the coupling of the line-emission process to the thermal pool is weak ($\varepsilon \ll 1$), the source function can depart *drastically* from the thermal values, and this departure can extend to *great depth* in the atmosphere. Note that the surface value of the source function exceeds the local creation rate by a factor of $1/\varepsilon^{\frac{1}{2}}$. This implies that $S_l(0)$ is controlled primarily by photons fed in from the line wings. These photons originated deep in the atmosphere where $S_l(\tau) \gg S_l(0)$; it is therefore clear that *the surface value of S_l has little to do with the local thermal source term but is dominated by nonlocal effects*.

Numerical solutions (53) for the full depth-variation of $S_l(\tau)$ are shown in Figures 11-1 and 11-2. The cases in Figure 11-1 are for a semi-infinite atmosphere, constant Planck function ($B = 1$), a Doppler profile ($a = 0$), and various values of ε . It can be seen that in each case $S_l(0) = \varepsilon^{\frac{1}{2}}$, and that $S_l \rightarrow B$ at $\tau \sim 1/\varepsilon$. The results shown in Figure 11-2 are for lines with $\varepsilon = 10^{-4}$, and for Voigt profiles ranging from a pure Doppler profile to a pure

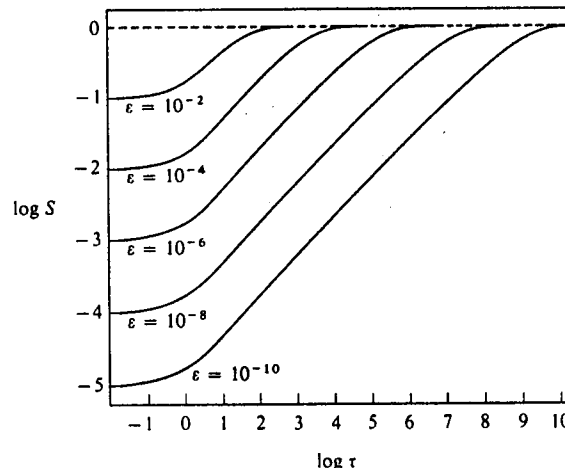


FIGURE 11-1
Line source functions in a semi-infinite atmosphere with $B = 1$, for a line with a pure Doppler profile ($a = 0$), and various values of ε . From (53), by permission.

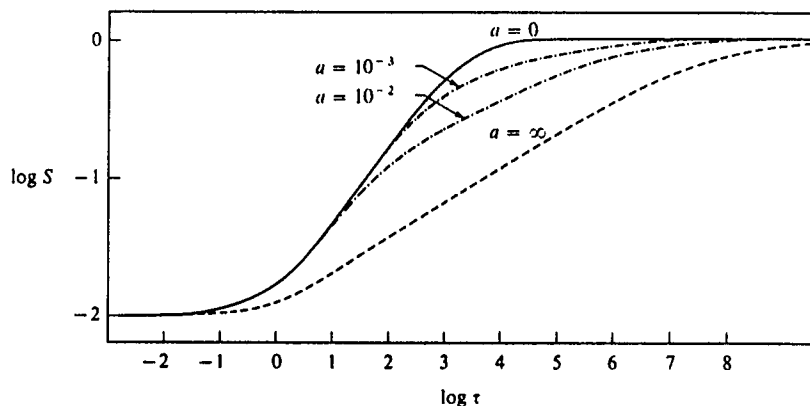


FIGURE 11-2

Line source functions in a semi-infinite atmosphere with $B = 1$, for lines with $\epsilon = 10^{-4}$, and Voigt profiles ranging from a pure Doppler profile ($a = 0$) to a pure Lorentz profile ($a = \infty$). From (53), by permission.

Lorentz profile ($a = \infty$). The increase in thermalization depth from ϵ^{-1} to ϵ^{-2} is shown plainly. The source functions in both Figures 11-1 and 11-2 will yield *absorption lines* with dark cores; in contrast, the LTE solution, with $S_i \equiv B$, would yield *no line* whatever. This difference can be attributed to the effects of scattering, and indeed the classical theory would also have predicted a line of the same central depth for the same ϵ . However there remain two important differences. (a) Both the upper- and lower-state occupation numbers differ from their LTE values; in many earlier “scattering” calculations LTE populations were (incorrectly) assumed. (b) The dark portion of the non-LTE profiles, where *noncoherent* scattering is assumed, are wider. The Eddington-Barbier relation implies that $I_v(0) \sim S_i(\tau_v = 1)$, hence the lines will be dark for $|x| \lesssim x_1$ where $\Lambda\phi(x_1) = 1$. Because Λ is so much larger for noncoherent scattering (ϵ^{-1} to ϵ^{-2} instead of $\epsilon^{-\frac{1}{2}}$), the corresponding values of x_1 will also be larger; we shall return to this point in §11-5. Finally, it must be remarked that the solutions obtained here are *fully consistent* solutions of both the transfer and statistical equilibrium equations; any approach that falls short of this level of consistency is unsatisfactory.

FINITE SLABS

The *finite slab* atmosphere of total thickness T is a case of astrophysical importance; it can be used to represent nebulae, or limited zones in an

atmosphere to which a particular ion is confined owing to changes in the ionization balance (e.g., chromospheric lines of, say, He II are limited to layers bounded above by the corona and below by the photosphere). In finite atmospheres two physically distinct behaviors are found, depending on whether the atmosphere is *effectively thick* or *effectively thin*. If $T \gg \Lambda$, then photons from the slab center will not escape before they thermalize; in this case $S_i(0)$ will attain its semi-infinite atmosphere value for the corresponding value of ϵ , and will approach B at depths $\gtrsim \Lambda$ from the surfaces. If, however, $T \ll \Lambda$, then the solution never thermalizes, and $S_i(\tau)$ becomes proportional to the local creation rate—i.e., $S_i(\tau) = \epsilon B f(\tau)$ where $f(\tau)$ is independent of ϵ for a given T .

An estimate of S_i at slab-center can be obtained as follows [see also (28)]. The ratio of the *total* number of emissions along a column through the slab to those *thermally created* must be equal to the mean number of times, $\langle N \rangle$, a photon is scattered before it escapes or is destroyed, i.e.,

$$\begin{aligned} \langle N \rangle &= \int_{-\infty}^{\infty} dv (4\pi h\nu\phi_v) \int_0^T S_i(\tau) d\tau / \int_{-\infty}^{\infty} dv (4\pi h\nu\phi_v) \int_0^T \epsilon(\tau) B(\tau) d\tau \\ &= \int_0^T S_i(\tau) d\tau / \int_0^T \epsilon(\tau) B(\tau) d\tau \end{aligned} \quad (11-39)$$

Here we have used the definition $\eta_v = \chi_v S_v$, and noted that S_i is frequency-independent. For a finite slab the dominant photon loss-mechanism is escape, hence $\langle N \rangle \sim [P_e(T)]^{-1}$; at slab center $P_e(T) \approx [2P_e(\frac{1}{2}T)]_\infty$, where the subscript denotes the escape probability from the indicated depth in a semi-infinite slab, and the factor of two accounts for losses through both faces. To obtain an order-of-magnitude estimate from equation (11-39), we replace $S_i(\tau)$ with $S_{\max} = S(\frac{1}{2}T)$ and assume ϵB is constant so that $\langle N \rangle \approx S_{\max}/(\epsilon B)$. Then, using (11-24) and (11-25) to calculate $P_e(T)$, and again ignoring numerical factors of order unity, we find

$$S_{\max} \approx \epsilon T (\ln T)^{\frac{1}{2}} B \quad (\text{Doppler}) \quad (11-40a)$$

$$S_{\max} \approx \epsilon (T/a)^{\frac{1}{2}} B \quad (\text{Voigt}) \quad (11-40b)$$

$$\text{and} \quad S_{\max} \approx \epsilon T^{\frac{1}{2}} B \quad (\text{Lorentz}) \quad (11-40c)$$

The behavior described above is seen very clearly in the numerical results (53) shown in Figure 11-3, which gives $S_i(\tau)$ for lines with Doppler profiles ($a = 0$), for various values of ϵ , in an atmosphere with $T = 10^4$. The dashed curve gives the solution for a semi-infinite atmosphere with $\epsilon = 10^{-4}$. It can be seen that for $\epsilon \geq 10^{-4}$ the solutions closely resemble semi-infinite

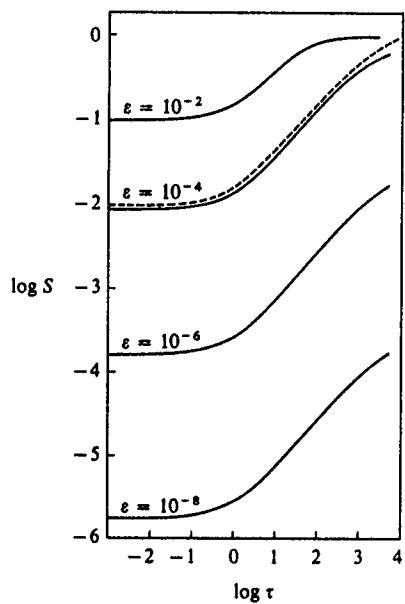


FIGURE 11-3
Line source functions in finite atmospheres with (total thickness) $T = 10^4$ and $B = 1$, for a line with a pure Doppler profile ($a = 0$). Dashed curve corresponds to the semi-infinite atmosphere solution with $\epsilon = 10^{-4}$. Note that $S_i(\tau)$ is symmetric about $T/2$ (not shown owing to use of a logarithmic scale for abscissa). From (53), by permission.

atmosphere solutions at the corresponding ϵ , while for $\epsilon < 10^{-4}$ the atmosphere becomes effectively thin and S_i falls below the corresponding semi-infinite-case curve, and, in fact, scales linearly with ϵ . Emergent intensities (53) are shown in Figure 11-4 for lines with $\epsilon = 10^{-4}$, and for various values of a and T . For $T = \infty$, an absorption line is obtained in every case, with central intensity independent of a . In finite atmospheres, emission lines are obtained, for the line wing becomes completely transparent for sufficiently large x , and the intensity must go to zero. At smaller x the intensity rises rapidly, and, for effectively thick atmospheres, saturates to the semi-infinite atmosphere value. Finally, in the line core, scattering leads to a self-reversal. The profiles shown in Figure 11-4 strongly resemble those from laboratory emission sources with saturated lines, and from hot chromospheric layers above a relatively cool photosphere.

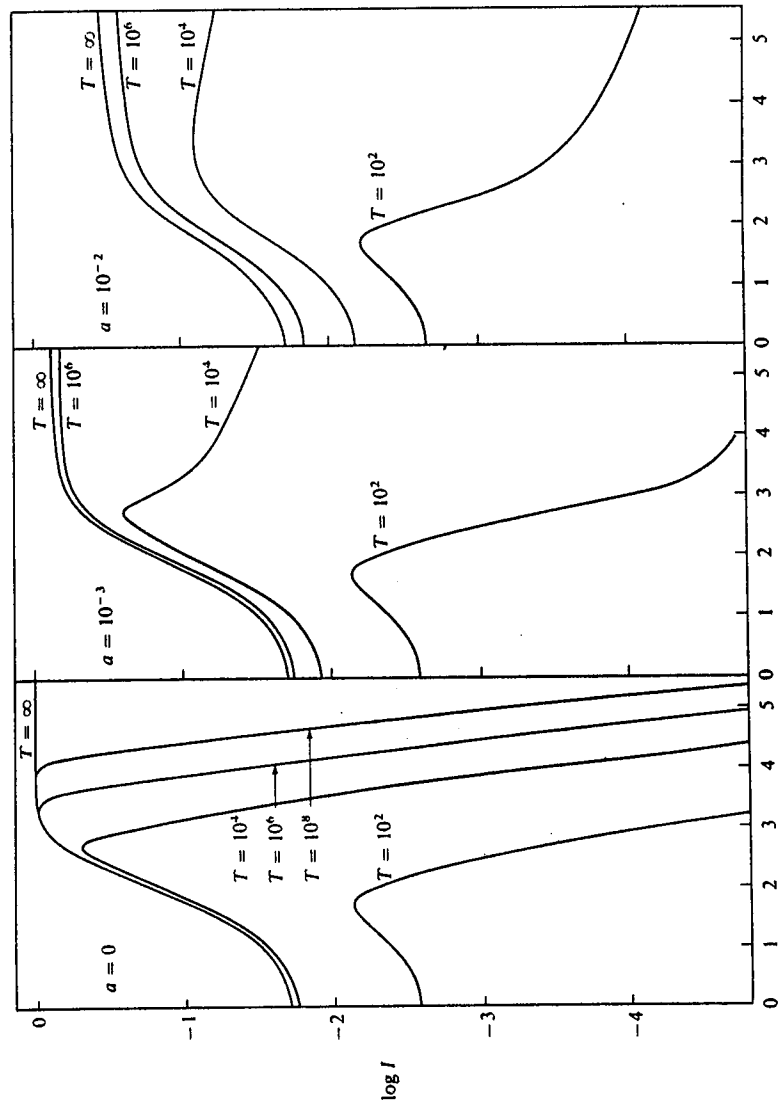


FIGURE 11-4
Emergent intensity from finite and semi-infinite atmospheres in Doppler and Voigt profiles with $\epsilon = 10^{-4}$. From (53), by permission.

THE EFFECTS OF AN OVERLAPPING CONTINUUM

All of the discussion presented thus far in this section has been based on the assumption that the only opacity source is the line itself. In virtually all situations of astrophysical interest, however, the line will be superposed on a background continuum arising from bound-free absorption by other levels of the atom, or by other atomic species. As was noted in §11-1, the presence of a background continuum affects the destruction probability P_d , and sets an upper bound on the photon mean-free-path and destruction length. We therefore expect the thermalization depth to have an upper bound set by continuum processes. Furthermore, the continuum provides an additional source of emission into the line. A detailed study of the line-formation problem with a background continuum has been presented in (315) for idealized problems similar to those considered above in the no-continuum case; we shall summarize some of the results of this work in the following paragraphs.

For simplicity we shall consider a semi-infinite atmosphere, and assume depth-independence for the line and continuum opacities χ_l and χ_c , the line profile ϕ_x , the line thermalization parameter ε , and the Planck-function B (all of these assumptions may be dropped if numerical techniques such as the Feautrier or Rybicki methods are employed). The transfer equation is

$$\mu(dI_x/dz) = -(\chi_c + \chi_l\phi_x)I_x + \chi_l\phi_x S_l + \chi_c B \quad (11-41)$$

Defining the optical depth in terms of the line opacity, $d\tau \equiv -\chi_l dz$, which implies that the continuum is regarded as a perturbation, and writing $r \equiv \chi_c/\chi_l$, equation (11-41) becomes

$$\mu(dI_x/d\tau) = (\phi_x + r)(I_x - S_x) \quad (11-42)$$

where $S_x \equiv \frac{(1-\varepsilon)\phi_x}{(\phi_x + r)} \int_{-\infty}^{\infty} \phi_x J_{x'} dx' + \frac{(\varepsilon\phi_x + r)}{(\phi_x + r)} B$

$$= (1 - \xi_x) \int_{-\infty}^{\infty} \phi_x J_{x'} dx' + \xi_x B \quad (11-43)$$

and $\xi_x \equiv (\varepsilon\phi_x + r)/(\phi_x + r) \quad (11-44)$

It is easy to see that ξ_x is the *total destruction probability* for a photon at frequency x , for it is the sum of (a) the probability that a photon is absorbed in the line, $\phi_x/(\phi_x + r)$, multiplied by ε , the probability that a line photon is destroyed by collisions, and (b) the probability that the photon is absorbed in the continuum, $r/(\phi_x + r)$, multiplied by unit probability of

destruction. The formal solution of the transfer equation (11-42) yields

$$\begin{aligned} J_x(\tau) &= \frac{1}{2} \int_0^\infty S_x(t) E_1 |(t - \tau)(\phi_x + r)| (\phi_x + r) dt \\ &= \frac{1}{2} \phi_x \int_0^\infty S_l(t) E_1 |(t - \tau)(\phi_x + r)| dt + \frac{1}{2} rB \int_0^\infty E_1 |(t - \tau)(\phi_x + r)| dt \end{aligned} \quad (11-45)$$

The solution given by equation (11-45) could be substituted into (11-43) to produce an integral equation for the total source function $S_x(\tau)$, but the resulting equation would be two-dimensional (τ and x), and would be impractical to solve. Alternatively we can write an equation for $S_l(\tau)$; if the line source function is known, we can compute $S_x(\tau) = [\phi_x S_l(\tau) + rB]/(\phi_x + r)$ as desired. To obtain the equation for $S_l(\tau)$, the integral $\int \phi_x J_x dx$ is calculated from equation (11-45) and the result substituted into equation (11-11) to give

$$S_l(\tau) = (1 - \varepsilon)(1 - \delta) \int_0^\infty S_l(t) K_{1,r} |t - \tau| dt + (1 - \varepsilon) \delta B \int_0^\infty L_{1,r} |t - \tau| dt + \varepsilon B \quad (11-46)$$

where $\delta \equiv r \int_{-\infty}^{\infty} \phi_x (\phi_x + r)^{-1} dx \quad (11-47)$

$$K_{1,r}(s) \equiv \frac{1}{2} (1 - \delta)^{-1} \int_{-\infty}^{\infty} E_1 [(\phi_x + r)s] \phi_x^2 dx \quad (11-48)$$

and $L_{1,r}(s) \equiv \frac{1}{2} r \delta^{-1} \int_{-\infty}^{\infty} E_1 [(\phi_x + r)s] \phi_x dx \quad (11-49)$

The particular choice of coefficients in front of the integrals defining the two kernel functions was made to assure *normalization* of the kernels.

Exercise 11-7: (a) Derive equation (11-46). (b) Show that $\lim_{r \rightarrow 0} (\delta/r) = \infty$, $\lim_{r \rightarrow 0} (1 - \delta) = 1$, and hence $\lim_{r \rightarrow 0} L_{1,r}(\tau) = 0$ and $\lim_{r \rightarrow 0} K_{1,r}(\tau) = K_1(\tau)$ where $K_1(\tau)$ is defined by equation (11-19). (c) Show that $K_{1,r}$ and $L_{1,r}$ are normalized such that $\int_0^\infty K_{1,r}(\tau) d\tau = \frac{1}{2}$ and $\int_0^\infty L_{1,r}(\tau) d\tau = \frac{1}{2}$. (d) In view of (c), show that, for $\tau \rightarrow \infty$, where $S_l(\tau)$ is slowly varying and hence can be removed from the integral, $S_l(\tau) \rightarrow B$.

The physical significance of equation (11-46) becomes clear if we introduce the *average destruction probability*

$$\bar{\xi} \equiv \int_{-\infty}^{\infty} \phi_x \xi_x dx = \delta + \varepsilon(1 - \delta) \quad (11-50)$$

for then $(1 - \xi) = (1 - \varepsilon)(1 - \delta)$ and we can rewrite equation (11-46) as

$$\begin{aligned} S_i(\tau) &= (1 - \xi) \int_0^\infty S_i(t) K_{1,r} |t - \tau| dt + (\xi - \varepsilon) B \int_0^\infty L_{1,r} |t - \tau| dt + \varepsilon B \\ &\equiv (1 - \xi) \int_0^\infty S_i(t) K_{1,r} |t - \tau| dt + \xi B_{\text{eff}}(\tau) \end{aligned} \quad (11-51)$$

In the first form of equation (11-51), the first term obviously represents scattering in the line, with a total photon destruction probability given by ξ . The second term represents photons fed into the line from the continuum, and the third term represents photons created by collisional processes. As in the pure-line case, the depth-variation of the source function will be determined by the properties of the kernel functions, and thermalization properties of S_i can be derived from a mathematical analysis of the asymptotic forms of $K_{1,r}$ and $L_{1,r}$ (315). On the other hand, the second form of equation (11-51) shows that the problem with a continuum is of the same form as the pure-line case, except that the coupling constant between the radiation and the thermal pool is ξ , not ε . Indeed, exploiting the same line of reasoning as before, but using ξ for P_d , one finds that the *thermalization depth is again given by equations (11-26)*, but with ε replaced by ξ . Values of ξ and Λ , for $\varepsilon = 10^{-6}$ and for various values of r and a , are presented in Table 11-1. The striking result seen there is that ξ can greatly exceed ε , even when $r \leq \varepsilon$, with a consequent dramatic decrease in Λ . These results show that by inhibiting photon transfer in the line wings, the continuum can dominate line thermalization. Note also that whenever $r \geq \varepsilon$, then ξ is already sufficiently large to assure that $\Lambda < r^{-1}$, as it must be, because we know from physical considerations that over distances greater than r^{-1} thermalization

TABLE 11-1
Average Photon Destruction Probability ξ and Thermalization Depth Λ for a Line with Overlapping Continuum ($\varepsilon = 10^{-6}$)

r	a							
	0		10^{-3}		10^{-2}			
	ξ	Λ	ξ	Λ	ξ	Λ	ξ	Λ
0	10^{-6}	1×10^6	10^{-6}	10^9	10^{-6}	10^{10}		
10^{-7}	1.79×10^{-6}	5.6×10^6	1.87×10^{-3}	2.9×10^6	5.71×10^{-5}	3.1×10^7		
10^{-6}	8.26×10^{-6}	1.2×10^5	5.72×10^{-3}	2.1×10^5	1.78×10^{-4}	3.2×10^5		
10^{-5}	6.69×10^{-5}	1.5×10^4	1.85×10^{-4}	2.9×10^4	5.63×10^{-4}	3.2×10^4		
10^{-4}	5.85×10^{-4}	1.7×10^3	7.84×10^{-4}	1.6×10^3	1.83×10^{-3}	3.0×10^3		
10^{-3}	4.98×10^{-3}	2.0×10^2	5.23×10^{-3}	3.7×10^1	7.25×10^{-3}	1.9×10^2		

SOURCE: (315), by permission.

in the continuum will occur; equations (11-26) with ε replaced by ξ are thus consistent.

To estimate the source function at the surface we can again use the similarity of equation (11-51) to (11-18) to infer that there exists a relation of the form

$$S_i(0) = \xi^{\frac{1}{2}} B_{\text{eff}} \quad (11-52)$$

where B_{eff} is an appropriate average of $B_{\text{eff}}(\tau)$ over a thermalization length. It is apparent from the discussion given above that whenever ξ exceeds ε (either because $r > \varepsilon$ or because extensive line wings assure that $\xi > \varepsilon$ even though $r < \varepsilon$), then both the destruction and creation terms (i.e., B_{eff}) are dominated by the continuum, and the line is said to be *continuum controlled*. This implies that $S_i(0)$, in particular, is set by the continuum even though the line opacity and line source function in the line core exceed the continuum terms. This is yet another manifestation of the fact, noted earlier, that the surface value of the source function is controlled by the line wings.

Numerical solutions for $S_i(\tau)$, in a semi-infinite atmosphere with $B = 1$ and $\varepsilon = 10^{-6}$, obtained using the method of discrete ordinates (315), are shown in Figures 11-5 and 11-6. It is easily seen that even modest values of

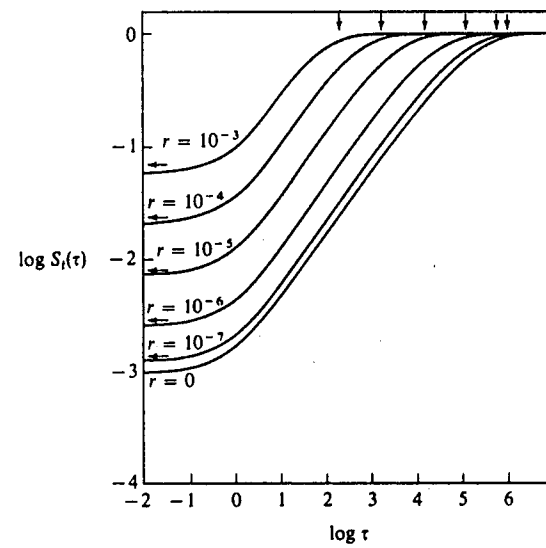


FIGURE 11-5
Line source functions in a semi-infinite atmosphere for a two-level atom with $\varepsilon = 10^{-6}$ and a pure Doppler profile ($a = 0$), with an overlapping continuum having various values of r . From (315), by permission.

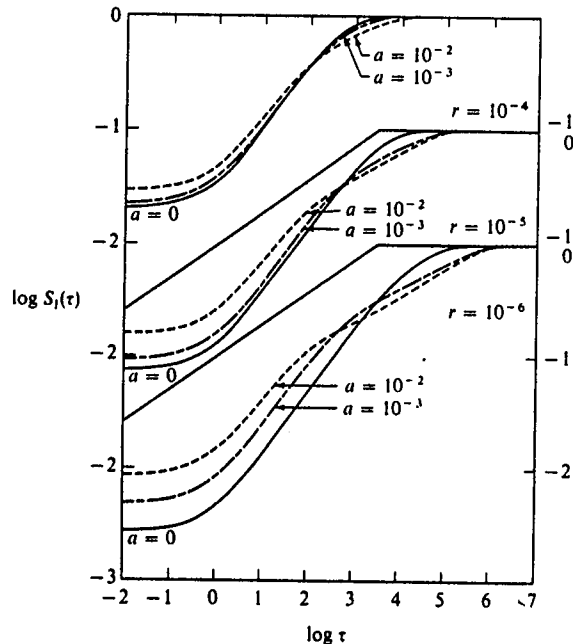


FIGURE 11-6
Line source functions in a semi-infinite atmosphere for a two-level atom with $\varepsilon = 10^{-6}$ and an overlapping continuum with various values of r , showing effects of different line profiles. From (315), by permission.

r produce major changes in the source function; the effects are even more striking in finite slabs (315). The results in Figure 11-5 pertain to a pure Doppler profile; the vertical arrows indicate the predicted thermalization depths listed in Table 11-1, and the horizontal arrows show ξ^{\pm} , the value of $S_l(0)$ if $B_{\text{eff}} \equiv 1$. For Voigt profiles (Figure 11-6) a fairly good estimate for $S_l(0)$ is obtained if one adopts

$$B_{\text{eff}} = (\Lambda/\alpha)^{-1} \int_0^{(\Lambda/\alpha)} B_{\text{eff}}(\tau) d\tau \quad (11-53)$$

with α chosen to be a little larger than 3; this choice allows for the strong decrease in the true weighting function with depth. For *finite* slabs, a first approximation to $S_{l,\max}$ at slab center is given by equations (11-40) with ε replaced by ξ ; this accounts for photons emitted by the continuum.

In real stellar atmospheres the effects of a background continuum on line-formation and thermalization are usually major. For early-type stars

only the strongest lines have values of r as small as 10^{-4} or 10^{-3} , and continuum terms therefore are generally dominant. On the other hand, the H and K lines of Ca II in the solar spectrum have $r \approx 10^{-9}$, and hence their thermalization is essentially independent of the overlapping continuum.

EFFECTS OF DEPTH-VARIABLE THERMALIZATION PARAMETERS AND LINE PROFILES

In the idealized problems considered thus far in this section it has been assumed, for the sake of simplicity, that all of the quantities B , r , ε , and ϕ_v are independent of depth, whereas in real stellar atmospheres they may all be strong functions of depth. These variations can, of course, markedly affect the line-formation process, the behavior of the source function, and computed line profiles. To account for these complications in attempts to model accurately real stellar spectra, recourse must be had to direct numerical methods such as those described earlier in this chapter. But physical insight can be gained from a study of simple parameterizations of the variations of some of the quantities mentioned above. A discussion of the extremely important effects of Planck function variations will be deferred to §11-3, where line-formation in the presence of a chromospheric temperature rise will be described. Variations in the parameter r can be important, but are not easy to summarize in a few words; see (18, Chap. 3) for further discussion. We shall concentrate here on the effects of depth-variations of ε and ϕ_v .

The collisional de-excitation parameter ε is proportional to the electron density, and hence must reflect the rise of the density with depth in the atmosphere. If the atmosphere is supposed to be essentially isothermal, then hydrostatic equilibrium implies that the total density increases linearly with m , the column-mass; if further we suppose that (χ/ρ) is essentially constant, then τ is also proportional to m . Then in an early-type star where the material is appreciably ionized, we expect n_e to be proportional to τ ; in a later-type star the material may be neutral in the outer layers and may then abruptly ionize at some depth, in which case a much more sudden rise in n_e (and ε) may occur. Even though an actual numerical solution is required to determine $S_l(\tau)$ with precision when ε is variable, it is reasonable on physical grounds that we should still expect thermalization to occur at a depth Λ where $P_e(\Lambda) \approx P_d(\Lambda)$. To illustrate the usefulness of this idea, suppose a rapid rise in ε occurs, from some value ε_1 to higher value ε_2 , at a particular depth τ_0 in an atmosphere with r , B , and ϕ all constant. Then if $\tau_0 > 1/\varepsilon_1$ (for a Doppler profile) it is clear that the line will already have thermalized, and hence the rise in ε has no effect. In this case $S_l(0)$ will equal $\varepsilon_1^{\pm} B$. Conversely, suppose that $\tau_0 < 1/\varepsilon_2$. Then the line source function thermalization will have been delayed by the low value of ε at the surface to a predicted depth of $1/\varepsilon_1$; but at that depth ε already equals $\varepsilon_2 > \varepsilon_1$. Hence the line will

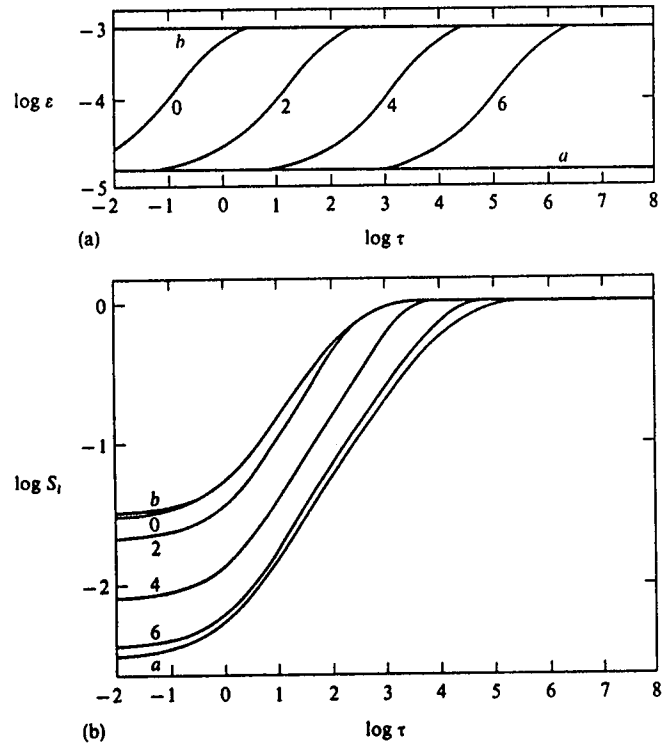


FIGURE 11-7
 (a) Variation of ε with depth: curves are labeled with $\log \tau_0$, and $\varepsilon(\tau) = 10^{-3}[1 - 0.99 \exp(-\tau/\tau_0)]$. (b) Line source function in a semi-infinite atmosphere with $B = 1$, for a line with a pure Doppler profile and $\varepsilon(\tau)$ as shown in (a). Curves labeled "a" and "b" correspond to constant values of ε of 10^{-5} and 10^{-3} respectively. From (284, 101).

behave as if ε were constant at $\varepsilon \equiv \varepsilon_2$, and $S_l(0)$ will equal $\varepsilon_2^{\frac{1}{2}}B$. These qualitative expectations are confirmed by detailed calculations (284, 101) such as those shown in Figure 11-7 where ε is assumed to have the form $\varepsilon(\tau) = 10^{-3}[1 - 0.99 \exp(-\tau/\tau_0)]$. Notice that, when $\tau_0 > 10^5$, S_l behaves as if $\varepsilon \equiv 10^{-5}$, whereas if $\tau_0 \lesssim 10^2$, S_l behaves as if $\varepsilon \equiv 10^{-3}$.

A change in the form of the line profile alters the way photons get redistributed into the line wings, and their probability of escape. Numerical studies (320; 18, 51) have revealed a number of interesting effects of profile depth-variations upon the line source function. Suppose, for example, the Doppler width rises sharply near the surface in an atmosphere with $B =$

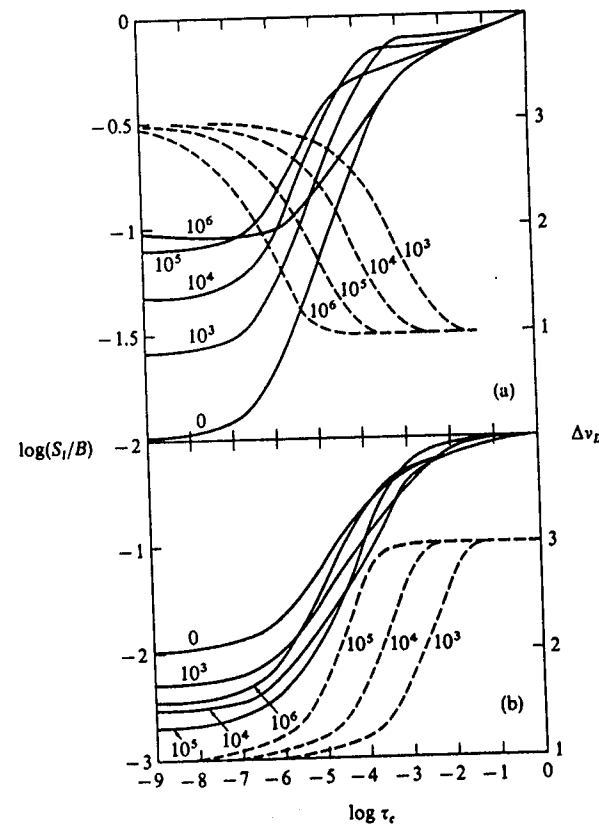


FIGURE 11-8
 Line source functions in a semi-infinite atmosphere with $B = 1$, for a line with $\varepsilon = 10^{-4}$, $r = 10^{-6}$, $a = 10^{-3}$, and a depth-variable Doppler width. (a) Doppler width rising toward surface, $\Delta v_D(\tau) = 1 + 2 \exp(-\alpha \tau_s)$. (b) Doppler width decreasing toward surface, $\Delta v_D(\tau) = 3 - 2 \exp(-\alpha \tau_s)$. Curves are labeled with parameter α . Curves labeled "0" have constant Doppler width. Ordinates: Left-hand scale and solid curves give $\log(S_l/B)$; right-hand scale and dashed curves give Δv_D . From (18, 52), by permission.

constant (see Figure 11-8a). Then we find that the surface value $S_l(0)$ is increased markedly because the broader line-wings can now intercept radiation from deeper layers. As the position of the rise in Δv_D moves deeper in the atmosphere, the surface effect diminishes, basically because the surface layer becomes more and more opaque in the wings, and the bright underlying

continuum radiation becomes more attenuated. At the same time, the source function at great depth also increases, basically because the higher opacity in the line-wings in the surface layer impedes the escape of radiation from below; this is sometimes referred to as the *reflector effect*. The effect at depth is greater, the thicker the upper layer (until, of course, the rise lies below the point of thermalization). Notice in Figure 11-8a that when $\alpha = 10^6$ the upper layer is optically thin, and thus there is essentially no reflector effect even though the surface rise is largest.

When the Doppler width decreases sharply at the surface, the value of $S_l(0)$ drops because the narrower profile no longer intercepts bright radiation in its wings. Radiation trapping is also reduced in lower layers, and hence S_l decreases there as well. At very great depth, however, the effect is the opposite, and S_l actually rises a little above its value for constant Δv_D , because now the decreased bandwidth available to the lines implies a decreased escape probability.

It must also be noted that, in addition to changing $S_l(\tau)$, variations in the absorption profile change the run of optical depth, at a given frequency, with physical depth. In view of the Eddington-Barbier relation, it is obvious that this implies a change in the "mapping" of S_l into $I_v(0)$, and hence in the emergent intensity distribution in the line profile, and its center-to-limb behavior [see, e.g., (26)].

11-3 The Two-Level Atom with Continuum

THE SOURCE FUNCTION

The discussion given in the preceding sections of this chapter is based on a very schematic and admittedly restrictive atomic model. Naturally the true situation for any real atom is more complicated. To introduce some of the physically important effects while retaining analytical simplicity, let us now consider an atomic model consisting of two bound states and a continuum. This model provides at least a rough representation of reality for resonance lines and also for subordinate lines when the resonance lines are in radiative detailed balance. The addition of the continuum greatly increases the number of processes that may take place. In the strict two-level case, the only processes that can occur are photoexcitations or collisional excitations from the lower to upper state, and their inverses. Now there are, in addition, photoionizations and collisional ionizations from the bound levels to the continuum, and radiative and collisional three-body recombinations to each bound level. It is clear that this is a much more general model, and we shall find that the additional physics has major implications for the line-formation process.

As before, assume complete redistribution, so that S_l is given by equation (11-4). The statistical equilibrium equations now are

$$\begin{aligned} n_l \left(B_{lu} \int \phi_v J_v dv + C_{lu} + R_{lk} + C_{lk} \right) \\ = n_u \left(A_{ul} + B_{ul} \int \phi_v J_v dv + C_{ul} \right) + n_l^*(R_{kl} + C_{lk}) \quad (11-54) \end{aligned}$$

$$\begin{aligned} \text{and } n_u \left(A_{ul} + B_{ul} \int \phi_v J_v dv + C_{ul} + R_{uk} + C_{uk} \right) \\ = n_l \left(B_{lu} \int \phi_v J_v dv + C_{lu} \right) + n_u^*(R_{ku} + C_{uk}) \quad (11-55) \end{aligned}$$

for the lower and upper levels, respectively. The photoionization and recombination rates are given by equations (5-66) and (5-67). Solving equations (11-54) and (11-55) for (n_l/n_u) , substituting into equation (11-4), and making use of the Einstein relations we obtain

$$S_l = \left[\int \phi_v J_v dv + \varepsilon B_v(T) + \theta \right] / (1 + \varepsilon + \eta) \quad (11-56)$$

where ε is given by equation (11-7),

$$\eta \equiv \frac{(R_{uk} + C_{uk})n_l^*(R_{kl} + C_{lk}) - g_l(R_{lk} + C_{lk})n_u^*(R_{ku} + C_{uk})/g_u}{A_{ul}[n_l^*(R_{kl} + C_{lk}) + n_u^*(R_{ku} + C_{uk})]} \quad (11-57)$$

$$\text{and } \theta \equiv \left(\frac{2hv^3}{c^2} \right) \left(\frac{g_l}{g_u A_{ul}} \right) \frac{(R_{lk} + C_{lk})n_u^*(R_{ku} + C_{uk})}{[n_l^*(R_{kl} + C_{lk}) + n_u^*(R_{ku} + C_{uk})]} \quad (11-58)$$

Equation (11-56) was first derived by Thomas (622) as an extension of earlier work by Milne (416, 159–164) and Strömgren (613), and was studied extensively in an important series of papers by Jefferies and Thomas (335; 336; 623; 337).

Exercise 11-8: Derive equations (11-56) through (11-58) in detail.

Despite the apparent complexity of these expressions, each term admits a simple interpretation. Consider the numerator of equation (11-56). The first term again represents the scattering reservoir. The second term is the thermal source, giving the rate at which photons are created by collisional excitation; note that this term depends upon the local value of T_e , the *electron kinetic temperature*. The third term is proportional to the total rate at which electrons are ionized from the ground state to the continuum,

times the fraction that recombines to the upper state and thus becomes available for emission into the line by radiative decay to the ground state. Similarly, in the denominator, the second term accounts for photons destroyed by collisional de-excitation of the upper state. The third term is a new sink term that is proportional to the total ionization rate from the upper state times the fractional recombination rate to the lower state; this term clearly accounts for the destruction of potential line photons via the continuum processes. We thus find all of the basic physics of the situation represented clearly in the source function.

Further insight follows from rewriting θ as ηB^* , where B^* is found to be

$$B^* = \left(\frac{2hv^3}{c^2} \right) \left\{ \left(\frac{n_i^* g_u}{n_u^* g_i} \right) \left[\frac{(R_{uk} + C_{uk})(R_{kl} + C_{lk})}{(R_{lk} + C_{lk})(R_{ku} + C_{uk})} \right] - 1 \right\}^{-1} \quad (11-59)$$

Exercise 11-9: Verify equation (11-59).

It is clear that B^* bears a formal resemblance to the Planck function, and, in fact, we can think of it as $B^* = B_v(T_e)$, where T_e is a characteristic *radiation temperature* whose value is set by the photoionization and recombination rates in the two bound-free continua. This radiation temperature can, in general, be quite different from T_e . At great depth in the atmosphere where the continua are optically thick, $J_v \rightarrow B_v(T_e)$; then $R_{lk} \rightarrow R_{lk}^* = R_{kl}^*$, and $R_{uk} \rightarrow R_{uk}^* = R_{ku}^*$, so that $B^* \rightarrow B_v(T_e)$, as expected, and $S_i \rightarrow B_v(T_e)$. But near the surface, the continua may become transparent (while the line remains optically thick) and the continuum radiative rates become essentially fixed. Depending on the relation of the radiation temperature (which characterizes J_v emerging from $\tau_c \sim 1$) to the local electron temperature, quite distinct situations emerge. For example, suppose that collisions are negligible, and that $R_{lk} > R_{kl}$ while $R_{ku} > R_{uk}$ (i.e., suppose that a relatively cool medium is irradiated by a "hot" radiation field in the ground-state continuum). Then it is clear that $B^* > B_v(T_e)$, and that S_i will be larger than the value it would have had by coupling to the thermal pool; the excess emission comes from a preferential depopulation of the lower state into the upper via the continuum, followed by radiative de-excitation in the line. If the line is an absorption line, an increase in S_i tends to *weaken* it; taken to the extreme limit, this is the mechanism that produces the photoionization-recombination-cascade emission spectrum in a nebula. If the inequalities posed above are reversed, then the upper state is selectively depopulated into the lower, and S_i decreases; if the line is an absorption line, it will *strengthen*.

The two essential points that have emerged from the above analysis are the following. (a) The source function for a given line contains terms in *other* transitions (the two continua for the present model). This result is quite generally true and carries over to the multilevel case (see §12-1). (b) The

new terms do not couple S_i to the local thermal pool, characterized by T_e , as do collisions, but rather to a radiation temperature that may be markedly hotter or cooler than the local kinetic temperature.

CLASSIFICATION OF LINES

In view of the fundamentally differing natures of the various source and sink terms that appear, we may expect that line-transfer problems may show substantially different characteristics depending on which terms provide the dominant contributions to S_i . Thomas has suggested (622; 626, 174) a classification of lines into broad categories by consideration of which terms are the largest for different atoms in typical stellar-atmosphere regimes. For example, if $\varepsilon > \eta$ and $\varepsilon B_v > \eta B^*$, the line is called *collision dominated*; here S_i couples to T_e . On the other hand, if $\eta > \varepsilon$ and $\eta B^* > \varepsilon B_v$, the line is *photoionization dominated*, and the line couples to a characteristic $T_v \neq T_e$. Intermediate cases where, say, $\varepsilon > \eta$ but $\eta B^* > \varepsilon B_v$, or vice versa, are called *mixed domination* lines. The recognition of these classes of lines represents a considerable advance over the rather ill-defined classical division of lines into "absorption" and "scattering" categories, and has led to important insights about line-formation. In particular, the emergent profiles for lines in these classes are quite different when a chromospheric temperature rise occurs in the outer layers of the atmosphere.

The category to which any particular line belongs depends (via the atomic cross-sections involved) upon the structure of the ion from which it arises, and upon the structure of the atmosphere (because of the dependence of the relevant rates upon atmospheric parameters such as temperature, density, and incident radiation fields). Different lines of the same ion will, in general, fall into different classes, and a comprehensive *a priori* classification is not possible; rather, each case must be examined in turn. Broad groupings of lines in a solar-type atmosphere have been suggested by Thomas; these are displayed in Table 11-2, and can be understood qualitatively as follows. The resonance lines of the singly ionized metals are collision dominated because the excitation energy is only a few electron volts (compared to a thermal

TABLE 11-2
Categories of Line Source Functions in a Solar-Type Atmosphere

Collision dominated	Photoionization dominated
Resonance lines of singly ionized metals (Mg^+ , Ca^+ , Sr^+ , etc.)	Resonance lines of neutral metals
Resonance lines of H and other nonmetals (C, N, O, etc.)	Hydrogen Balmer lines

SOURCE: Adapted from (623; 626, 174).

energy of about 0.5–1 eV), while the ionization energies are 11–15 eV; recalling that both the collision and photoionization rates scale as $\exp(-E_0/kT)$, it is plausible that the collisions should prevail. Even for hydrogen, where E_0 in $L\alpha$ is 10 eV, the collision rates dominate because the solar u.v. radiation is weak and the photoionization rate is small. In contrast, for the hydrogen Balmer lines and the neutral metals, the relevant photoionization edges lie in regions where the solar radiation field is intense, and the photoionization rates prevail over collision rates. The sodium D-lines are an exception because of an unusually large collision cross-section (284, 333; 284, 347); this example serves as a warning that the broad classes listed are *illustrative*, and detailed analysis is needed in each case. In a higher temperature regime (e.g., in an O-star) some of the remarks just made are no longer valid, and lines switch categories. For example, the radiation field in the Lyman continuum becomes extremely intense (the hydrogen is virtually completely ionized), and the hydrogen Lyman lines become photoionization dominated. The higher subordinate lines now have energies $E_0 \lesssim kT$ (~ 3 eV at O-star temperatures), and are relatively weak, hence are formed in deeper, denser layers; this tends to lead to collision domination of the subordinate series.

LINE-FORMATION IN THE PRESENCE OF A CHROMOSPHERE

The great physical importance of the division of lines into the two broad categories described above becomes strikingly apparent when we consider the nature of the source function variation, and emergent line profile, in an atmosphere with a chromospheric temperature rise outward. The basic point is that collision-dominated lines are linked to the *local electron kinetic temperature*, while photoionization-dominated lines are not. The latter couple instead to a *radiation temperature* characteristic of the energy distribution (emitted at some other point in the atmosphere) in the continua of the upper and lower levels. We therefore expect collision-dominated lines to be at least partly responsive to the local temperature, and to exhibit, in their profiles, features attributable to the outward temperature rise. On the other hand, we expect photoionization-dominated line-profiles to be insensitive to variations in local parameters (in particular, to variations in T_e). The strong dichotomy of behavior just described was clearly demonstrated in the pioneering work of Jefferies and Thomas (336). They showed that these considerations explained the observed presence of emission cores in lines such as the H and K lines of Ca^+ (and the analogous lines of Mg^+), and their simultaneous absence in the hydrogen Balmer lines.

In their work Jefferies and Thomas adopted a schematic continuum source function of the form

$$S_c(\tau) = B_v(T_e) = S_i(1 + \alpha\tau_e + \beta e^{-\gamma\tau_e}) \quad (11-60)$$

which provides an approximate representation of a temperature distribution that has: a uniform gradient in the photosphere; a plateau at a minimum temperature at some characteristic depth (they used $T_{\min} \approx 4000^\circ\text{K}$ at $\tau_c \approx 10^{-2}$); and then a steep outward gradient mimicking the sharp chromospheric rise. The transfer equation was solved in the Eddington approximation:

$$\frac{1}{3} (d^2 J_v/d\tau^2) = (\phi_v + r)^2 [J_v - (\phi_v + r)^{-1}(rS_c + \phi_v S_i)] \quad (11-61)$$

using the method of discrete ordinates, for a Doppler profile and for typical values of r , ε , η , and B^* .

Results for a collision-dominated line ($\eta \equiv 0$) with $\varepsilon = 10^{-4}$, $r = 10^{-4}$, and various choices for the continuum source function are shown in Figure 11-9. Note that at great depth S_i thermalizes to S_c , but as the wings begin to become transparent ($\tau_c \lesssim 1$), S_i drops below S_c . Proceeding outward, S_i rises very steeply at $\tau_c \approx 10^{-2}$. The line source function tries to follow this rise through collisional coupling, and actually does increase outward, but ultimately the effects of scattering dominate, and, at the surface, S_i lies about three orders of magnitude below $B_v(T_e)$. It follows from the Eddington-Barbier relation that the depth-variation of $S_i(\tau)$ should be reflected in the frequency-variation of the emergent intensity. The computed emergent

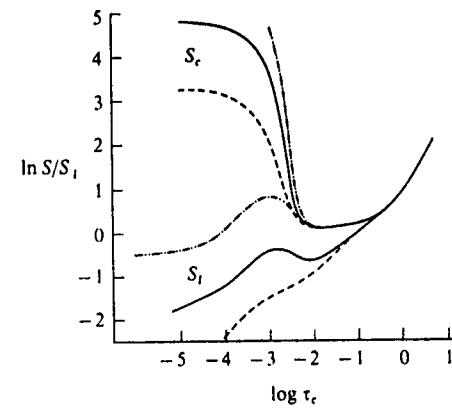


FIGURE 11-9
Line source functions for a collision-dominated line in a semi-infinite atmosphere with a chromospheric temperature rise. Upper curves show continuum source function S_c , and lower curves show corresponding line source functions S_i . In all cases $\varepsilon = 10^{-4}$ and $r = 10^{-4}$. From (336) by permission.

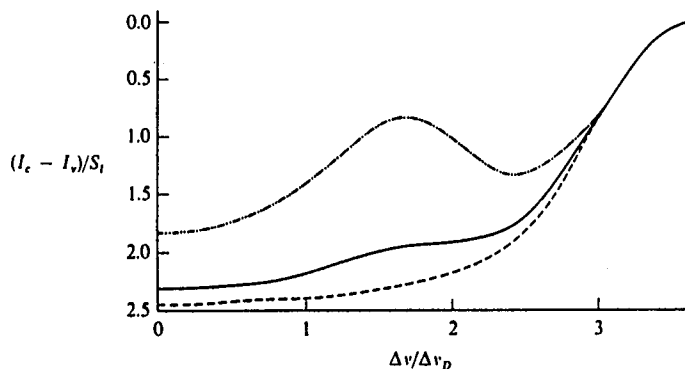


FIGURE 11-10
Line profiles for a collision-dominated line in a semi-infinite atmosphere with a chromospheric temperature rise. Curves are coded to correspond to those in Figure 11-9. From (336), by permission.

intensity is shown in Figure 11-10; only half of the profile (which is symmetric about line-center) is shown. Note that the lines show an emission peak near ± 1.5 Doppler widths, with a central absorption reversal; lines of this form are called *doubly reversed*. The overall variation of intensity within the line is in good qualitative agreement with the observed behavior in the solar Ca II *H*- and *K*-lines and the corresponding lines of Mg II. Numerous other calculations, with a chromospheric temperature rise, for other choices (sometimes including depth-variations) of ϵ , a , r , ϕ_v , and different parameterizations of $B_v(\tau)$ can be found in the literature [see, e.g., (284, 101; 26; 27; 18, 45–48)]. All show the same kind of behavior as that shown in Figure 11-10, and some yield semiquantitative agreement with the solar data; excellent quantitative fits to the observations are obtained when multi-level calculations, using realistic atmospheric models and atomic models for Ca⁺, are employed (see §12-1).

The behavior of photoionization-dominated lines, for the same assumed Planck function, contrasts strongly with that of collision dominated lines. Results for a line with $\epsilon = 0$, $\eta = 10^{-2}$, and $r = 10^{-4}$ are shown in Figure 11-11. At very great depth, $S_l \rightarrow S_c$ when the line thermalizes in the continuum. Proceeding outward, S_l remains fixed at the value set by B^* , and at a line optical depth of order $1/\eta$, shows a strong drop outward, characteristic of scattering, to a value equal to $\eta^2 B^*$. The source function shows no response whatever to the variation of $B_v(T_e)$. Note that proceeding outward, S_l first lies above S_c (because B^* has a radiation temperature set in the continua in deeper, hotter layers), and then, near the surface, lies below S_c (which rises

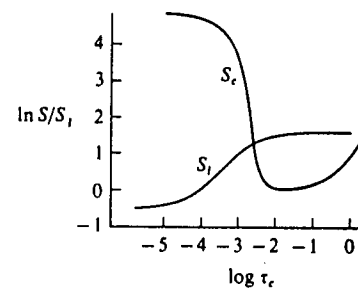


FIGURE 11-11
Source function for a photoionization-dominated line in a semi-infinite atmosphere with a chromospheric temperature rise. From (336), by permission.

rapidly to its chromospheric value). The line profile is a pure absorption feature with no hint of central emission reversal. This behavior is precisely what is observed for the Balmer lines and, in fact, the run of S_l correlates well with the empirical source function deduced by Athay and Thomas (29).

The recognition that the Ca II *H*- and *K*-lines have source functions that couple partially to the local Planck function variation led to the realization that the emission features often observed in the cores of these lines in stellar spectra contain valuable information about the temperature distribution in stellar chromospheres. If suitably analyzed, these lines provide unique diagnostic tools for the determination of the physical structure of the outer layers of solar-type stars. It is known that the intensity of the emission correlates with stellar age (675; 677), and this fact offers the possibility that by combining accurate chromospheric diagnostics with a reliable theory of stellar evolution, we may be able to infer the time-evolution of the solar chromosphere. One of the most fascinating empirical results relating to chromospheric Ca II *H* and *K*-line emission is known as the *Wilson-Bappu effect* (676), which shows that the half-intensity-width of the emission components correlates closely with stellar luminosity, over a range of 10^6 in L . Several theoretical suggestions have been made to explain this observation, but, as was early emphasized by Jefferies and Thomas (337), an understanding of the phenomenon must be based on an accurate physical picture of line-formation. Their work, and more recent efforts, have elucidated the dependence of the emission intensity and width upon the form of $T_e(\tau)$ (amplitude and depth of rise) and upon the functions ϵ , r , and ϕ_v .

Some useful insight concerning the basic properties of chromospheric emission lines can be gained from approximate scaling rules [(24; 18, 46)] such as those summarized in Table 11-3. These give estimates of the surface value, $S_l(0)$, and peak value, $S_l(\max)$, of the source function in a chromospheric slab, with a Planck-function variation given by equation (11-60) with S_1 set to unity. The rules are based on the assumption that the Doppler width is independent of depth; Doppler width variations alter the results

TABLE 11-3
Scaling Rules for Line Source Function in Finite Chromospheric Slabs

Chromospheric thickness	Doppler profile ($a < \epsilon$)		Voigt profile $\epsilon < a < 1$	
	$S_i(0)$	$S_i(\text{max})$	$S_i(0)$	$S_i(\text{max})$
Optically thin $(\gamma r)^{-1} < 1$	$\xi\beta$	$\xi\beta$	$\xi\beta$	$\xi\beta$
Effectively thin $1 < (\gamma r)^{-1} < \Lambda$	$\xi\beta(\gamma r)^{-\frac{1}{2}}$	$\xi\beta(\gamma r)^{-1}$	$\xi\beta(\gamma r a)^{-\frac{1}{2}}$	$\xi\beta(\gamma r a)^{-1}$
Effectively thick $\Lambda < (\gamma r)^{-1}$	$\xi^{\frac{1}{2}}\beta$	β	$\xi^{\frac{1}{2}}\beta$	β

SOURCE: Adapted from (18, 46), by permission.

somewhat (24) and, more importantly, strongly affect the emergent line-profile for a given $S_i(t)$. The parameters of interest for describing the run of $B_v(T_e)$ are β , the amplitude of the rise (assumed to be $\gg 1$), and γ^{-1} , the continuum depth at which the rise occurs [the corresponding line depth is $(\gamma r)^{-1}$]. If $(\gamma r)^{-1} \ll \Lambda$ (the thermalization depth), then S_i will respond only weakly to the chromospheric temperature rise; but if the inequality is reversed, a strong effect will occur. If the slab is effectively thick [i.e., $(\gamma r)^{-1} > \Lambda$, where $\Lambda = \xi^{-1}$ or $a\xi^{-2}$ for Doppler and Voigt profiles, respectively, and ξ is the total destruction probability given by equation (11-50)], then S_i saturates to β at depth and falls by a factor of $\xi^{\frac{1}{2}}$ at the surface. If the slab is optically thin, then S_i just equals the local creation term $\xi\beta$. If the slab is effectively thin, the maximum value of S_i is given by equations (11-40) with $T = (\gamma r)^{-1}$. Note that the quoted results for the Voigt profile presume that $a(\gamma r)^{-1} > 1$; if a is so small that this is not true, the line wings are negligible and the results listed for a Doppler profile apply instead. The surface value of S_i can be derived by recognizing that if $S_{i,\text{max}} \propto \xi\beta\langle N \rangle$ (where $\langle N \rangle$ gives the mean number of scatterings needed to escape), then from random-walk arguments we expect $S_i(0) \propto \xi\beta\langle N \rangle^{\frac{1}{2}}$. Note that the effectively-thin results merge smoothly with the effectively-thick results when $(\gamma r)^{-1} = \Lambda$, and with the optically-thin results when $(\gamma r)^{-1} = 1$.

From the results of Table 11-3 we see that, with a given chromospheric structure, some collision dominated lines will respond strongly to the temperature rise, while others may not, depending on the values of ϵ , r , and a appropriate to them. For example, for the Ca II lines in the solar chromosphere we have (to order of magnitude only!): $a \sim 10^{-3}$, $r \sim 10^{-9}$, $\epsilon \sim 3 \times 10^{-4}$, and $\gamma \sim 10^6$; therefore $\Lambda \sim 10^4$, while $(\gamma r)^{-1} \sim 10^3$, so the lines are effectively thin. Furthermore $a(\gamma r)^{-1} \sim 1$, so $(S_{i,\text{max}}/\beta) \sim \epsilon(\gamma r a)^{-\frac{1}{2}} \sim$

11-4 Static Extended Atmospheres 367

0.3, and thus the coupling of the Ca II lines to the temperature rise is relatively inefficient. In contrast, for the Mg II resonance lines, r is about a factor of 10 smaller (because Mg is about 10 times more abundant than Ca), and the other parameters are about the same; in this case we obtain a much stronger coupling to the rise and much brighter emission, as observed. It should be noted that the arguments given about are meant only to be *qualitative*, for the depth-variation of the parameters is actually fairly complicated, and not well-represented everywhere by the values chosen; in particular, equation (11-60) provides a relatively poor fit to the actual run of $B_v(t)$. Detailed analyses of Ca II line-formation in stellar chromospheres have been performed using realistic atomic and atmospheric models (56; 58), and a physically plausible explanation of the Wilson-Bappu effect has begun to emerge (57).

11-4 Static Extended Atmospheres

As was described in §7-6, many stars have extended atmospheres whose thicknesses are comparable to the radius of the star. We shall suppose that, to a first approximation, these atmospheres are spherically symmetric. For the purposes of the present discussion we shall consider the stellar radius r_* to be that of the surface on which $\tau_v \approx \frac{1}{2}$. We imagine that this "photospheric core" is surrounded by an envelope of large size, within which unit optical depth in the most opaque spectral regions (i.e., line centers) is encountered at radii $R \gg r_*$. In reality, virtually all stars with very extended atmospheres also have large-scale velocity fields (usually overall atmospheric expansion) that strongly affect—indeed dominate—transfer in the lines, so that the assumption of a static atmosphere is physically less useful in an analysis of line-formation than it was for the continuum. Nevertheless, there are some extremely important effects of a fundamentally geometric origin that enter; it is worthwhile to examine these here, and to defer a discussion of velocity-field effects until Chapter 14.

As seen by an outside observer, the size of the emitting surface where $\tau_v = 1$ at the more opaque frequencies, in particular the cores of spectral lines, can be much larger than that of the continuum. Then the line has a larger effective emitting area, and if we assume LTE and suppose that the envelope is essentially isothermal, it is clear that the line will appear in emission relative to the continuum. This behavior contrasts with the result for an isothermal planar atmosphere where the line is neither in absorption or emission. In fact, the basic geometric effect just described is actually the primary mechanism that produces the extremely intense emission in very opaque spectral lines observed—e.g., in Wolf-Rayet spectra. The assumption

that the atmosphere is essentially isothermal implies a nonradiative source of energy input, for we have seen in §7-6 that in radiative equilibrium (in LTE), $J \sim B \sim r^{-2}$ in an extended atmosphere; thus the situation just described may be a bit extreme (though we have no strong physical reason to prefer radiative equilibrium—recall the solar corona!). Also, if the line source function has a scattering term, we expect $S_i(\tau)$ to decrease outward (in fact the drop is enhanced by extension effects; see below). However, it is clear that, for any given $S_i(\tau)$, the change in effective emitting area from line core to wing will always tend to increase the core emission, relative to the continuum, compared to the value it would have had in a planar atmosphere. Absorption lines will tend to weaken, and emission lines will tend to grow brighter, as atmospheric size increases.

A second effect of atmospheric extension is a systematic *increase of the escape probability* at a given (radial) optical depth. It is obvious from elementary geometric considerations that along all rays, except the single ray at $\mu = +1$, the optical path-length from the test point to the surface is *smaller* in a spherically symmetric atmosphere than in a plane-parallel semi-infinite atmosphere of identical properties (i.e., same run of physical variables along the radial direction in the two cases). Thus, in view of equation (11-22), $P_e(\tau)$ increases, and we expect $S_i(\tau)$ to decrease accordingly.

A third effect, which also increases the effective probability of escape, is the systematic *bias toward larger radii* in the scattering. Suppose that the scattering process is isotropic and that the material is homogeneous, so that the photon mean-free-path is the same in all directions, and that $l = 1$ defines a spherical volume around the test point. Then, from the basic geometry of the situation, it is easy to see that, in a spherical atmosphere, *more* photons end their flights at *larger* radii (hence closer to the surface); in contrast, in a planar atmosphere the probabilities that the photon ends its flight at a greater or smaller depth (by a given amount) are *equal*. If the material has an opacity that decreases strongly outward, the bias is enormously enhanced [see Table II and Fig. 2 of (374)]. This bias implies that the net chance of escape is enhanced even further.

The transfer equation for the two-level-atom line-formation problem [i.e., S_i given by an equation of the form of (11-56)] in spherical geometry is easily solved by the methods described in §7-6 [see equations (7-190) through (7-208) and related discussion]. Calculations for idealized models (374) similar to those employed earlier in this chapter provide illustrations of the concepts outlined above. We characterize the atmosphere by its outer radius R (in units of the core radius $r_c = 1$), a total line optical depth T_l , a continuum optical depth T_c , and opacities $\chi_i \propto r^{-2}$ and $\chi_c \propto r^{-2}$. We set $\varepsilon = \text{constant}$, and $B = 1$. Source functions for an envelope with no background continuum, surrounding an *empty* core (i.e., a nebula) are shown in Figure 11-12. The two

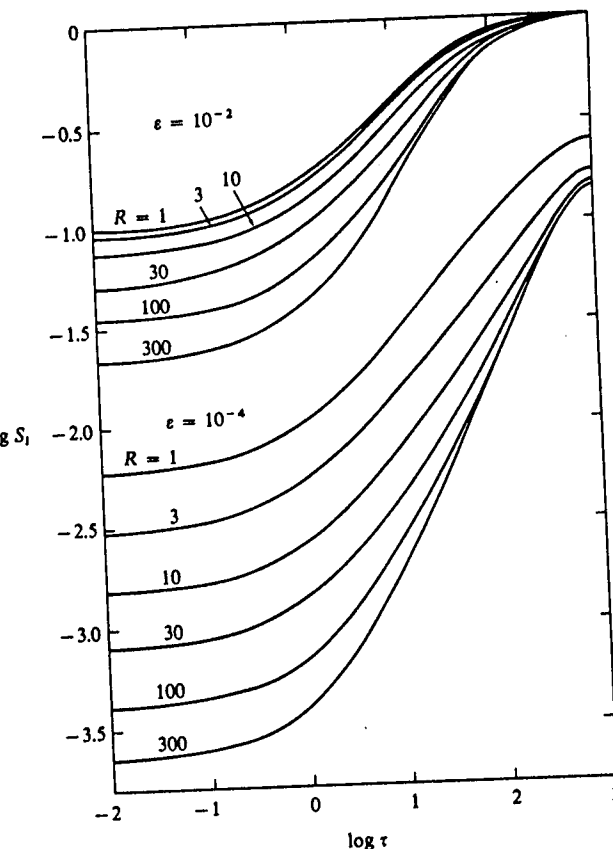


FIGURE 11-12
Line source functions in a spherical atmosphere of outer radius R (in units of $r_c = 1$), $B = 1$, $\varepsilon = \text{constant}$, $T_c = 0$, $T_l = 10^3$, and opacity $\chi_i \propto r^{-2}$. Curves are labeled with R , and results for two values of ε , corresponding to effectively thick and effectively thin media, are shown. From (374), by permission.

values of ε chosen yield effectively thick and effectively thin media. The major effects of increased photon escape in decreasing S_i are readily apparent. Note that, for the effectively thick medium, the thermalization depth ($\Lambda \approx 10^2$) is scarcely affected by sphericity. Emergent flux profiles for these source functions are shown in Figure 11-13. There we see that the central reversal, which is a prominent feature in the planar limit (note *log* scale), vanishes for very

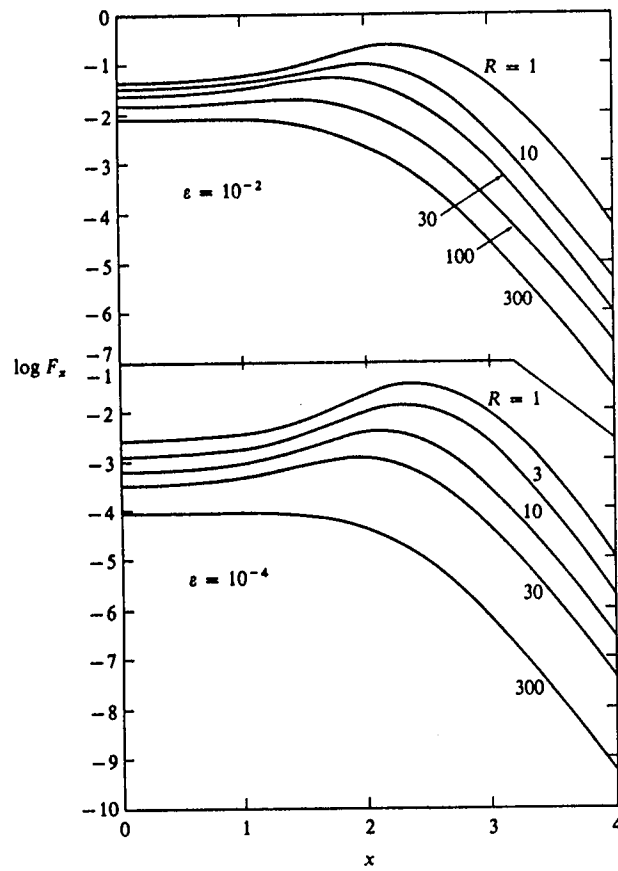


FIGURE 11-13
Emergent flux profiles from spherical atmospheres with same properties as used in Figure 11-12. From (374), by permission.

extended atmospheres; this is a manifestation of the greater effective emitting area in the line core. Analogous results for atmospheres with $T_c = 2$ and $\epsilon = 2 \times 10^{-3}$, and otherwise identical to those mentioned above, are shown in Figures 14-11 (source functions; note only curves with $v_{\max} = 0$) and 11-14 (line profiles). Again, the source functions are dramatically reduced by increased escapes, and the line profile transforms from a pure absorption line to an emission line with a central reversal (the reversal results only because S_l has decreased so much at $\tau = 1$; if S_l remained unchanged, the whole line would come into emission).

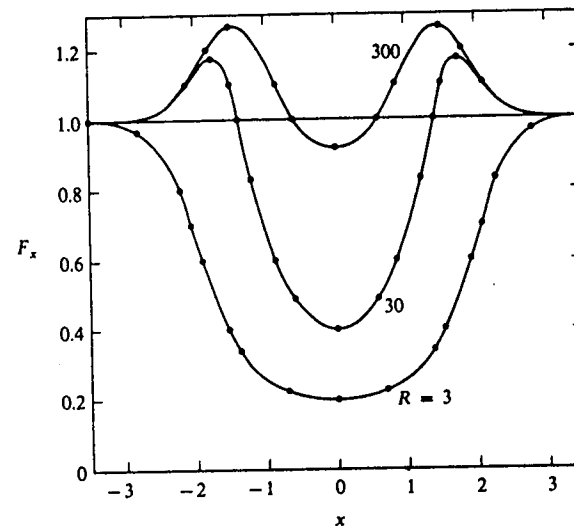


FIGURE 11-14
Emergent flux profiles from spherical atmospheres with $B = 1$, $\epsilon = 2 \times 10^{-3}$, $T_c = 2$, $T_l = 10^3$, and $\chi \propto r^{-2}$. The source functions in these atmospheres are shown in Figure 14-11.

11-5 Comments on LTE Diagnostics

From the developments presented in the preceding sections of this chapter we have obtained a very different, and physically a far more satisfying, picture of line-formation from that based on the assumption of LTE. The full multilevel problem must be solved before close quantitative agreement with observation can be obtained. It is, nevertheless, worthwhile to consolidate some of the changes in perspective inherent in the new conceptual framework fashioned above, by summarizing here a few of the important differences between the LTE and non-LTE methods of analysis, and by stressing the implications of these differences for the reliability of diagnoses of physical conditions in a stellar atmosphere. An extended discussion of many of these points can be found in (626).

In LTE line-formation theory, the source function is linked uniquely to the electron temperature T_e , and the line profile reflects the depth-variation of the Planck function, to within the limits of resolution set by photon diffusion over a single mean-free-path. In contrast, in the non-LTE theory $S_l(\tau)$ is no longer tied to $T_e(\tau)$; instead, it is fixed by the scattering term, which results from the interplay of the rates of photon escape, destruction,

and creation, by all mechanisms. Of these, only collisions couple the creation and destruction events to the local value of T_e . The other photon sources and sinks (which may far overshadow the collisional terms) couple to radiation fields in spectral regions outside of the line. Thus far, only continuum fields have been considered; but, as will be seen in Chapter 12, all lines in the entire transition array of the atom are, in principle, involved. To be sure, in the classical theory there was some flexibility implicit in the division of lines into "absorption" and "scattering" lines. But this division was ad hoc, and actually misleading, for we have seen that all line source functions have scattering terms, and that the important question is, "What are the sources and sinks that dominate in fixing the level of the scattering term?" The classical theory did not clearly recognize the photoionization category, and was essentially unprepared to cope with the mutual interaction of several lines.

One of the important implications of the above-mentioned changes in the theoretical structure is that, if S_i is no longer uniquely specified by the run of $T_e(\tau)$ (and, in fact, it may be totally unconnected with T_e), then it is clear that we cannot hope to infer $T_e(\tau)$ from the emergent intensity $I(\tau = 0, v)$. In particular, we have repeatedly found that $S_i(0)$, and hence the central intensity of the line, are almost completely unrelated to the "boundary temperature" T_0 , but are determined by transfer over an entire thermalization length, by photons fed into the line wings. Thus the literature containing estimates of stellar boundary temperatures, obtained from line-core intensities using an LTE theory, is little more than a collection of elaborate "maps" of nonexistent "territory."

Extending this conclusion, we notice that with an LTE theory, to explain the observed emission cores in the Ca II H - and K -lines we would have to propose a nonmonotone temperature distribution $T_e^*(z)$, which first decreases outward, then rises, then drops again. Not only would this be inconsistent with the distribution $T_e(z)$ inferred from (LTE!) methods using infrared and continuum data [which show a photospheric drop to a minimum plateau, followed by the chromospheric-coronal rise—cf. Figs. 7-31 and 7-32], but also the particular distribution inferred from the Ca II lines would not yield a fit to other lines (e.g., of Mg II) showing similar reversals. Worse, the use of such a temperature profile would produce emission reversals in all lines of sufficiently great strength, even those where none are observed (e.g., $H\alpha$). The entire problem vanishes when we discriminate between the collision-dominated and photoionization-dominated classes; and further, the new approach allows us to understand the varying degree of the effectiveness of the coupling of S_i to T_e for different collision-dominated lines. In short, the non-LTE analysis leads to an enormous improvement in our conceptualization of the physical situation.

One of the primary applications of LTE line-formation theory has been the estimation of stellar abundances. As we have seen, the depth-variation of

$S_i(\tau)$ is often markedly different from $B_v(T)$; thus the emergent intensity within the line (and hence its equivalent width) must differ from its LTE value. In a general way, the central depths of collision-dominated lines are increased by departures from LTE, and the equivalent width is increased (which implies that the abundance required to fit an observed width will decrease). For photoionization-dominated lines, non-LTE effects may either increase or decrease the linestrength; a useful summary of expected consequences of departures from LTE on abundances is given in (225).

Until recently the question "Do departures from LTE actually lead to significant errors in stellar abundance analyses?" remained open, and was the subject of vigorous and lengthy debate in the literature. As we shall see in §12-4, the question can now be answered in the affirmative in many important cases [see also (435)]. This is not to say that LTE abundance estimates are always in error; in many cases they are not. It is, however, apparent that it must be shown, and not merely assumed, that the application of LTE provides an adequate approximation to reality for any case in question.

Another parameter often inferred from curve-of-growth analyses is the characteristic "microturbulent" velocity in the atmosphere. Leaving aside the questions raised about whether a simple curve of growth adequately describes the complex problem of line-formation in a turbulent medium (discussed in §14-1), it is important to note that the diagnosis of this particular parameter is especially vulnerable to error from non-LTE effects. The position of the flat part of the curve of growth depends sensitively upon the way, and the distance over which, the line saturates to its thermal value, for these characteristics of the solution determine the depth and width of the line. For example, as remarked earlier in §11-2, even though coherent scattering may produce a line of the same depth as noncoherent scattering (with the same value of ϵ), the line will be wider in the latter case, and therefore the equivalent width larger. Calculations, for idealized model atmospheres and two-level atoms, have shown important effects of departures from LTE upon the flat part of the curve of growth (25), and recently (cf. §14-1) non-LTE theories that include stochastic velocity fields in the line transfer have been developed. Although there is little doubt that mass motions do exist in stellar atmospheres, the accuracy of the actual values assigned will remain in doubt until internally-consistent analytical methods are employed.

We now turn attention to the problem of attempting to match observed stellar spectra, using realistic multilevel model atoms and detailed model atmospheres, in a physically self-consistent solution of the full transfer and statistical equilibrium equations.

12

Non-LTE Line Transfer: The Multilevel Atom

The discussion presented in the previous chapter, based on the use of a highly simplified atomic model in idealized atmospheres, affords deep insight into much of the physics of spectrum line-formation. But to analyze real stellar spectra, it is now necessary (1) to consider much more realistic atomic models, having many levels (perhaps spread over a sequence of ionization stages), giving rise to a multiline transition array; and (2) to solve the combined transfer and statistical equilibrium equations for such atomic models, in fairly elaborate atmospheric models that attempt to describe the physical structure of the star with a high degree of realism. Throughout the discussion we shall assume that we are dealing with an "impurity" species (i.e., other than hydrogen) that has no significant influence on the structure of the atmosphere, and shall therefore regard the atmospheric model as given and *fixed*. It is obvious that with a larger number of levels, the number of transitions and interactions that are possible increases greatly, and both the physical and mathematical nature of the problem become more complex.

Moreover, it is essential to realize that this increased complexity is not merely one of having to treat larger systems of equations, but that there are extremely important new *physical* effects involved. In particular, we shall now find that *the radiation field in any one transition may affect that in every other transition in the atom*, and that in many cases these effects are of overwhelming importance. Furthermore, the way in which the effects manifest themselves is often very subtle, being the result of extremely complicated chains of interactions. This mutual interaction of line radiation fields (and source functions) is referred to as *interlocking*, and the successful treatment of interlocking effects poses the central obstacle to the solution of multilevel transfer problems.

The most straightforward approach to the multilevel problem proceeds from a rather direct extension of the techniques employed in the previous chapter for a two-level atom. Here one writes analytical expressions for the source function in each line in such a way as to isolate explicitly the radiation field in that line, and solves the corresponding transfer equation holding all other terms fixed. This is the *equivalent-two-level atom* approach, in which only one line at a time is considered in the solution of the transfer equation, and the interactions among lines are treated by *iteration*. In the method just described, one has tacitly assumed that the coupling between lines is fairly weak in some sense; but often this is not the case, and the equivalent-two-level-atom approach then becomes unsatisfactory. For example, the individual line components of *multiplets* usually have, as their initial and/or final states, closely-spaced levels that can interact physically, very strongly. In such situations, photons may *switch* from one line to another in the multiplet, and the radiation fields in the lines become strongly interlocked. More generally, in chains of transitions within a complicated transition array, conditions often arise under which photons are rather freely *converted* from one transition, with its corresponding spectral region, to another. In effect, the photon no longer belongs uniquely to a *specific line*, but, to a certain extent, belongs to the *ensemble of radiation fields of the entire set of transitions of the atom*. The profound importance of this point was recognized and emphasized by Jefferies (334, Chap. 8; 284, 177), who advanced the appealing picture that the photons should be considered to be interchangeable members of a *collective pool*. Viewed in this light, it is apparent that it is essential to treat all of the lines and their interactions *simultaneously*, to a high degree of consistency. This may be done quite directly in special cases (e.g., in multiplets with a common lower state). In the general case, strict consistency can be achieved by the *complete linearization method*; this scheme allows fully for all interlocking effects from the outset, and may be considered as the mathematical realization of Jefferies's physical conception of the collective photon pool.

12-1 The Equivalent-Two-Level-Atom Approach

FORMULATION

In our study of the two-level atom, we made use of the statistical equilibrium equations to eliminate analytically the population ratio appearing in the line source function, and thus to obtain an expression of the general form

$$S_l = \left(\int \phi_v J_v dv + \alpha \right) / (1 + \beta) \quad (12-1)$$

where α and β describe the possible ways of creating or destroying a photon. In writing equation (12-1), explicit use is made of the fact that for a *strict* two-level atom, there is only *one* line, hence only one radiation field of relevance. Indeed, we saw that if the atom also has a continuum, then the radiation fields in the two bound-free transitions appear in the terms α and β . Because the line is usually much more opaque than the continua, the latter will often be transparent at the depth of line-formation, and the continuum rates then will be *fixed* (though this is not always the case). If *other* levels and *other* lines are included, it is to be expected that the radiation fields in these transitions will also appear in the terms α and β , and, in addition, that these terms will vary (i.e., cannot be fixed *a priori*) in the region of line formation. Nevertheless, it is obvious that, however strong the coupling of a given line to other lines may be, the line must always at least respond to the collisional rate coupling the two levels in question, and to the continuum rates from these levels. This suggests that, as a computational strategy, one might attempt to write a mathematical expression for the source function in which the line-scattering, collisional interaction, and continuum radiative and collisional rates from the two levels forming the line appear as *direct rates*, while all other rates are grouped analytically into *net rates*; one hopes in this way to minimize the effect of interlocking at each stage of the calculation.

Consider a line formed between levels l and u . The rate equation for the lower level is

$$\begin{aligned} n_l & \left(B_{lu} \int \phi_v J_v dv + C_{lu} + \sum_{i < l} A_{li} Z_{li} + \sum_{i < j \neq u} C_{ij} Y_{ij} + R_{lk} + C_{lk} \right) \\ & - n_u \left(A_{ul} + B_{ul} \int \phi_v J_v dv + C_{ul} \right) \\ & = n_l^* (R_{kl} + C_{lk}) + \sum_{i < j \neq u} n_j A_{ji} Z_{ji} + \sum_{i < l} n_i C_{il} Y_{il} \quad (12-2) \end{aligned}$$

and for the upper level we have

$$\begin{aligned} n_u & \left(A_{ul} + B_{ul} \int \phi_v J_v dv + C_{ul} + \sum_{u > i \neq l} A_{ui} Z_{ui} + \sum_{u < j} C_{uj} Y_{uj} + R_{uk} + C_{uk} \right) \\ & - n_l \left(B_{lu} \int \phi_v J_v dv + C_{lu} \right) \\ & = n_u^* (R_{ku} + C_{uk}) + \sum_{u < j} n_j A_{ju} Z_{ju} + \sum_{u > i \neq l} n_i C_{iu} Y_{iu} \quad (12-3) \end{aligned}$$

In equations (12-2) and (12-3) we have used the *net radiative bracket* Z_{ji} defined by equation (5-58), the *net collisional bracket* Y_{ij} defined by equation (5-71), and the radiative ionization and recombination rates defined by equations (5-66) and (5-67); further n_i^* denotes the LTE population of level i , given by equation (5-14), at the *actual* value of the ion density.

If we solve equations (12-2) and (12-3) for the ratio $(n_l g_u / n_u g_l)$, substitute the result into the relation $S_{lu} = (2hv^3/c^2)[(n_l g_u / n_u g_l) - 1]^{-1}$, and make use of the Einstein relations among the transition probabilities, we find

$$S_{lu} = \left[\int \phi_v J_v dv + (\varepsilon' + \theta) B_v(T_e) \right] / (1 + \varepsilon' + \eta) \quad (12-4)$$

where ε' is defined as in equation (11-7), while

$$\eta \equiv [a_2 a_3 - (g_l / g_u) a_1 a_4] / [A_{ul}(a_2 + a_4)] \quad (12-5)$$

$$\text{and} \quad \theta \equiv [n_l^* a_1 a_4 (1 - e^{-hv/kT})] / [n_u^* A_{ul}(a_2 + a_4)] \quad (12-6)$$

where, in turn,

$$a_1 = R_{lk} + C_{lk} + \sum_{i < l} A_{li} Z_{li} + \sum_{i < j \neq u} C_{ij} Y_{ij} \quad (12-7)$$

$$a_2 = n_l^* (R_{kl} + C_{lk}) + \sum_{i < j \neq u} n_j A_{ji} Z_{ji} + \sum_{i < l} n_i C_{il} Y_{il} \quad (12-8)$$

$$a_3 = R_{uk} + C_{uk} + \sum_{u > i \neq l} A_{ui} Z_{ui} + \sum_{u < j} C_{uj} Y_{uj} \quad (12-9)$$

$$a_4 = n_u^* (R_{ku} + C_{uk}) + \sum_{u < j} n_j A_{ju} Z_{ju} + \sum_{u > i \neq l} n_i C_{iu} Y_{iu} \quad (12-10)$$

Exercise 12-1: Verify equations (12-4)–(12-10).

It is clear that the terms a_1 and a_2 represent, respectively, the loss rate from level l to all levels other than u , and the number of electrons fed into level l from all levels other than u ; a_3 and a_4 denote similar quantities for level u .

The resemblance of equation (12-4) to the two-level form is obvious. Note that the populations of *all other levels* appear in the terms a_2 and a_4 . This occurs because we have used only two of the entire set of rate equations, and hence can eliminate *only* n_l and n_u . It is possible, in principle, to obtain an expression for the source function S_{lu} that does not involve any of the occupation numbers *explicitly*; here the full set of rate equations $\mathcal{A}n = \mathcal{B}$ is manipulated to give analytical expressions for the quantities α and β , in equation (12-1), in terms of the cofactors of \mathcal{A} [see (333; 284, 187)]. However, the algebra in such a procedure quickly becomes hopelessly unmanageable; and, more important, it is not at all obvious that anything is gained, for the resulting source function then is *nonlinear* in the radiation fields of all other transitions. Moreover, these radiation fields depend upon the occupation numbers in the appropriate levels, hence S_{lu} will still depend *implicitly* upon the n_i 's, ($i \neq l, i \neq u$).

If we write χ_c for the continuum opacity and

$$\chi_{lu} = (B_{lu}h\nu/4\pi)[n_l - (g_l/g_u)n_u]$$

for the line opacity, then the transfer equation at each frequency in the line can be written as

$$\mu(dI_v/dz) = -(\chi_c + \chi_l\phi_v)I_v + \chi_cS_c + \chi_l\phi_vS_l \quad (12-11)$$

where S_c denotes the continuum source function (which is not necessarily the Planck function). Writing $d\tau_v = -(\chi_c + \chi_l\phi_v)dz$, and substituting for S_l from equation (12-4), equation (12-11) can be rewritten as

$$\mu(dI_v/d\tau_v) = I_v - a_v \int \phi_v J_v dv - b_v \quad (12-12)$$

which can be recast into a second-order form, and solved by the standard Feautrier or Rybicki methods described in Chapter 6. A calculation of this type is carried out for *each line* of the entire transition array considered. Note that to compute χ_l , and hence τ_v , a_v , and b_v in equation (12-12), it is necessary to have actual values for n_l and n_u ; as these quantities are known only approximately at any stage of the calculation, it is clear that an iteration procedure is required, in which successively more accurate values of the occupation numbers are employed. This iteration may be carried out simultaneously with the more basic iteration required to obtain estimates of the radiative rates in all lines.

In a calculation designed to simulate conditions in a real atmosphere, it is, in general, necessary to account for the variation in the ionization state of the particular atomic species under consideration (perhaps over a sequence of several different ionization stages). Although continua arising from excited states of "impurity" species will generally be transparent (compared to the dominant absorption and emission terms from H and He), so that the radiation field may be considered to be *fixed*, this situation will not usually be true for ground state continua, which normally will be opaque enough to determine their own radiation fields. Thus it is necessary to supplement the line transfer equations (12-12) with corresponding continuum equations, as described in the discussion of the formation of the Lyman continuum in §7-5 [see equations (7-127) through (7-131) and (7-135) through (7-144)]. The complete set of rate equations for a particular impurity species will be composed of as many equations as there are bound levels (over all stages of ionization taken into account), plus a final equation setting the sum of all occupation numbers equal to n_{atom} , the total number density of the species. For a given abundance of the element, relative to hydrogen, n_{atom} is a pre-specified function of depth. In overall form these equations are similar to the first M_{He} lines of the matrix displayed, in §5-4, between equations (5-91) and (5-92).

The iteration procedure required to obtain the solution (which consists of the run of the occupation numbers of all the levels with depth) is fairly straightforward in principle, though often complicated in practice. If one starts with an initial estimate of $n_i(z)$ for all atomic levels i , say from LTE relations, then provisional optical depth scales can be constructed. By regarding χ_c and η_v as known [via equations (7-1) and (7-2)], an estimate of the radiation field in each transition may be obtained by a *formal solution* of the transfer equation (i.e., S_l is regarded as given). One may use this estimate to compute continuum photoionization and recombination rates. A transfer equation of the form (12-12) for each line (and opaque continuum) is then solved in sequence, supposing, initially, that all the net brackets Z_{ji} and Y_{ij} appearing in equations (12-7) through (12-10), and their continuum analogues, may be set identically to zero. This sequence of calculations produces radiative rates R_{ij} in all lines and opaque continua. The rate equations $\mathcal{A}n = \mathcal{B}$ are then re-solved, at each depth, to obtain an improved estimate of all the occupation numbers n . All Z_{ji} 's and Y_{ij} 's, and hence η and θ for each line can now be evaluated via equations (12-5) through (12-10) because all of the required rates and level-populations are known. Equations (12-12) are then re-solved, using the new values for τ_v , η , and θ and one obtains, thereby, new estimates of J_{lu} and S_{lu} in every line (and continuum). The rate equations are again re-solved, and the process is iterated to convergence. Once a converged solution is obtained, all the line source functions are known, and line profiles may be calculated for each line.

As mentioned above, the practical implementation of a successful iteration procedure using the equivalent-two-level-atom formalism is often quite complicated, for the rate of convergence (or lack thereof!) may be strongly affected by technical details, such as the way the net rates are computed, source functions are evaluated, and many others. Careful discussions of these points can be found in (18, Chap. 4; 23, 27–63; 23, 113–132; 187), as well as in the references cited therein. A more fundamental difficulty with this overall approach is that the iteration procedure may fail to converge but, instead, stabilizes on a solution that is *inconsistent*; see the discussion in (18, §4.2) and (23, 27–63). This failure, which is not too common, and which can sometimes be overcome with special procedures, is, nevertheless, not surprising; as we shall see in the next section, there are many physical situations in which the radiation fields in different lines are very strongly interdependent, in contradiction to the basic assumption of the equivalent-two-level-atom approach. The inconsistency problem is overcome wholly by the complete-linearization method presented in §12.3.

APPLICATION

The equivalent-two-level-atom approach has been extensively applied to calculations of a wide variety of spectra, particularly for the solar atmosphere and for solar-type stars. For example, for the sun, analyses have been made of the Ca II *H*- and *K*-lines (400; 401; 569), O I and C II lines (168), the Mg I *b*-lines and Na I *D*-lines (21), and the spectrum of Fe I (22), using sophisticated multilevel atoms and elaborate atmospheric models. Very complete spectrum syntheses, using this general approach, of both continuum and line intensities have led to refined photospheric-chromospheric models (645; 646). Further, similar analyses have been made of the Ca II *H*- and *K*-lines in solar-type stars (56; 58).

Space does not permit a discussion of all of these results, and the reader should examine the references cited. It is, nevertheless, of interest to quote a few results (401) for the solar Ca II lines, which play a central role in studies of the chromosphere. The *H* and *K* lines arise from the transitions $4s^2S_{\frac{1}{2}} \rightarrow 4p^2P_{\frac{1}{2}, \frac{3}{2}}$ (see Figure 12-1); the two upper states are coupled by collisions, and may also decay to the metastable $3d^2D_{\frac{3}{2}, \frac{5}{2}}$ states in the infrared triplet $\lambda\lambda 8498, 8542, 8662$. As the next levels lie well above the $4p$ level (recall $kT \sim 0.5$ eV in the solar photosphere), the five levels mentioned above, plus the continuum, suffice to provide an accurate description of the physics of line-formation. A solution of the transfer and statistical equilibrium equations for this 5-level Ca⁺ atom yields source functions in all 5 lines; the frequency-independent *K*-line source function (obtained assuming complete redistribution) is shown in Figure 12-2, along with the Planck function

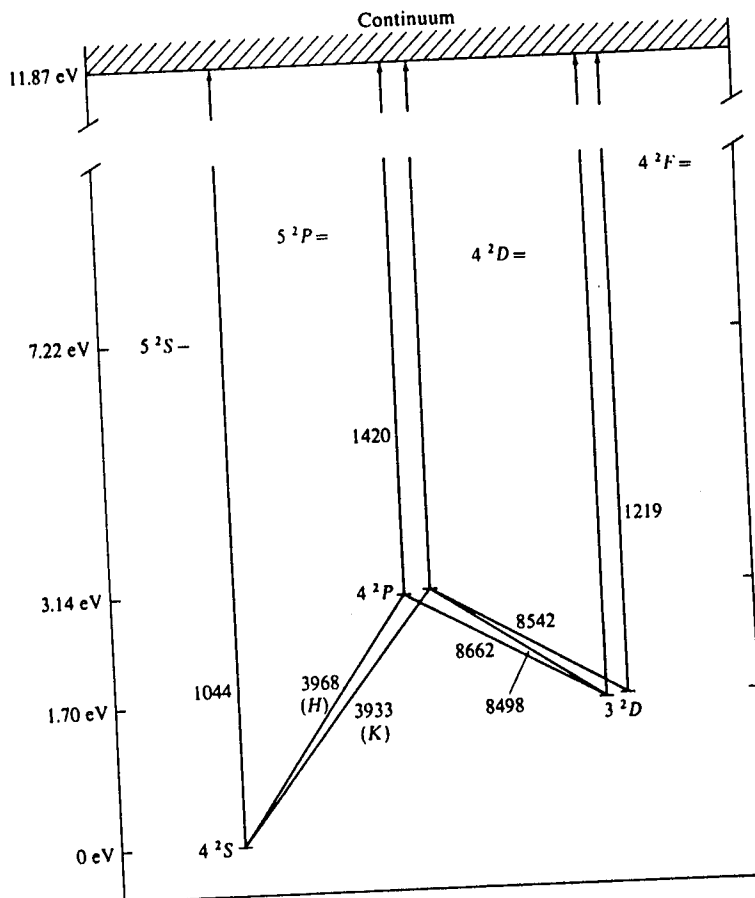


FIGURE 12-1
Energy-level diagram for lower states of Ca⁺. The five levels $4s^2S_{\frac{1}{2}}$, $4p^2P_{\frac{1}{2}, \frac{3}{2}}$, and $3d^2D_{\frac{3}{2}, \frac{5}{2}}$ suffice to describe the line-formation process for the Ca II *H* and *K* lines at $\lambda\lambda 3968$ and 3933 , and the infrared-triplet $\lambda\lambda 8498, 8542, 8662$. Note that the next levels lie fairly high in energy, and hence can be ignored, though interactions with the continuum are included. From (401), by permission. (Courtesy of the Publications of the Astronomical Society of the Pacific.)

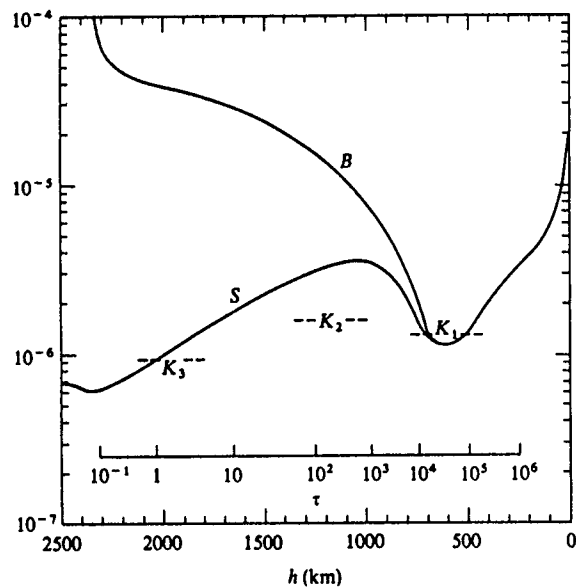


FIGURE 12-2
Ca II K-line source function S , and corresponding Planck-function B , in model solar atmosphere. Source function is in absolute units: $\text{ergs cm}^{-2} \text{ sec}^{-1} \text{ hz}^{-1} \text{ sr}^{-1}$. Optical depth scale is at line center and dashed lines indicate intensities at K_1 , K_2 , and K_3 (see Fig. 12-3). From (401), by permission. (Courtesy of the *Publications of the Astronomical Society of the Pacific*.)

corresponding to the adopted run of temperature $T_e(h)$. The emergent intensity profiles, at $\mu = 1$, for the H - and K -lines and the infrared triplet, are compared with observation in Figures 12-3 and 12-4, respectively. The agreement between theory and observation is quite satisfying. However, when the computed variation of the H - and K -line profiles from center to limb is compared with observation, significant disagreements are found; as we shall see in §13-4, these are removed when the partial coherency of the scattering process, and the resulting frequency-dependence of the source function, are taken into account. Further, the calculations shown in Figures 12-3 and 12-4 represent only the average quiet chromosphere. To match plage profiles (569), a different atmospheric model is required; and to match the *detailed* variation of the K -line profile, as observed from point to point on the disk, will require a full treatment of the three-dimensional fine-structure and the velocity fields in the chromosphere. Such calculations have not yet been undertaken in a completely satisfactory fashion, but are needed, both to diagnose details of chromospheric structure, and to answer the question "To what extent

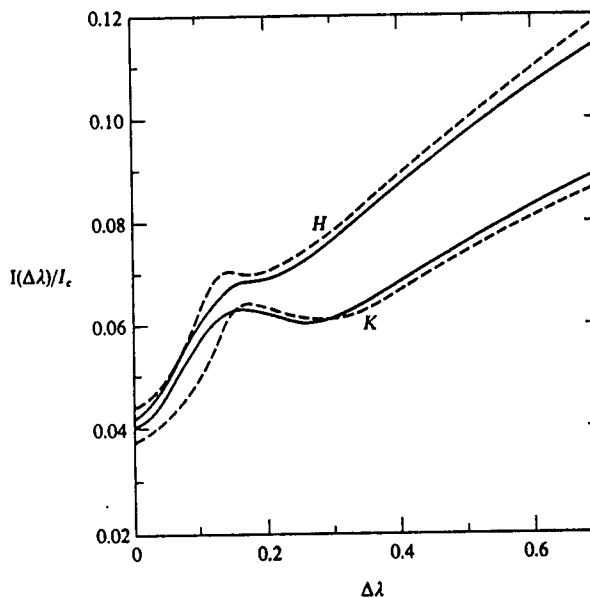


FIGURE 12-3
Computed H - and K -line profiles at $\mu = 1$ (dashed lines) compared with observed profiles (solid lines). From (401), by permission. (Courtesy of the *Publications of the Astronomical Society of the Pacific*.)

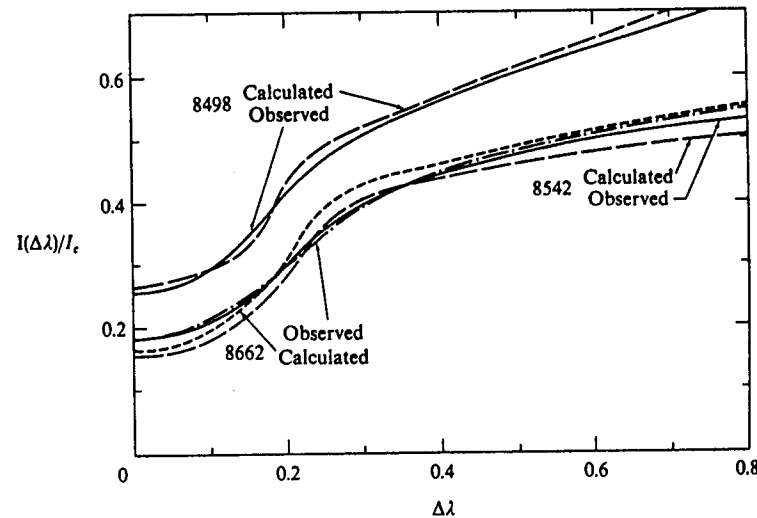


FIGURE 12-4
Computed Ca II infrared-triplet profiles at $\mu = 1$ compared with observed profiles. From (401), by permission. (Courtesy of the *Publications of the Astronomical Society of the Pacific*.)

(if any) is it possible to replace the complicated multidimensional structure of the chromosphere with a meaningful horizontally-averaged 'mean chromosphere'?"

12-2 Effects of Level Coupling: Source Function Equality in Multiplets

As was emphasized in the preceding section, the equivalent-two-level-atom approach works best when the coupling terms from two particular levels to all other levels are small, compared to those between the levels themselves and from these levels to the continuum. There are, however, many important physical situations for which this will *not* be the case, and it is important to understand the effects of strong coupling among several levels. These effects have important implications that affect both our perception of line-formation, and our choice of numerical methods used to obtain solutions of multilevel transfer problems. Most of the fundamental physical concepts were outlined by Jefferies (333; 334, Chap. 8), and much of the subsequent theoretical work [e.g. (567)] has been based on his ideas. Numerous instructive calculations, using idealized multilevel atomic models and parameterized model atmospheres, have been carried out; see, e.g., (54; 18, Chap. 4; 187; 213; 217; 218). Rather than attempt to summarize these diverse investigations here, we shall, instead, confine attention to two concrete examples, which illustrate the nature of interlocking effects in a particularly illuminating way.

First we shall consider, briefly, the case of three levels coupled together by two lines of a resonance series, and one subordinate line. The primary result of interest here is *photon degradation* from the higher resonance line into the lower resonance and subordinate lines; this phenomenon is related to fluorescence in nebulae and to the Rosseland cycles discussed in §5-5. Next, we shall devote the remainder of the section to the interlocking of lines within a multiplet; here *photon conversion* may occur as collisions shuffle electrons among the fine-structure levels of the spectroscopic terms involved. As a result, the source functions in the different lines become dependent upon one another, and in a certain limit become *equal* at each depth in the atmosphere. *Source-function equality* in multiplets is of great theoretical importance, for it implies that we may replace several lines within a multiplet by a single representative line, and thereby reduce greatly the amount of computation required. Further, source function equality, when it occurs, allows application of a non-LTE method of analysis of line-profile data, by means of which the physical properties of an atmosphere may be inferred directly with a minimum of theoretical interpolation. In keeping with the remainder of the book, in which theoretical prediction rather than analysis of observations has been emphasized, this analytical method will

not be discussed here, and the reader is encouraged to refer to the complete discussion by Jefferies (334, Chap. 9).

PHOTON DEGRADATION AND CONVERSION

Consider, first, a three-level atom with two resonance lines $1 \leftrightarrow 2$ and $1 \leftrightarrow 3$, and a subordinate line $2 \leftrightarrow 3$. As an example, in hydrogen we would have the $L\alpha$, $L\beta$, and $H\alpha$ lines; in fact, for expository convenience, the three lines will be referred to with these names, even though we may not be dealing with hydrogen. For the present purposes, interactions with the continuum will be ignored, and attention focussed entirely upon the lines. Generally, we can expect the ground-state population n_1 to be vastly larger than the upper-state populations n_2 and n_3 ; hence the resonance lines will be much more opaque, and will have much larger optical depths, at a given physical depth, than the subordinate lines. Suppose now that all three lines were somehow uncoupled, and were formed in distinct two-level atoms; each would then thermalize at a characteristic depth $\Lambda_{ij} \approx 1/\varepsilon_{ij}$, where ε_{ij} is the collisional destruction probability in transition $i \leftrightarrow j$. Because $h\nu_{23} \ll h\nu_{12}$ (or $h\nu_{13}$) we will generally find $\varepsilon_{23} \gg \varepsilon_{12}$ (or ε_{13}); hence the subordinate line will thermalize in a smaller number of optical depths, measured on its own scale, than the resonance lines.

But this will be overshadowed by the much greater opacity in the resonance lines, and the subordinate-line thermalization will occur at much greater geometric depth in the atmosphere. Put another way, the subordinate line is so much more transparent than the resonance lines, that photon-escapes (and hence departures of S from B) first occur in *this* transition, as one proceeds outward from great depth toward the surface of the atmosphere. There will thus be a certain range of depths over which the resonance lines, were they *not* coupled to the subordinate line, would by themselves be thermalized, but within which the subordinate line has become transparent enough to permit escapes. In this critical range, some of the electrons photoexcited by $L\beta$ from level 1 to level 3 will decay into $H\alpha$, and the $H\alpha$ photons will escape; there will thus be a systematic *degradation* of $L\beta$ photons into $H\alpha$ and $L\alpha$ photons, at a rate determined by the branching ratio $A_{32}/(A_{31} + A_{32})$. Note that the inverse process of conversion of $H\alpha$ photons into $L\beta$ is essentially ineffectual. If an $H\alpha$ photon is absorbed, leading to an excitation $2 \rightarrow 3$, *most* of the subsequent emissions from state 3 will be in the $3 \rightarrow 1$ transition; because, however, τ_{13} is so large and ε_{13} is so small, these photons are *trapped*, and merely scatter until a $3 \rightarrow 2$ transition is finally made, and the photon escapes. In this atmospheric region, $L\alpha$ will adjust in such a way as to remain almost in detailed balance (with its source function near to the Planck function), while $L\beta$ excitation is drained, and its source function is depressed.

Ignoring stimulated emissions, we can express "reduced" source functions as $(S_{21}/B_{21}) = (b_2/b_1)$, $(S_{31}/B_{31}) = (b_3/b_1)$, and $(S_{32}/B_{32}) = (b_3/b_2)$, where B_{ij} denotes the Planck function $B(v_{ij}, T)$, and $b_i \equiv n_i/n_i^*$. When $L\alpha$ adjusts to detailed balance, $b_2 = b_1$ (recall the discussion pertaining to the ground-state population of H in B-stars given in §7-5), and thus $(S_{32}/B_{32}) = (S_{31}/B_{31})$, so that the "reduced" $L\beta$ and $H\alpha$ source functions become equal below the point of $L\alpha$ thermalization. As we proceed to the outermost layers of the atmosphere, the $L\beta$ line becomes more and more transparent and, ultimately, the probability of direct escape exceeds the branching ratio into $H\alpha$, with its consequent escape; at this point the $L\beta$ and $H\alpha$ source functions become uncoupled.

Results from a calculation (218) for a three-level atom with the parameters $A_{31}/A_{32} = 10$, $\epsilon_{12} = \epsilon_{13} = 10^{-3}$, $\epsilon_{23} = 9 \times 10^{-2}$, $(\tau_{12}/\tau_{13}) = 6.2$, and $(\tau_{23}/\tau_{13}) = 1.6 \times 10^{-4}$ [$(S_{31}/B_{31})/(S_{32}/B_{32})$] are shown in Figure 12-5. There we see that $L\alpha$ thermalizes at $\tau_{13} \approx 2 \times 10^2$, which implies $\tau_{12} \approx 10^3$, as expected from ϵ_{12} . At $\tau_{13} \lesssim 10$, the probability of $L\beta$ escape is comparable to the probability of branching into $H\alpha$; therefore for $\tau_{13} < 10$ the "reduced" $L\beta$ and $H\alpha$ source functions diverge. But below this depth, they rapidly

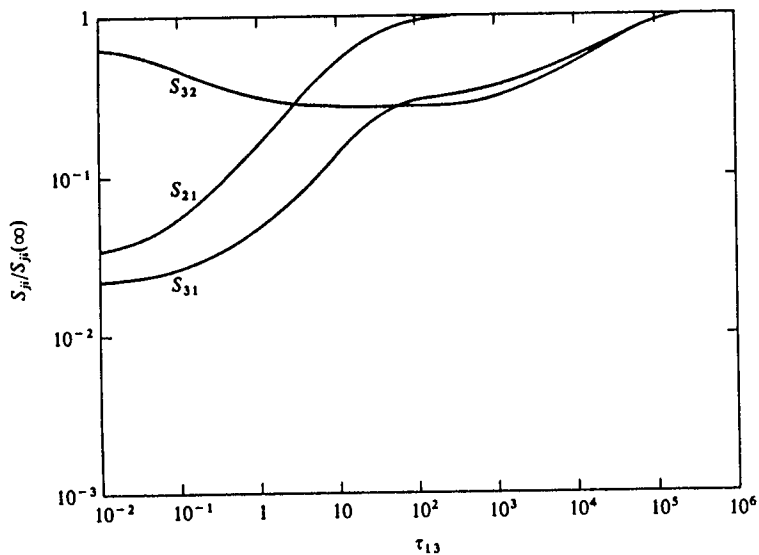


FIGURE 12-5
Source functions for 3-level atom in which both resonance lines, $(1 \leftrightarrow 3)$ and $(1 \leftrightarrow 2)$, and the subordinate line $(2 \leftrightarrow 3)$ are radiatively permitted. Abscissa: optical depth in the $1 \rightarrow 3$ line; ordinate: "reduced" source functions $[S_j(\tau)/S_j(\infty)]$; $S_j(\infty)$ is equal to the Planck function at the appropriate frequency. From (218), by permission.

12-2 Effects of Level Coupling: Source Function Equality in Multiplets

approach equality, at a value well below that which the $L\beta$ source function would have attained if degradation did not occur. Thermalization in $H\alpha$ (and, along with it, $L\beta$) occurs at about $\tau_{13} \approx 10^5$, which implies $\tau_{23} \sim 10$, as would be expected from ϵ_{23} . Further discussion and interpretation of the results may be found in the paper cited, but it is clear from what has been said here that there are major effects of interlocking on the source function variations in this problem. See also (18, §4.8).

Let us now turn to the case of a three-level atom consisting of a ground state, and two close-lying upper states. We assume that both radiative and collisional transitions can take place between states 1 and 2, and between 1 and 3, but that only collisional transitions occur between states 2 and 3. This model simulates the actual physical situation for a *resonance doublet*, where the upper states are separated by fine-structure splitting. For example, the sodium D-lines arise from transitions from the $3s\ ^2S_1$ ground state (state 1) to the upper states $3p\ ^2P_3$ and $3p\ ^2P_1$ (states 2 and 3).

Consider first the limit in which the $2 \leftrightarrow 3$ collision rate is zero (i.e., the *uncoupled* case). The transitions $1 \leftrightarrow 2$ and $1 \leftrightarrow 3$ can then take place without reference to one another, and the two lines are formed independently. Each line will have a source function that falls below the local Planck function near the surface, and equilibrates to the Planck function at *thermalization depths* given by

$$\Lambda_{12} \approx (A_{21} + C_{21})/C_{21} \quad (12-13a)$$

$$\text{and} \quad \Lambda_{13} \approx (A_{31} + C_{31})/C_{31} \quad (12-13b)$$

Here we have made the simplifying assumptions of Doppler profiles and an absence of strong gradients. In the limit considered here, the run through the atmosphere of the source functions for the two lines will, generally, be different, and at any given depth they will not usually have the same value.

On the other hand, suppose that collisions occur very rapidly between levels 2 and 3. In this case, excited electrons are shuffled from one level to the other; we then say that photons have been *converted* back and forth between the two lines. In the transfer problem the two upper states become effectively a single state, and in the extreme limit, the occupation numbers of the two upper states will be proportional to their statistical weights. The source functions for the two lines (which depend on the ratio $n_1 g_u / n_2 g_1$) then become equal at each point in the atmosphere. (Here we ignore the inconsequential differences that may arise because v_{12} is not exactly equal to v_{13}). In general, the actual situation will be intermediate between the two extremes described above, and we expect that the source functions will be equal only over a limited range in the atmosphere.

Proceeding outward from the deepest layers of the atmosphere, we will find that the source functions in the lines begin to drop below the Planck

function at depths smaller than their thermalization depths; this occurs (cf. §11-2) because the escape probability begins to exceed the destruction probability. But if the collision rates C_{23} and C_{32} are nonzero, there is now a finite chance that the photon will be switched from one line to another, rather than be destroyed or escape, and there is now a *conversion length* (333; 284, 177) over which the source functions in the two lines are still coupled together. The lines become uncoupled only when the escape probability exceeds both the destruction and the conversion probabilities—i.e., when

$$P_e(\tau_{12}) \gtrsim (C_{21} + C_{23})/(A_{21} + C_{21} + C_{23}) \quad (12-14a)$$

and $P_e(\tau_{13}) \gtrsim (C_{31} + C_{32})/(A_{31} + C_{31} + C_{32}) \quad (12-14b)$

From equations (12-14), we see that the two lines could thermalize independently over the entire range predicted by equations (12-13) only if, *everywhere* on that range, $C_{31} > C_{32}$ and $C_{21} > C_{23}$ (by a fair margin); if either of these conditions is violated, photon conversion plays an essential role. Again assuming Doppler profiles, we can estimate the optical depths from which photons in each line can retain their strict identity, and can emerge, without being either collisionally destroyed or converted, as

$$\Lambda_{12}^* \approx (A_{21} + C_{21} + C_{23})/(C_{21} + C_{23}) \quad (12-15a)$$

and $\Lambda_{13}^* \approx (A_{31} + C_{31} + C_{32})/(C_{31} + C_{32}) \quad (12-15b)$

in the $1 \leftrightarrow 2$ and $1 \leftrightarrow 3$ transitions respectively. Let z_{12}^* and z_{13}^* be the *geometric depths* (from the surface) corresponding to Λ_{12}^* and Λ_{13}^* . Then the two groups of photons may propagate independently only over a depth $z^* = \min(z_{12}^*, z_{13}^*)$.

From a mathematical point of view, whenever conversion is competitive with thermalization, the usefulness of the iteration procedure employed by the equivalent-two-level-atom approach becomes less clear. It then appears more attractive to consider the two (*or more*) lines, and their effects upon one another, *simultaneously*, and to develop a different computational technique.

OBSERVATIONAL INDICATIONS OF SOURCE FUNCTION EQUALITY

To motivate further the theoretical development, let us consider some of the observational evidence that source function equality in multiplets actually occurs. An excellent example is provided by an extensive set of precise observations of the sodium *D*-lines at various positions on the disk of the Sun (655). The emergent intensity at a specified frequency and

disk-position is given by

$$I_v(0, \mu) = \mu^{-1} \int_0^\infty [S_c(\tau_c) + \beta_v S_i(\tau_c)] \exp \left[-\mu^{-1} \int_0^{\tau_c} (1 + \beta_v) dt_c \right] d\tau_c \quad (12-16)$$

where τ_c is the continuum optical depth scale, and $\beta_v \equiv \chi_i \phi_v / \chi_c$. In the core of the line $\beta_v \gg 1$, so that, with good accuracy, we may write

$$I_v(0, \mu) = \mu^{-1} \int_0^\infty S_i(\tau) \exp(-\tau \phi_v / \mu) \phi_v d\tau \quad (12-17)$$

where τ is now the line optical depth scale. For the *D*-lines one has $(f_{13}/f_{12}) = 2$; thus we may write

$$I_{12}(0, \mu, v) = \int_0^\infty S_{12}(\tau_{12}) \exp(-\phi_v \tau_{12} / \mu) (\phi_v / \mu) d\tau_{12} \quad (12-18a)$$

and $I_{13}(0, \mu, v) = \int_0^\infty S_{13}(\tau_{12}) \exp(-2\phi_v \tau_{12} / \mu) (2\phi_v / \mu) d\tau_{12} \quad (12-18b)$

Thus clearly $I_{13}(0, \mu, v) = I_{12}(0, \frac{1}{2}\mu, v)$ if S_{12} and S_{13} have a common depth dependence. In essence, one may compensate for the higher opacity in one line by increasing the path length in the other. When this comparison is carried out, very good agreement between the cores of the two *D*-lines is found, as shown in Figures 12-6a through 12-6c. By way of contrast, Figure 12-6d shows the inverse comparison of $I_{13}(0, \frac{1}{2}\mu, v)$ with $I_{12}(0, \mu, v)$, and demonstrates the genuine significance of the agreement shown in the other figures. The disagreement in the wings arises from the increasingly large contributions from the continuum, which invalidate the assumptions required to write equation (12-17).

These striking observational results provide an impetus to examine in detail the conditions under which source function equality can occur (aside from the trivial case of LTE), and to develop methods well suited to handle the transfer problem for multiplets. The strong agreement shown in Figure 12-6 is so impressive that, in some of the early analyses (655; 656), it was concluded that there must be *strict* source function equality in the two lines all the way to the surface. To obtain such equality, one would have to impose the exacting requirement that $C_{23} \gg A_{21}$ and $C_{32} \gg A_{31}$; these conditions cannot actually be met by the collisional rates for the *D*-lines in the solar atmosphere, and an apparent contradiction arises. Subsequent work (16; 51) has shown, however, that the requirements stated above are far too stringent, and that one needs to have only $(C_{32}/A_{31}) > (C_{31}/A_{31})$ and $(C_{23}/A_{21}) > (C_{21}/A_{21})$ (conditions that are met for the solar *D*-lines) to obtain a very near (though not *exact*) equality of the source functions. These conditions are sufficient to produce profiles that look identical to within the accuracy of the observations.

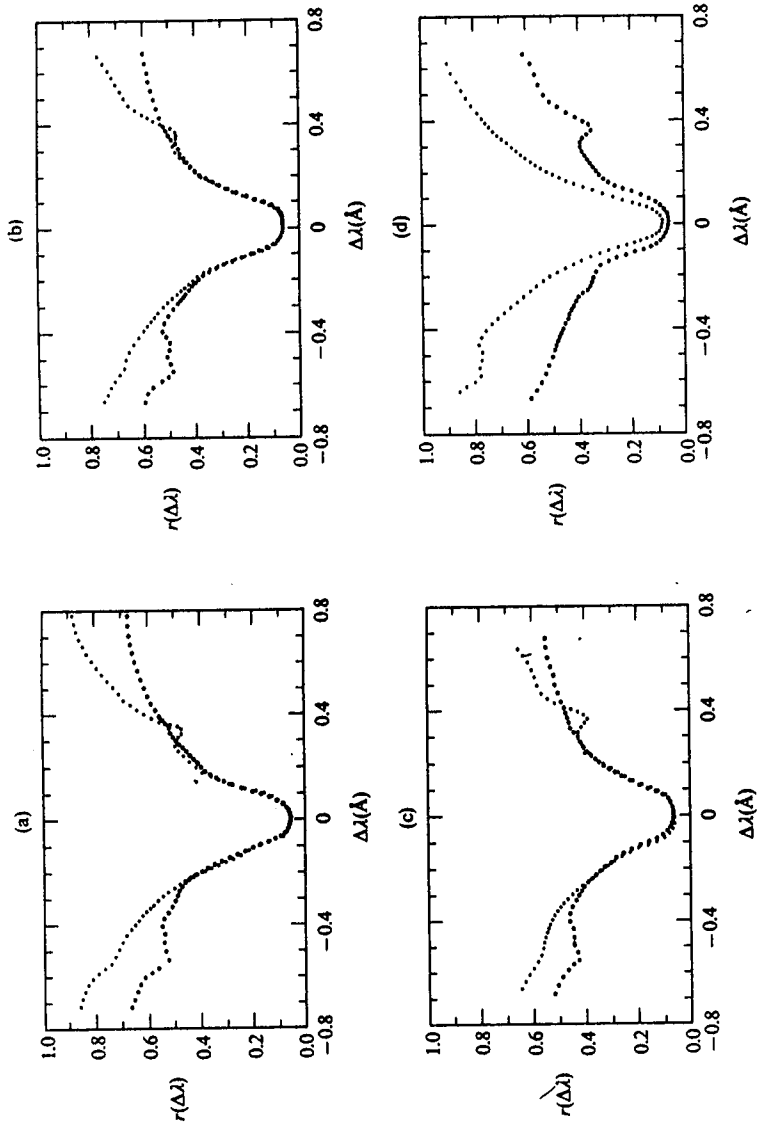


FIGURE 12-6
Comparison of $I_{12}(0, \frac{1}{2}\mu, v)$ with $I_{13}(0, \frac{1}{2}\mu, v)$ for solar sodium D-lines: (a) for $\mu = 0.6$; (b) for $\mu = 1.0$; (c) for $\mu = 0.6$; (d) Inverse comparison of $I_{12}(0, \frac{1}{2}\mu, v)$ with $I_{13}(0, \frac{1}{2}\mu, v)$ for $I_{12}(0, \frac{1}{2}\mu, v) \gg I_{13}(0, \frac{1}{2}\mu, v)$ with $I_{12}(0, \frac{1}{2}\mu, v) \gg I_{13}(0, \frac{1}{2}\mu, v)$. From (655), by permission.

SOLUTION OF THE TRANSFER EQUATION IN MULTIPLETS

Let us now consider how the coupled transfer problems for lines in a multiplet, arising from a single lower level to two (or more) upper levels that interact via collisions, are formulated and solved. For simplicity, stimulated emissions and coupling to the continuum will be neglected, and the differences in line frequencies ignored; these may, of course, be taken into account, but the algebra becomes much more complicated without a compensating enhancement of the physical content. The source function in the $(1 \rightarrow j)$ transition is

$$S_{1j} = (2hv^3/c^2)(g_1 n_j / g_j n_1) \quad (12-19)$$

The required population ratios are obtained from rate equations; for the case of only two upper levels these are:

$$n_2(A_{21} + C_{21} + C_{23}) = n_1(B_{12}J_{12} + C_{12}) + n_3C_{32} \quad (12-20a)$$

$$\text{and} \quad n_3(A_{31} + C_{31} + C_{32}) = n_1(B_{13}J_{13} + C_{13}) + n_2C_{23} \quad (12-20b)$$

where

$$J_{1j}(\tau) \equiv \int_{-\infty}^{\infty} J_{1j}(\tau, v)\phi_j(\tau, v) dv = \frac{1}{2} \int_{-\infty}^{\infty} dv \phi_j(\tau, v) \int_{-1}^1 d\mu I_{1j}(\tau, \mu, v) \quad (12-21)$$

Making use of the Einstein relations, and detailed-balancing relations of the form $C_{ij} = (n_j/n_i)^*C_{ji}$, and defining $\varepsilon_{12} \equiv C_{21}/A_{21}$, $\eta_{12} \equiv C_{23}/A_{21}$, $\varepsilon_{13} \equiv C_{31}/A_{31}$, and $\eta_{13} \equiv C_{32}/A_{31}$, we may rewrite equations (12-20), in terms of source functions of the form of (12-19), as

$$S_{12} = (J_{12} + \varepsilon_{12}B_v + \eta_{12}S_{13})/(1 + \varepsilon_{12} + \eta_{12}) \quad (12-22a)$$

$$\text{and} \quad S_{13} = (J_{13} + \varepsilon_{13}B_v + \eta_{13}S_{12})/(1 + \varepsilon_{13} + \eta_{13}) \quad (12-22b)$$

These expressions display transparently the *linear dependence* between S_{12} and S_{13} . We see that if $\eta_{12} = \eta_{13} \equiv 0$, the source functions are *uncoupled*. But if either $\eta_{12} \gg 1$ or $\eta_{13} \gg 1$, then $S_{12} \rightarrow S_{13}$. We see further, that even if the strong inequalities just mentioned are not satisfied, merely having $\eta_{1j} \gg \varepsilon_{1j}$ and $\eta_{1j}S_{1k} \gg \varepsilon_{1j}B_v$ will imply a near-equality of S_{12} and S_{13} , for then the physical source-sink terms in each source function will be dominated by the *other* line. The η_{1j} terms are thus expected to influence the solution in a way reminiscent of the collisional versus photoionization domination found in the two-level case (i.e., the lines in a multiplet may be "conversion-dominated").

In view of the linear dependence discussed above, it is evident that a simultaneous solution for both source functions is mandatory. Let us

consider a single ground state and an arbitrary number of upper levels. Equations (12-22) can be replaced by the general form

$$S_{1j} = \alpha J_{1j} + \sum_k \beta_{jk} S_{1k} + \gamma_j \quad (12-23)$$

where the sum extends over all upper levels. This system can be solved (at each depth-point in the medium) to obtain an expression of the form

$$S_{1j}(\tau) = \sum_k a_{jk}(\tau) J_{1k}(\tau) + b_j(\tau) \quad (12-24)$$

Exercise 12-2: Write explicit analytical expressions, of the form of equation (12-24), for the case of only two upper levels, starting from equations (12-22).

To write the transfer equation we now adopt the optical depth τ_{1i} in some particular line ($1 \rightarrow i$) as standard, and write $\gamma_j \equiv (d\tau_{1i}/d\tau_{1j}) = (f_{1j}/f_{1i})$. Then for each line ($1 \rightarrow j$) we have

$$\mu [dI_{1j}(\tau, \mu, v)/d\tau] = \gamma_j \phi_j(\tau, v) [I_{1j}(\tau, \mu, v) - S_{1j}(\tau)] \quad (12-25)$$

We introduce depth, angle, and frequency discretizations $\{\tau_d\}$, $\{\mu_m\}$, and $\{v_n\}$, and appropriate quadrature sums required to perform the integrations indicated in equation (12-21). Then defining

$$u_{j, dm} \equiv u_{1j}(\tau_d, \mu_m, v_n) = \frac{1}{2} [I_{1j}(\tau_d, +\mu_m, v_n) + I_{1j}(\tau_d, -\mu_m, v_n)] \quad (12-26)$$

and rewriting equation (12-21) as

$$J_{j, d} \equiv J_{1j}(\tau_d) = \sum_n \sum_m w_{mn} \phi_j(\tau_d, v_n) u_{j, dm} \quad (12-27)$$

the transfer equation can be written in the discrete form

$$\mu_m^2 (d^2 u_{j, dm}/d\tau^2) = (\gamma_{j, d} \phi_{j, dn})^2 \left(u_{j, dm} - \sum_{k=2}^{L+1} a_{jk, d} J_{j, d} - b_{j, d} \right) \quad (12-28)$$

Here $\phi_{j, dn} \equiv \phi_j(\tau_d, v_n)$, $a_{jk, d} \equiv a_{jk}(\tau_d)$, $b_{j, d} \equiv b_j(\tau_d)$,

and $\gamma_{j, d} \equiv \gamma_j(\tau_d)$

the sum extends over all L lines (or upper levels) considered. An equation of the form of (12-28) can be written for each line.

To solve the system we may use the Rybicki method. Define

$$u_{j, mn} \equiv (u_{j, 1mn}, \dots, u_{j, dm}, \dots, u_{j, Dmn}) \quad (12-29)$$

and $J_j \equiv (J_{j, 1}, \dots, J_{j, d}, \dots, J_{j, D})^T$ (12-30)

which describe the depth-variations of these quantities on the range $\tau_1 \leq \tau \leq \tau_D$. Then the system (12-28) can be written in the general form

$$T_{j, mn} u_{j, mn} + \sum_{k=2}^{L+1} U_{k, mn} J_k = K_{j, mn} \quad (12-31)$$

for each $(j = 2, \dots, L + 1)$, $(m = 1, \dots, M)$, $(n = 1, \dots, N)$. Here T is a $(D \times D)$ tridiagonal matrix, the U 's are $(D \times D)$ diagonal matrices, and K is a vector of dimension D . These systems are solved in succession to yield, in effect,

$$u_{j, mn} = \sum_{k=2}^{L+1} C_{jk, mn} J_k + D_{j, mn} \quad (12-32)$$

where C is a full $(D \times D)$ matrix. Equations (12-32) are substituted into the matrix representations of equation (12-27), namely $J_j = \sum_{mn} W_{j, mn} u_{j, mn}$, to generate a final system of the form

$$\sum_{k=2}^{L+1} P_{jk} J_k = Q_j, \quad (j = 2, \dots, L + 1) \quad (12-33)$$

Here each P_{jk} is a $(D \times D)$ matrix, so the whole system is of order $LD \times LD$. The system is then solved by standard numerical methods, and yields the full depth-variation in all lines simultaneously. When stimulated emission terms are included, the system becomes nonlinear and requires an iterative solution. A linearization method for the problem is described in (23, 1); we shall not discuss this particular procedure, but instead will describe, in §12-3, a more general method that handles this problem and many others from the outset.

The sodium D -lines have been studied (51), using schematic atomic and atmospheric models, with an integral-equation method essentially equivalent to the system described above. For these particular lines the following relations among atomic parameters exist: $g_1 = 2$, $g_2 = 2$, $g_3 = 4$, $A_{31} = A_{21}$, $B_{13} = 2B_{12}$, $C_{21} = C_{31}$; hence $\varepsilon_{12} = \varepsilon_{13}$ and $\eta_{12} = 2\eta_{13}$. Adopt the $1 \leftrightarrow 3$ transition as standard so that $\gamma_2 = \frac{1}{2}$ and $\gamma_3 = 1$. Solutions were obtained for a range of typical values of the parameters ε_{13} and η_{13} , and depth-variations of the Planck function. Results for cases with $B_v = 1$, $\varepsilon = 10^{-4}$, and $\eta = \eta_{13} = 0, 10^{-4}, 10^{-3}, 10^{-2}, 10^{-1}$, and 1, are shown in Figure 12-7. We see that, while η_{13} would have to be larger than 1 to guarantee strict source function equality to the very surface, much smaller values of η_{13} yield equality for $\tau \gtrsim 1$, which is the significant range for determining the emergent intensity. The emergent specific intensity for $\mu = 1.0, 0.8$, and 0.6 is shown in Figure 12-8. Clearly the profiles agree very closely when $\eta = 10^{-3}$, and are indistinguishable when $\eta = 10^{-2}$. These calculations show that, for all practical purposes, source function equality can occur for $\eta \ll 1$; indeed this result is not surprising, for we would, in fact, expect

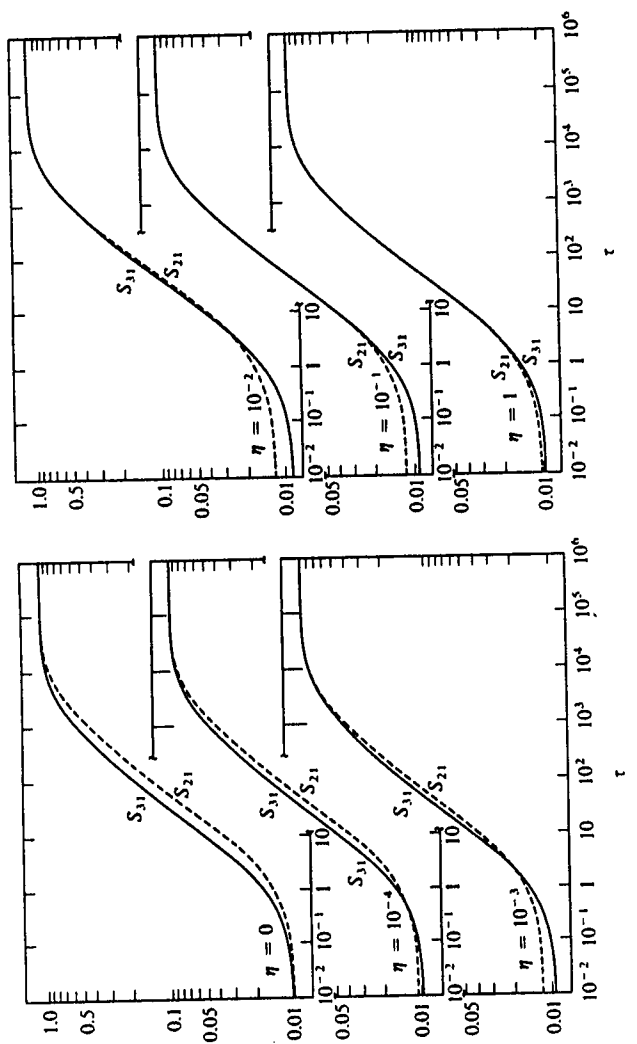


FIGURE 12-7
Source functions for an idealized sodium D-line multiplet in a semi-finite atmosphere, assuming $B_v = 1$, $\varepsilon = 10^{-4}$ and various values of $\eta = \eta_{13}$. From (51), by permission.

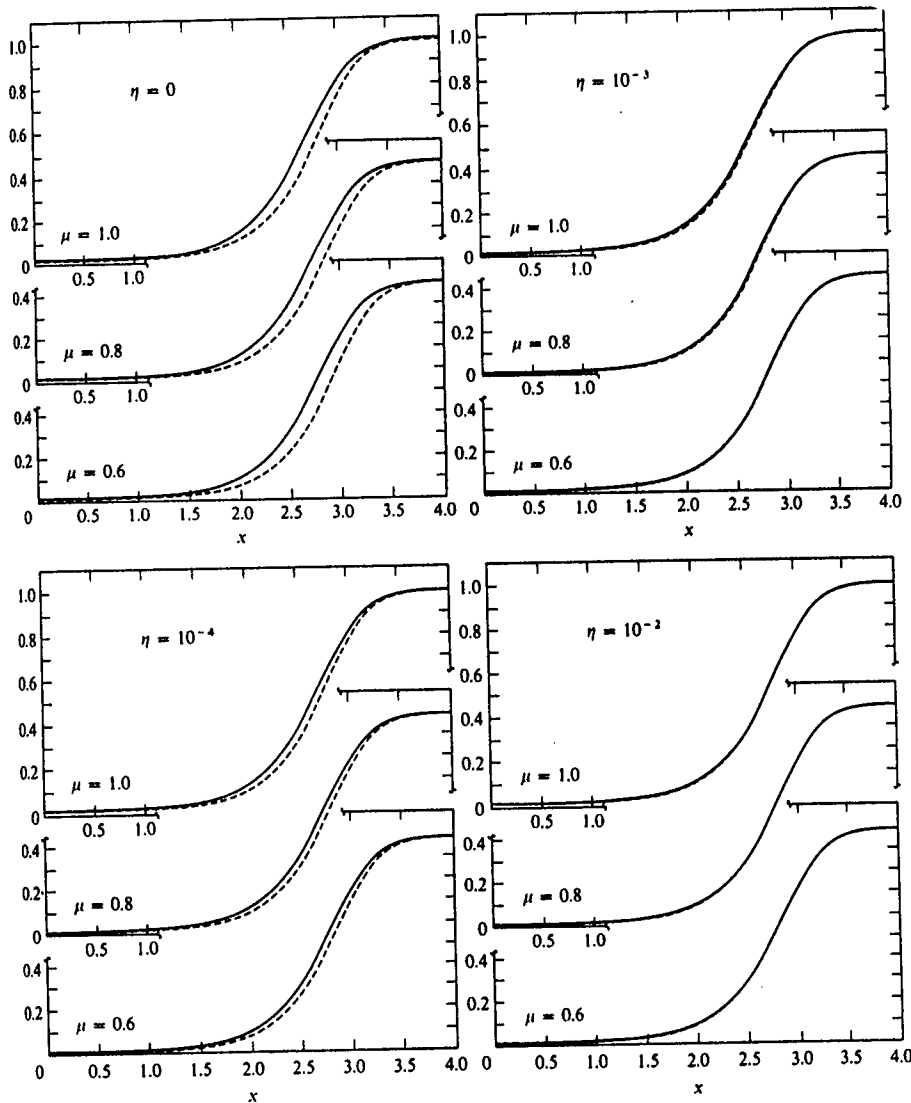


FIGURE 12-8
Line profiles comparing $I_{12}(0, \frac{1}{2}\mu, v)$ with $I_{13}(0, \mu, v)$ for various values of η , at $\mu = 1, 0.8$, and 0.6 . Solid curves give I_{13} , dashed curves give I_{12} . A scissa: displacement from line center in units of Doppler widths. From (51), by permission.

conversion to dominate individual line-thermalization as soon as $\eta \gg \epsilon$. The effects of a schematic temperature gradient were also studied, and it was found that, when $B_v(\tau)$ increases inward, the value of η required for source function equality decreases (compared to the $B_v \equiv 1$ case), and increases when $B_v(\tau)$ decreases inward. These results, however, may depend upon the specific forms chosen for $B_v(\tau)$, and may not be general.

12-3 The Complete Linearization Method

In the light of the discussion presented thus far in this chapter, it can be appreciated that the effects of interlocking in the multilevel line-formation problem are important, complex, and lead to systems of equations that may be ill-conditioned. Neither of the methods discussed thus far is entirely satisfactory for multilevel problems. The equivalent-two-level-atom formulation is ill-posed when there is strong coupling among lines. The method developed to treat multiplets is too specialized. What is needed is a method that is general, flexible, and computationally robust, and that handles the physical complexities of the problem. These requirements are met by the *complete linearization method* (42). In this method, the full set of rate equations is incorporated into the transfer equation, from the outset, by linearizing in terms of all occupation numbers and their dependences upon the radiation field. The rate equations themselves constitute the physical prescription of how the photons interact with the material, are created, destroyed, converted, degraded, and interlock within the collective photon pool envisioned by Jefferies. The transfer equations determine how this information is propagated from one depth to another. By means of the linearization procedure, a set of equations is developed that describes fully consistently (to first order) the response of the material, at every point in the atmosphere, to the radiation field at any frequency and any depth-point and, reciprocally, the response of the radiation field at all frequencies and all points in the medium to a change in material properties at any point. When this system is solved (iteratively), one has a simultaneous solution of the full set of rate equations and transfer equations that reflects both the global nature of the transfer problem (inherently large destruction/conversion lengths interplaying with an open boundary surface) and the intricate infrastructure of the statistical equilibrium equations. In practice, this method has provided a means of treating extremely complex model atoms with a very high degree of realism.

We shall examine here the statistical equilibrium problem for a multilevel "impurity" atom that has no effect upon the structure of the atmosphere. We regard the model atmosphere as given—i.e., the temperature (T), electron density (n_e), mass density (ρ), and the total number density of the species under consideration (n_{atom}) are all specified, fixed, functions of depth. The atom is assumed to have L discrete levels, distributed, perhaps, over several

ionization stages. The rate equations are formulated to describe all interactions among all levels, and to fix the total number density at the specified value n_{atom} . These equations will be of the general form of the first M_{He} lines of the matrix displayed in §5-4, supplemented by an equation of the form $\sum_{(l, J)} n_{lj} = n_{\text{atom}}$. For ease of exposition we make the simplifying assumption that, at any chosen frequency v_n , there is only one transition (say $l \leftrightarrow u$) of the atom that can interact (bound-bound or bound-free) with the radiation field, and that all overlapping sources of opacity and emission are fixed.

The transfer equation to be solved at each frequency v is

$$\partial^2(f_v J_v)/\partial \tau_v^2 = J_v - (\eta_v/\chi_v) \quad (12-34)$$

From equations (7-1) and (7-2) we can write the opacity and emissivity in a bound-bound transition as

$$\chi_v = \alpha_{lu}(v)[n_l - (g_l/g_u)n_u] + X_v \quad (12-35a)$$

$$\eta_v = (2hv^3/c^2)\alpha_{lu}(v)(g_l/g_u)n_u + E_v \quad (12-35b)$$

and that in a bound-free transition as

$$\chi_v = \alpha_{lu}(v)[n_l - n_u(n_l/n_u)*e^{-hv/kT}] + X_v \quad (12-36a)$$

$$\eta_v = (2hv^3/c^2)\alpha_{lu}(v)n_u(n_l/n_u)*e^{-hv/kT} + E_v \quad (12-36b)$$

where X_v and E_v are fixed. To unify the notation, write

$$\chi_v = \alpha_{lu}(v)[n_l - G_{lu}(v)n_u] + X_v \quad (12-37a)$$

$$\eta_v = (2hv^3/c^2)\alpha_{lu}(v)G_{lu}(v)n_u + E_v \quad (12-37b)$$

where $G_{lu}(v) \equiv (g_l/g_u)$ for bound-bound transitions, and $G_{lu}(v) \equiv n_e \Phi_l(T) \exp(-hv/kT)$ for bound-free transitions; here $\Phi_l(T)$ is the Saha-Boltzmann factor for level l [cf. equation (5-14)]. The system is discretized in depth $\{m_d\}$, ($d = 1, \dots, D$), and frequency $\{v_k\}$, ($k = 1, \dots, K$). We then can write a transfer equation of the form of equation (7-37) at each frequency v_k ; these equations are linearized to obtain an equation of the form of (7-39), where now $\delta\chi_{dk}$ and $\delta\eta_{dk}$ can be expressed simply as

$$\delta\chi_{dk} = \alpha_{lu}(v_k)[\delta n_{l,d} - G_{lu}(v_k) \delta n_{u,d}] \quad (12-38a)$$

$$\delta\eta_{dk} = (2hv_k^3/c^2)\alpha_{lu}(v_k)G_{lu}(v_k) \delta n_{u,d} \quad (12-38b)$$

The δn 's can be expressed in terms of changes in the radiation field only, as T and n_e are assumed fixed, and from equation (5-102) or (7-157) we can write

$$\delta n_d = \sum_{k=1}^K \left(\frac{\partial n}{\partial J_k} \right)_d \delta J_{dk} \quad (12-39)$$

where analytical expressions for $(\partial n / \partial J_d)$ are given by equation (5-108). By means of equations (12-38) and (12-39), it is now easy to eliminate all the δn 's in the linearized transfer equation analytically, in terms of the δJ 's only (33), and to obtain equations in the standard Feautrier form

$$-A_d \delta J_{d-1} + B_d \delta J_d - C_d \delta J_{d+1} = L_d \quad (12-40)$$

where

$$\delta J_d \equiv (\delta J_{d1}, \dots, \delta J_{dk}, \dots, \delta J_{dK})^T \quad (12-41)$$

and $A_1 = C_D \equiv 0$.

Exercise 12-3: Write explicit expressions for the elements of the matrices A_d , B_d , and C_d , and the vector L_d in equation (12-40).

In the formulation of the linearization procedure described in §7-5, both the δJ 's and δn 's appeared explicitly. By eliminating the δn 's the system size has been reduced from $[(K + L) \times (K + L)]$ to $(K \times K)$, which saves computer storage; but now A and C are full, whereas in the earlier formulation [cf. equation (7-159)] both A and C were diagonal (omitting the constraint of hydrostatic equilibrium which is not relevant in the present context). All of the operations in the elimination scheme given by equations (6-40) and (6-41) now involve full matrices, and the computing time therefore increases; the overall scaling is $T = c DK^3$, compared to the older scaling $T' = c'D(K + L)^3$, but c is much larger than c' .

The solution of equations (12-40) is carried out iteratively, as described below. The great power of the method is that equations (12-40) account for the full depth-to-depth and frequency-to-frequency coupling in the problem. That is, the effect of δJ_{dk} at (τ_d, v_k) upon $J_{d'k'}$ at all other $(\tau_{d'}, v_{k'})$ is given consistently, and thus photon propagation within the collective pool is taken fully into account.

In actual application of the method, we must now consider how to obtain a starting solution, and how to treat a large number of lines, as required by a realistic model atom. These questions are related, and the latter is of particular importance. For example, suppose the model atom has, say, 20 levels. On combinatorial grounds there could be of the order of 200 transitions; if we require, say, 10 frequencies per line profile, the problem becomes unmanageable. But of course spectroscopic selection rules severely limit the number of transitions that are actually possible in the spectrum, and among 20 levels one would typically have about 30 permitted lines. Of these, only a particular subset will directly influence those levels of primary interest in the treatment of definite limited set of lines in the spectrum, and usually it is possible to divide the transition array into a set of "primary" lines for which a strictly self-consistent treatment is necessary and a set of "secondary" lines for which a less precise treatment is adequate. This division is exploited in the initialization procedure.

To initialize the problem, the model atmosphere is used to determine background opacities and emissivities, and the radiation field is computed, assuming LTE populations for the atom under study. This radiation field is used to calculate photoionization rates, and the statistical equilibrium equations are solved assuming radiative detailed balance in the lines, but not in the continua; in this way one obtains the correct asymptotic solution at depth. It is then possible to do an equivalent-two-level-atom solution to find J_{lu} in each line.

The resulting J 's allow the radiative rates in the lines to be computed, and the complete statistical equilibrium equations can then be solved to obtain improved level-populations. This process may be iterated, and may be extended to include the analogue of the equivalent-two-level-atom solution for the opaque continua as described in §7-5 [cf. equations (7-135) through (7-144)]. The process outlined here could, in principle, be iterated to consistency, and one would then have the method of §12-1; however, in the present context, only one or two iterations are performed, and the results are adopted as initial estimates of the n 's, J 's, and Eddington factors required to start the linearization procedure. At this point, and henceforth, the radiative rates in the "secondary" lines are held fixed at their equivalent-two-level-atom values, and only the "primary" lines are treated explicitly in the linearization. This will provide an adequate treatment of the secondary lines if they have been chosen astutely, and if they (a) are very weak, and therefore dominated by overlapping absorption-emission processes, or (b) are, in fact, "isolated", and therefore accurately described by a two-level atom, or (c) are only very weakly coupled to the lines of primary interest, even though they are members of, say, a multiplet, and the two-level-atom approximation is poor.

Starting from the initial solution just described, the linearized equations (12-40) are now solved for δJ at all depths. The resulting δJ 's are used to obtain a more accurate estimate of the radiation field; the radiative rates are then updated with this revised field, and the statistical equilibrium equations are re-solved for new level populations. With the new occupation numbers, opacities and emissivities may be computed, and a formal solution (Λ -iteration) is then performed to obtain the radiation field and Eddington factors (this step also provides a smoothing of the solution). The convergence of the method is ordinarily very swift, yielding $\|\delta J_v / J_v\| \lesssim 10^{-5}$ in 4 or 5 iterations, typically with order-of-magnitude improvement between successive iterations. This scheme is the one used to carry out most of the work discussed in §12-4. A detailed description of a particular version of the method, including a program adapted for calculations in the solar atmosphere, is given in (36).

A difficulty with the Feautrier-type approach developed above is that it becomes costly for computations involving large numbers of frequencies.

The problem can be overcome, however, with a new method (37) that uses a Rybicki-type elimination. Again we assume that at frequency v_k there is only one transition (t), arising from levels l and u . At this particular frequency, the linearized transfer equation (7-39) can be written, in view of equations (12-38), as

$$\mathbf{T}_k \delta J_k + \mathbf{L}_k \delta n_l + \mathbf{U}_k \delta n_u = \mathbf{R}_k \quad (12-42)$$

where each of the δ -vectors contains the *depth* variation of the quantity—e.g.,

$$\delta \mathbf{J}_k = (\delta J_{1k}, \dots, \delta J_{dk}, \dots, \delta J_{Dk})^T \quad (12-43)$$

and the matrices \mathbf{T}_k , \mathbf{L}_k , and \mathbf{U}_k are of dimension $(D \times D)$ and are tridiagonal. Equation (12-42) may be solved to obtain an equation of the form

$$\delta \mathbf{J}_k + \mathcal{L}_k \delta n_l + \mathcal{U}_k \delta n_u = \mathcal{R}_k \quad (12-44)$$

where \mathcal{L} and \mathcal{U} are now full matrices. Now the basic radiation-dependent quantities entering the rate equations are radiative *rates* integrated over the transitions in question. We therefore introduce the variations in the net rates, defined as

$$\begin{aligned} (\delta Z_t)_d &= n_{l,d} \delta R_{lu,d} - n_{u,d} \delta R_{ul,d} \\ &= \sum_k [4\pi w_k \alpha_{lu}(v_k)/hv_k] [n_{l,d} - G_{lu}(v_k)n_{u,d}] \delta J_{dk} \end{aligned} \quad (12-45)$$

where the sum extends only over those frequencies contained within transition t . If we substitute equations of the form of (12-44) into (12-45), and perform the indicated summations, we obtain finally

$$\delta Z_t + A_t \delta n_l + B_t \delta n_u = C_t \quad (12-46)$$

where A_t and B_t are full matrices.

Exercise 12-4: (a) Write explicit expressions for the elements of the matrices \mathbf{T}_k , \mathbf{L}_k , and \mathbf{U}_k , and the vector \mathbf{R}_k in equation (12-42). (b) Assuming that the matrices \mathcal{L}_k , \mathcal{U}_k , and the vector \mathcal{R}_k are known, write explicit expressions for the elements of A_t , B_t , and C_t in equation (12-46).

From equations (5-108) and (12-39) it follows that one can write

$$\delta n_m = \sum_i D_{mi} \delta Z_i \quad (12-47)$$

where D_{mi} is a diagonal matrix with elements $(D_{mi})_d = (\partial n_m / \partial Z_i)_d = (\mathcal{A}_d)_{mj}^{-1} - (\mathcal{A}_d)_{mi}^{-1}$, where \mathcal{A}_d is the unperturbed rate matrix at depth-point d , and i and j are the lower and upper states in transition t . Using equation (12-47) in equation (12-46), we obtain the system

$$\begin{aligned} E_t \delta Z_t &\equiv (I + A_t D_{ll} + B_t D_{uu}) \delta Z_t \\ &= C_t - A_t \sum_{i' \neq t} D_{li'} \delta Z_{i'} - B_t \sum_{i' \neq t} D_{ui'} \delta Z_{i'} \end{aligned} \quad (12-48)$$

with one such equation for each transition t .

The overall size of the system (12-48), which contains the full transition-to-transition coupling (interlocking) over all depth-points, is $(DT \times DT)$. A direct solution of these equations would thus require a time that scales as $T_D = c D^3 T^3$, which for, say, $T \sim 20$ and $D \sim 50$ becomes impractically large. The system is therefore solved by iteration, using a *successive over-relaxation (SOR) method* (526, 438). In this approach there are two basic iteration cycles: (a) the SOR iteration, to obtain a definite set of δZ_i 's ($i = 1, \dots, T$) within a given stage of linearization, and (b) the overall linearization procedure, where successive sets of δZ_i 's are used to update rates, and the full statistical equilibrium equations are then re-solved. The SOR procedure is started by computing the solutions of the systems $E_t \delta Z_i^{(0)} = C_t$ ($i = 1, \dots, T$); this initial solution requires $c D^3 T$ operations, and the resolved systems (equivalent to E_t^{-1}) are saved. Then with any set of current estimates of the δZ 's, the righthand side of equation (12-48) can be evaluated for each transition in turn (note that only vector multiplications are involved, so the procedure is very fast); this yields a single vector of known value on the righthand side, and, using the previously resolved E_t , a new value of δZ_i is obtained. Each cycle in the SOR procedure requires $c D^2 T^2$ operations, so if I iterations are necessary, the overall computing time scales as $T_{\text{SOR}} = c D^3 T + c' I D^2 T^2$, which is clearly favorable compared to T_D if $I < DT$.

By actual tests it is found (37) that this method works well, even though the SOR iterations resemble the equivalent-two-level-atom approach, in that only one transition at a time is treated. The reason is that this part of the calculation is required only to determine the δZ 's, which are merely one step of the overall linearization procedure (in itself designed to handle the interlocking problem self-consistently). Inasmuch as further steps in the linearization are presumed, the δZ 's at any given stage need not be known perfectly, but only with sufficient accuracy that the *error* in the current estimate of δZ is smaller than the *full size* of the δZ 's of the next linearization step. In practice, the requirement $|\delta Z_i^{(i)} - \delta Z_i^{(i-1)}| < \epsilon |\delta Z_i^{(i)}|$ (where i denotes the SOR iteration number) works well with ϵ set at about 10^{-2} . Both of the methods described in this section have proven to be very effective in a wide variety of physical problems, for different atoms, in stellar atmospheres of various types; we now turn to a discussion of some of the results obtained for early-type stars.

12-4 Light-Element Spectra in Early-Type Stars

From our study of the combined equations of transfer and statistical equilibrium, we have gained deep insight into the physics of spectral line-formation in stellar atmospheres. But it has also emerged that, when departures from LTE are taken into account, the equations to be solved become extremely intricate, and require special methods (which are computationally expensive).

It is therefore of considerable interest to answer the questions: "Do departures from LTE actually have a sensible effect in real stellar spectra?" "Are serious errors made in diagnostics of element abundances, or physical properties of the atmosphere, when non-LTE effects are ignored?" "Are there regions of the spectrum, portions of the H-R diagram, or classes of atoms and ions, for which we can conclude categorically that the use of an LTE approximation is safe, or is unsound?" From the practical point of view, it is important to know when it is adequate to assume LTE in the analysis of a stellar spectrum, for then the amount of computational work required is greatly reduced. Equally important is knowledge of when the results obtained from such analyses are *not* to be trusted. Answers to the questions posed above have come forth only quite recently as it became possible to obtain accurate numerical solutions of the non-LTE transfer equations, for elaborate multilevel atomic models in realistic model atmospheres, by applying on high-speed computers the techniques discussed in this chapter. It is now known that non-LTE effects are indeed of great consequence in several situations of basic interest and importance, and that a number of serious discrepancies between theory and observation are removed when departures from LTE are taken into account. A few of the results obtained thus far will be described below; further details can be found in the papers cited as well as reviews given in (433; 434; 435). It is not an exaggeration to state that work in this essential area has just begun, and much is yet to be learned from further efforts.

In many respects, the most fundamental spectrum in early-type stellar atmospheres is that of hydrogen. Not only do the hydrogen-line profiles serve as effective tools to measure basic stellar parameters, such as the effective temperature and surface gravity, but also, when one recognizes that hydrogen dominates the transfer of radiation through the major part of the spectrum in early-type stars, one realizes that a serious discrepancy between theory and observation for these lines has grave implications for the overall properties of the radiation field. Although very good agreement is usually obtained between predicted and observed H-line profiles for B- and A-type stars (cf. §10-5), strong disagreement has been found for the O-stars ($T_{\text{eff}} > 30,000^{\circ}\text{K}$). The basic problem is that the H-lines are observed to have nearly-constant strength in the O-stars over the spectral range O9–O5 [as can be seen by inspection of the plates in (465) or (5)], while the LTE equivalent widths decrease markedly over the corresponding temperature range ($30,000^{\circ}\text{K} \leq T_{\text{eff}} \leq 50,000^{\circ}\text{K}$), owing to increased hydrogen ionization. This decrease can be offset somewhat by assuming a higher surface gravity in the models, but then inconsistencies arise. Typically it is found (420) that, if a match is made between the observed H-line *equivalent widths* and those calculated from LTE models, then the surface gravities required to obtain the fit are too large (by about a factor of 3) compared to those deduced from fundamental measurements of stellar masses and radii, or

from stellar-structure computations. Similarly, when detailed comparisons are made with line *profiles* (510), it is found that, if a fit is made to the line-wings, the line-core predicted by LTE is much too weak. These discrepancies vanish when departures from LTE are taken into account (436; 45), and it is found that the non-LTE profiles are invariably much stronger than the LTE profiles, as shown in Figure 12-9 for a typical model. A comparison between the observed equivalent widths of $\text{H}\beta$ and both LTE and non-LTE calculations is shown in Figure 12-10. It can easily be seen there that the non-LTE results are in much better agreement with observation, and that the LTE equivalent widths are systematically too small by factors of 3 to 5 in the extreme cases [see also (174)]. Further, an excellent fit can be obtained to observed profiles by using the non-LTE computations; this can be seen by comparing the fits displayed in (510) and (45), both of which use the same observational data. In sum, by taking into account departures from LTE, *major* improvements are obtained in matching observed H-line profiles for the O-stars. For the B-stars, the hydrogen lines are much less strongly affected by deviations from LTE, and for a line such as $\text{H}\gamma$, LTE actually provides a very good approximation. Some important effects are found for $\text{H}\alpha$ (511; 430), where departures from LTE produce a deeper line-core, and a shallower wing than given by LTE. The latter effect arises because at the depths where the $\text{H}\alpha$ -wing is formed, $b_3 > b_2$ (cf. §7-5) and therefore $S_{23} > B(v_{23}, T)$; the predicted changes have been confirmed by observation.

After hydrogen, helium is the next most important element in stellar atmospheres, and is represented by the He I spectrum in B-stars, and by both the He I and He II spectra in O-stars. These lines may be used to

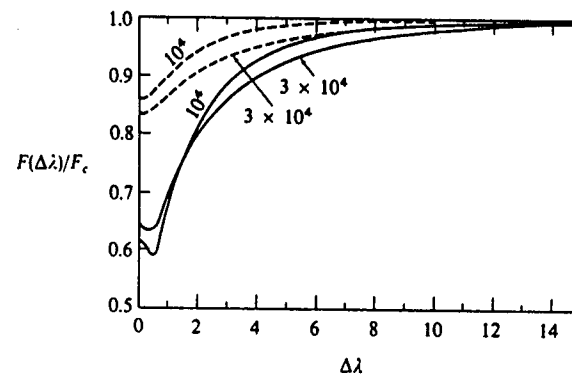


FIGURE 12-9
 $\text{H}\alpha$ profiles for O-star models with $T_{\text{eff}} = 45,000^{\circ}\text{K}$; curves are labeled with surface gravity g . Abscissa gives displacement from line-center in Å; ordinate gives residual flux. Solid curves: non-LTE profiles; dashed curves: LTE profiles. Note marked strengthening of line by non-LTE effects. From (45), by permission.

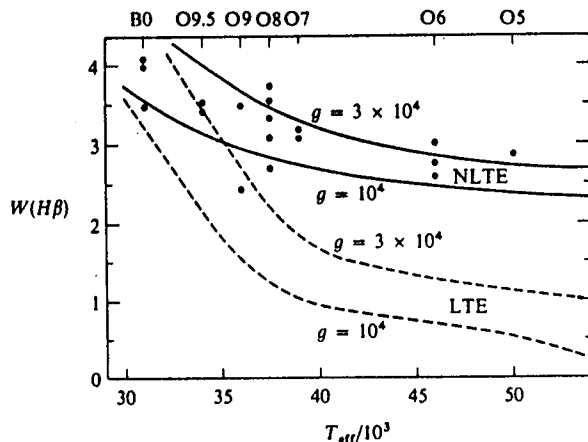


FIGURE 12-10
H β equivalent widths in O-stars. Solid curves: non-LTE calculations; dashed curves: LTE calculations. Dots: observed values (693). Ordinate gives equivalent width in Å; abscissae give ($T_{\text{eff}}/10^3$) and spectral types.

estimate the helium abundance $N(\text{He})/N(\text{H})$, and in the O-stars, the ratio of strengths of the He II lines to He I lines provides a sensitive temperature-indicator. LTE calculations of He I lines in B-stars have produced excellent agreement with the observations for the blue-violet lines [see, e.g. (390; 480; 481)], especially when the most accurate line-broadening theories available are used (438; 439). However, lines in the yellow-red regions of the spectrum [e.g., $\lambda 5876$ ($2p\ 3P - 3d\ 3D$) and $\lambda 6678$ ($2p\ 1P - 3d\ 1D$)] are always found to be stronger in B-star spectra than given by LTE computations, using the same model and abundance that fit the blue-violet lines. Formally these lines indicate abundances almost three times larger than that given by the blue-violet lines. When a detailed non-LTE calculation is made (46), using a realistic atomic model (see Figure 12-11), it is found that the lines mentioned above are strengthened dramatically, and that good agreement with observation is obtained, as shown in Figure 12-12 for $\lambda 6678$. It is interesting that the largest non-LTE effects are found for the lines with the smallest values of $h\nu$, for, as mentioned in §5-3, these lines, with relatively small values of $h\nu/kT$, have collisional rates that are comparable to the radiative rates, and the classical argument is that these lines should therefore be in LTE. The reason for the large effects can be seen by examining the source function in the limit $\delta \equiv h\nu/kT < 1$. If we write $(b_i/b_u) = (1 + \beta)$, then

$$(S_i/B_v) = (e^{h\nu/kT} - 1)/[(b_i/b_u)e^{h\nu/kT} - 1] \\ = (e^\delta - 1)/[e^\delta(1 + \beta) - 1] \approx \delta/(\beta + \delta) = (1 + \beta/\delta)^{-1}$$

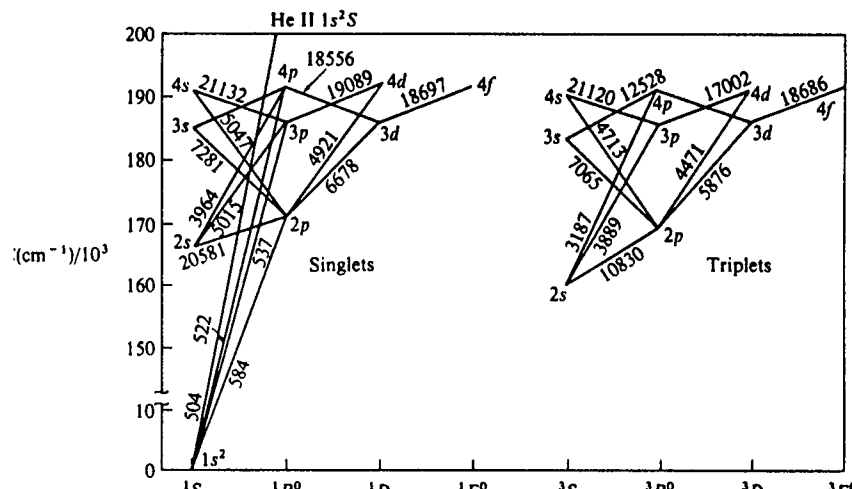


FIGURE 12-11
Model He I atom used in non-LTE calculation of He I spectrum. Ordinate gives wavenumber in cm^{-1} times 10^{-3} . All the transitions shown were included in the calculation explicitly as "primary" transitions in the sense defined in §12-3; all other dipole-permitted lines up through $n = 10$ were treated as "secondary" transitions, with rates fixed by an equivalent-two-level-atom computation. The singlets and triplets are treated separately. From (46), by permission.

which shows that a given fractional departure β of the level-population ratio is amplified by a factor δ^{-1} when $\delta < 1$. The occupation numbers, and hence the ratio (b_i/b_u) will, in general, be determined by processes other than those in the line. In the O- and B-stars the level populations are set by photo-ionizations and recombinations, and thus β will generally be nonzero despite a large collisional rate in a line. Once $\beta \neq 0$, large departures of S_i from B_v become possible; the same argument, by the way, explains why even tiny departures from LTE have very large effects in the radio-frequency recombination lines observed in nebulae (199). In the O-stars, LTE predicts too-weak lines for both He I and He II. If one attempts to match the observed equivalent widths, without regard to line-profiles (420), the derived helium abundances are about a factor of two higher than the value obtained from B-stars, or from the nebulae in the interstellar medium from which the O-stars have just formed. If a fit is made to the wings of the line profiles (510), it is again found that the line cores are much too weak. On the other hand, a non-LTE calculation (45) yields excellent agreement with observed line strengths and profiles at the "standard" abundance $N(\text{He})/N(\text{H}) = 0.1$ [see also (174; 175)].

Departures from LTE on occasion introduce large errors into abundance estimates based on LTE calculations. For example, LTE determinations of

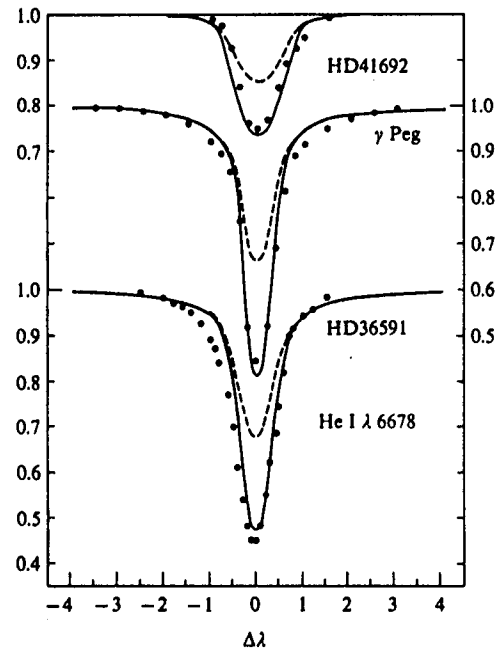


FIGURE 12-12
Comparison of observed (390) He I $\lambda 6678$ profiles (dots) with non-LTE (solid curves) and LTE (dashed curves) calculations for three B-stars. Ordinate: residual flux; abscissa: displacement from line-center in Å. From (46), by permission.

the abundance of Mg in O-stars are in error by a factor of 10 or more (431), and only when a non-LTE calculation is made, is a fit obtained to the observations, with an abundance near the solar (and accepted "cosmic") value, as shown in Figure 12-13 [see also (384; 586)]. Similarly, LTE analyses of the spectrum of Ne I in B-stars have routinely given a neon abundance of 5×10^{-4} relative to hydrogen, in disagreement with the value 10^{-4} obtained from nebulae, the solar corona, the solar wind, and cosmic rays (both galactic and solar-produced). Again the discrepancy is removed when a non-LTE calculation is done (47) and it is found that the Ne I spectrum, consisting primarily of lines in the red, is affected by essentially the same mechanism as that described above for He I. Finally, the spectra of Si III and Si IV in B- and O-stars show significant non-LTE effects (349). Departures from LTE increase the computed line-strengths by 50 to 70 percent, and line-core intensities decrease by a factor of 0.6 relative to LTE. To

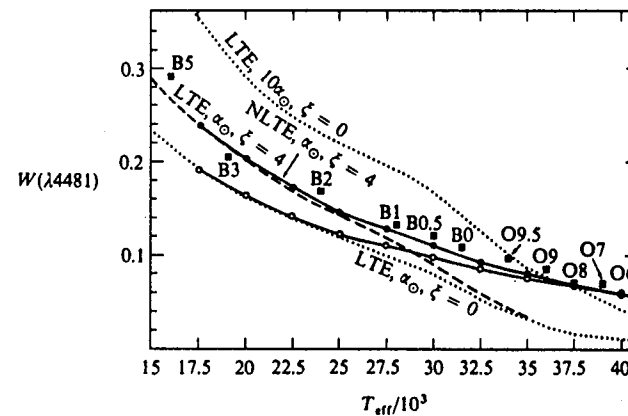


FIGURE 12-13
Strength of Mg II $\lambda 4481$ in B- and O-stars. Ordinate: equivalent width in Å; abscissa: $(T_{\text{eff}}/10^3)$. Squares: observed values at the indicated spectral types. Dotted curves: LTE calculations at a solar or ten-times solar Mg abundance, with zero microturbulence. Dashed curve: solar Mg abundance, and 4 km s^{-1} microturbulence. Solid curves: non-LTE calculation at solar Mg abundance, and zero (open circles) or 4 km s^{-1} (filled circles) microturbulence. Note that for the O-stars the choice of microturbulent velocity does not influence the result, and that the LTE predictions yield much too small a line-strength, while the non-LTE results agree well with the observations.

produce lines of similar strength in LTE, an abundance 5 to 7 times the solar value would be required. In short, there is ample evidence that, at least for early-type stars, deviations from LTE may produce large and important changes in abundance estimates.

Yet another context in which non-LTE effects enter preeminently in early-type stellar spectra is in the production of emission lines. For example, in the Of stars, the lines of He II $\lambda 4686$, C III $\lambda 5696$, and N III $\lambda\lambda 4634-41$ are seen in emission, while other lines of the same ionic spectra are in absorption. In the case of He II $\lambda 4686$, studies have been made of selective excitation mechanisms (45) and the effects of atmospheric extension in static models (376); while weak emission lines have been obtained in such work, it is clear that a quantitative fit to the observed line-strengths will be obtained only when large-scale atmospheric expansion is taken into account (see Chapters 14 and 15). The C III line has not yet been subjected to analysis. For the N III lines there exists a subgroup of the Of stars, designated O((f)), in which the N III lines are weakly in emission and the He II line is in absorption (657); these appear to be near-main-sequence objects in which the effects of atmospheric extension and expansion, if present at all, may be ignored.

A detailed non-LTE study of the N III doublet spectrum (429; 440; 443; 433) gives a plausible explanation of how the $\lambda\lambda 4634-41$ lines from the $3p^2P \rightarrow 3d^2D$ transition can be *in emission*, while the next lower multiplet, $\lambda\lambda 4097, 4103$ ($3s^2S \rightarrow 3p^2P$) is *in absorption*. The two essential ingredients required to produce this result are (a) a mechanism for populating the $3d$ state with enough electrons to induce the $3d \rightarrow 3p$ emission, and (b) a way of depopulating the $3p$ state so that emission does not appear in the $3p \rightarrow 3s$ transition. Both the $3s$ and $3d$ states can be populated directly by transitions from the ground state (see Figure 12-14) and, when the ultraviolet radiation field at $\lambda 374$ and $\lambda 452$ is intense, these states will have large occupation numbers. In *static* atmospheres, however, the resonance lines come into detailed balance, and therefore do not lead to a very large overpopulation of the $3d$ state. Rather, the overpopulation results from *dielectronic recombination* from the $2s2p(^1P)3d$ state—which, for the N^{++} ion, just happens to lie barely above the ionization limit. Stabilization of this state occurs when the $2p$ electron drops to the $2s$ level, and proceeds at a very rapid rate, feeding electrons directly into the $3d$ state. These electrons then decay $3d \rightarrow 3p$, producing the emission. Further, it turns out that, because of the particular structure of the N^{++} ion, the most probable route of exit from $3p$ is *not* $3p \rightarrow 3s$, but rather via “two-electron jumps” of the form $2s^23p \rightarrow 2s2p^2$ (see Figure 12-14); the latter process occurs so efficiently that it drains the $3p$ state, leaving the $3s \rightarrow 3p$ line in absorption. Inasmuch as the $\lambda\lambda 4634-40$

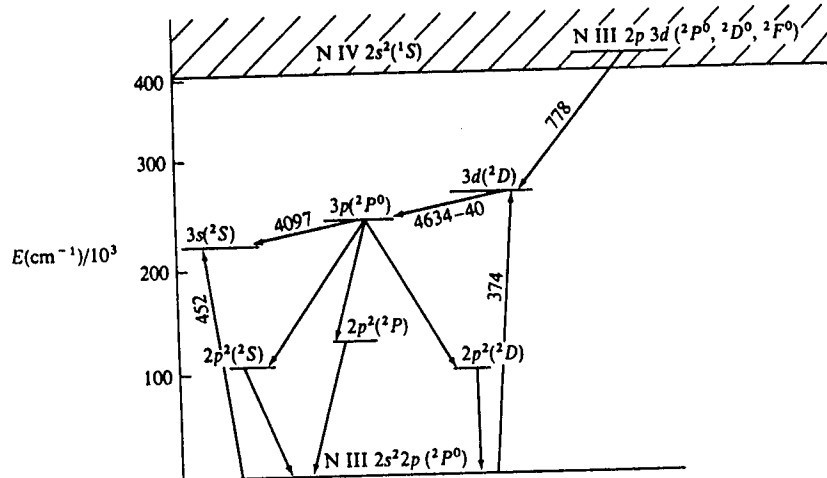


FIGURE 12-14
Simplified term diagram for the lower states of N^{++} , as well as the autoionizing state $2s2p(^1P)3d$ from which dielectronic recombinations can occur directly into the $2s^23d$ state, leading to emission at $\lambda\lambda 4634-40$.

41 emission lines can be produced in planar, static atmospheres, solely as a result of the atomic structure of the ion responsible, they must be regarded as *intrinsic* emission lines. In *expanding* atmospheres, direct pumping of the $3s$ and $3d$ states will occur in the $2p \rightarrow 3s$ and $2p \rightarrow 3d$ transitions, because the resonance lines will be Doppler shifted into the bright adjacent continuum and will not be in detailed balance. This greatly enhances the $3d \rightarrow 3p$ emission (thus explaining the very bright emission seen in the O stars, which are known to have expanding envelopes and stellar winds), while the increased $3s$ population, coupled with the drain from $3p$, assures that the $3s \rightarrow 3p$ lines remain in absorption. The calculations show (see Figure 12-15) that the $\lambda\lambda 4634-40$ lines make the transition from absorption to emission

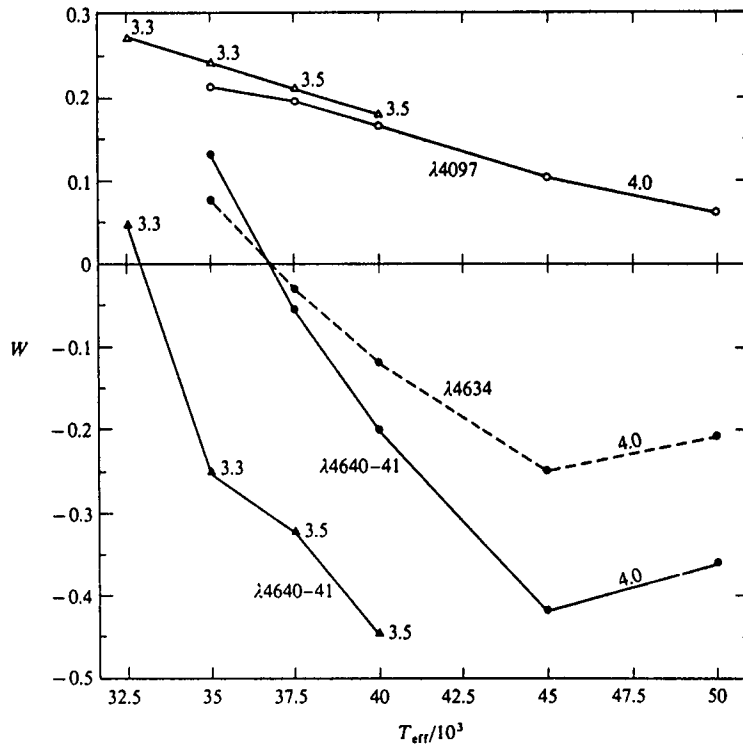


FIGURE 12-15
N III line-strengths for the $3s \rightarrow 3p$ ($\lambda 4097$) and $3p \rightarrow 3d$ ($\lambda\lambda 4634-40$) lines in planar, static, model atmospheres. Ordinate: equivalent width (negative values denote emission); abscissa: $(T_{\text{eff}}/10^3)$. Note that the $\lambda 4097$ line remains in absorption while $\lambda\lambda 4634-40$ make a transition from absorption to emission at a spectral type near O6. From (443) by permission.

at about spectral type O6 near the main sequence, in agreement with observation (443).

Many more analyses, for a wide variety of atoms and stellar atmospheres, need yet to be done (particularly for later spectral types) before the questions posed at the beginning of this section can be answered fully, and efforts in this direction will be richly rewarded with interesting results.

Line Formation with Partial Frequency Redistribution

In the process of *scattering* in spectral line-formation, an atom is excited from one bound level to another by the absorption of a photon, and then decays radiatively back to the original state, with the emission of a photon. In our work on line-transfer we have, thus far, assumed that scattering is either strictly coherent, or that the photons are completely redistributed over the line profile. Neither of these limits is achieved exactly in stellar atmospheres, and it is necessary to consider the redistribution of photons, in angle and frequency, in some detail, and to calculate *redistribution functions*, which describe the scattering process precisely. This calculation proceeds in two steps. We first consider a single atom in its own frame of reference, and compute the form of any redistribution that occurs within the substructure of the bound states. Then, recognizing that what is actually observed in a stellar atmosphere is an entire ensemble of atoms moving with a thermal velocity distribution, we take into account the Doppler redistribution in frequency produced by the atoms' motion. Doppler redistribution arises because the incident and emergent photons travel, in general, in different directions; in this event the projection of the atom's velocity vector along the propagation vectors will be different for the two photons, and a differential

Doppler shift must occur. The final redistribution function is obtained by averaging over all possible velocities. Once the redistribution function is known, a transfer calculation can be carried out, taking into full account any correlations (or lack thereof) between incoming and outgoing photon frequencies.

In this chapter the notation and methods of Hummer (313) will be adopted; the reader is referred to this paper for further details and other results. An interesting analysis of the problem from a rather different conceptual point of view can be found in (295) and (296).

13-1 Redistribution in the Atom's Frame

Let us first consider the nature of redistribution in the *rest frame of the atom*. Let the frequency displacement from line center of the incoming photon, *measured in the atom's frame*, be denoted by ξ' , its direction by n' , and the frequency displacement and direction of the outgoing photon by ξ and n . Assume that the material has no preferred directions on an atomic scale so that the atomic absorption profile $f(\xi')$ is isotropic; f is normalized such that $\int_{-\infty}^{\infty} f(\xi') d\xi' = 1$. Further, suppose that the *frequency redistribution function* $p(\xi', \xi)$ gives the probability that a photon absorbed in the frequency range $(\xi', \xi' + d\xi')$ is emitted into the range $(\xi, \xi + d\xi)$, while the *angular phase function* $g(n', n)$ describes the probability that the photon is scattered from solid angle $d\omega'$ in direction n' , into solid angle $d\omega$ in direction n . These functions are normalized such that

$$\int_{-\infty}^{\infty} p(\xi', \xi) d\xi' = \int_{-\infty}^{\infty} p(\xi', \xi) d\xi = 1 \quad (13-1)$$

$$\text{and } (4\pi)^{-1} \oint g(n', n) d\omega' = (4\pi)^{-1} \oint g(n', n) d\omega = 1 \quad (13-2)$$

The phase functions most useful in describing atomic scattering are those for isotropic and dipole scattering, given by equations (2-17) and (2-18).

In terms of the functions just defined, we may now write the probability that a photon (ξ', n') is absorbed as $f(\xi') d\xi' d\omega'/4\pi$, and the probability that, if a photon (ξ', n') is absorbed, then a photon (ξ, n) is emitted as $p(\xi', \xi)g(n', n)d\xi d\omega/4\pi$. Thus the *joint probability* that a photon (ξ', n') is absorbed and a photon (ξ, n) is emitted is $f(\xi')p(\xi', \xi) d\xi' d\xi g(n', n)(d\omega'/4\pi)(d\omega/4\pi)$.

We must now specify the functions $f(\xi')$ and $p(\xi', \xi)$. Following Hummer, we shall consider the following four categories: (a) Case I, zero line width; (b) Case II, radiation damping in the upper state, and coherence in the atom's rest frame; (c) Case III, complete redistribution in atom's frame; (d) Case IV, subordinate-line redistribution between two broadened states. Let us examine these in turn.

(a) **Case I.** Here we consider an idealized atom with two perfectly sharp states. Then $f(\xi') d\xi' = \delta(\xi' - \xi_0) d\xi'$, and $p(\xi', \xi) = \delta(\xi' - \xi)$ where δ denotes the Dirac function, and ξ_0 is the line-center frequency; clearly there is no redistribution in the atom's frame in this case. It is obvious that the conditions described here do not apply to any real line, for normally one (or both) levels will be broadened. It is useful, nevertheless, to study this limiting case, for it demonstrates the effects of Doppler redistribution *alone*, as seen by an observer in the laboratory frame examining the ensemble of moving atoms.

(b) **Case II.** Here we envision an atom with a perfectly sharp lower state, and an upper state whose finite lifetime against radiative decay (back to the lower state) leads to a Lorentz profile

$$f(\xi') = (\delta/\pi)/[(\xi' - \xi_0)^2 + \delta^2] \quad (13-3)$$

where $\delta \equiv \Gamma_R/4\pi$, and Γ_R is the radiative damping width of the upper state. We assume that there are no additional perturbations of the atom while it is in its upper state; then there will be no reshuffling of electrons among substates of the upper state, and the decay to the lower state will produce a photon of exactly the same frequency as was absorbed. Thus we again have $p(\xi', \xi) = \delta(\xi' - \xi)$. This case applies to resonance lines in media of such low densities that collisional broadening of the upper state is completely negligible—for example, the Lyman α line of hydrogen in the interstellar medium.

(c) **Case III.** The basic physical picture here is of an atom with a perfectly sharp lower state, and a broadened upper state, in a medium where collisions are so frequent that *all* excited electrons are randomly reshuffled over the substates of the upper state before emission occurs. The absorption profile is again the Lorentz profile given by equation (13-3), where δ now represents the full width (radiative plus collisional) of the upper state. In this extreme limit, the frequency of the emitted photon will have *no correlation* with the frequency of that absorbed; the probability for emission at any particular frequency is then proportional to the number of substates present at that frequency, and hence to the absorption profile itself. When complete redistribution in the atom's frame occurs we thus have

$$p(\xi', \xi) d\xi = f(\xi) d\xi = (\delta/\pi) d\xi/[(\xi - \xi_0)^2 + \delta^2] \quad (13-4)$$

which shows clearly that $p(\xi', \xi)$ is independent of ξ' , and that the joint probability of absorption at ξ' and emission at ξ is proportional to $f(\xi')f(\xi)$.

(d) **Case IV.** Here we suppose that the line is formed by an absorption from a broadened state i , to a broadened upper state j , followed by a radiative decay to state i . This picture is appropriate to scattering in subordinate lines. Because the electron returns to the same level as that from which it was

excited, the entire circuit is treated as a single quantum-mechanical process, and an expression is obtained for the product $f(\xi')p(\xi', \xi)$. An expression for the joint probability of absorption and emission was derived by Weisskopf (663) and by Woolley (683). A subsequent analysis by Heitler (293, 198) yielded a different result that was widely quoted in the astrophysical literature, but is now known to be in error (489, 195); the earlier formula is, in fact, correct. The derivation is straightforward but lengthy, so only the final expression will be quoted here, namely

$$\begin{aligned} f(\xi')p(\xi', \xi) &= (\delta_i^2 \delta_j / \pi^2) 4(\delta_i + \Delta) / \{[(\xi' - \xi_0)^2 + \Delta^2][(xi - \xi_0)^2 + \Delta^2][(xi' - xi)^2 + 4\delta_i^2]\} \\ &\quad + (\delta_i \delta_j / \pi^2) / \{[(xi - \xi_0)^2 + \Delta^2][(xi - xi')^2 + 4\delta_i^2]\} \\ &\quad + (\delta_i \delta_j / \pi^2) / \{[(xi - xi')^2 + 4\delta_i^2][(xi' - \xi_0)^2 + \Delta^2]\} \\ &\quad + (\delta_i^2 / \pi^2) / \{[(xi' - \xi_0)^2 + \Delta^2][(xi - \xi_0)^2 + \Delta^2]\} \end{aligned} \quad (13-5)$$

where $\Delta \equiv \delta_i + \delta_j$ [see (684, 164–168) for a detailed derivation and discussion].

It is easy to show that $f(\xi')p(\xi', \xi) = f(\xi)p(\xi, \xi')$, as would be expected in the symmetrical process $i \rightarrow j \rightarrow i$. Further, by inspection of the denominators in equation (13-5), it is easy to see that for a given value of ξ , there are two relative maxima, one with $\xi' = \xi$ and the other with $\xi' = \xi_0$. These can be understood physically as follows. (1) Most absorptions will arise from the center of the lower level; when these excite a particular substate of the upper state, the decay occurs most often back to the center of the lower level. It is clear that ξ will then equal ξ' , and that this process occurs with a relatively high probability. (2) Alternatively, there is a very high probability that an atom will be excited from the center of the lower state to the center of the upper by photons with $\xi' = \xi_0$; the upper state may then decay to any arbitrary substate of the lower, in particular, yielding the frequency ξ . The inverse also occurs: a transition from an arbitrary substate of the lower level has high probability of exciting the center substate of the upper level, and the most probable decay is back to the center of the lower level. Thus there will be a peak in emission at line center (i.e., at $\xi = \xi_0$), and indeed one sees that there is such a peak in equation (13-5).

The laboratory-frame redistribution function corresponding to equation (13-5) has not appeared in the literature [owing to use of the erroneous result of Heitler], though it could be derived straightforwardly (the calculation would be tedious, however). Moreover, the formulation of a correct transfer equation for subordinate-line redistribution is quite complicated; we shall not, therefore, consider Case IV further in what follows.

Of the four cases defined above, Cases II and III are of the greatest astrophysical importance. In fact, neither of these extreme limits is attained, and

the typical situation of interest for resonance-line formation is one in which the upper state is broadened by both radiation damping and elastic collisions, with damping-widths δ_R and δ_C respectively. In this case, one would expect the line profile to be given by equation (13-3) with $\delta = \delta_R + \delta_C$. Of the atoms in the upper state, a fraction $\gamma \equiv \delta_R / (\delta_R + \delta_C)$ would be expected to decay radiatively, and hence to emit coherently in the atom's frame (recall the lower state is perfectly sharp). The remaining fraction $(1 - \gamma) = \delta_C / (\delta_R + \delta_C)$ would have suffered collisions, and would be expected to have been completely redistributed. Thus we could now write

$$p(\xi', \xi) = \gamma \delta(\xi' - \xi) + (1 - \gamma)(\delta/\pi) / [(\xi - \xi_0)^2 + \delta^2] \quad (13-6)$$

This result was derived by Zanstra (690; 691), who treated the radiating atom as a classical oscillator. A detailed quantum-mechanical calculation (489) recovers equation (13-6) when the lower state is presumed to be perfectly sharp. If inelastic collisions occur with sufficient frequency, δ_I , to contribute to the total width of the state, then $\delta = \delta_R + \delta_C + \delta_I$; we now write $\gamma \equiv (\delta_R + \delta_I) / (\delta_R + \delta_C + \delta_I)$, for it is only the elastic collisions that reshuffle atoms among upper-level substates (489). In this case it is also necessary to introduce an additional emission source accounting for collisional excitations of the upper level (see §13-4). In sum, we see that the redistribution function in this more general situation can be expressed as a linear combination of the results for Cases II and III.

13-2 Doppler-Shift Redistribution in the Laboratory Frame

GENERAL FORMULAE

Let us now consider the effects of the Doppler shifts introduced by the motion of the scattering atoms relative to the laboratory frame. In this section we shall derive expressions that describe the full angular and frequency dependence of redistribution in the scattering process. In practice, relatively few radiative transfer calculations of relevance to line formation in stellar atmospheres have been done with the scattering treated in this much detail (the dimensionality of the problem is large!), and the angle-averaged functions to be derived in §13-3 are generally much more useful in application. Following Hummer's treatment, we first deduce general formulae for the observer's-frame redistribution function, and then calculate explicit results for the specific cases defined above. As was discussed in §2-1, the redistribution function $R(v', n'; v, n) dv' dv (d\omega'/4\pi) (d\omega/4\pi)$ gives the joint probability of scattering a photon from a laboratory frame frequency $(v', v' + dv')$, and solid angle $d\omega'$ in direction n' , into frequency $(v, v + dv)$, and solid angle $d\omega$

in direction \mathbf{n} . The function is normalized such that [equation (2-7)]

$$(4\pi)^{-2} \oint d\omega' \oint d\omega \int_0^\infty dv' \int_0^\infty dv R(v', \mathbf{n}'; v, \mathbf{n}) = 1$$

Suppose an atom moving with velocity \mathbf{v} , which remains fixed during the scattering process, absorbs a photon (v', \mathbf{n}') and emits a photon (v, \mathbf{n}) , as measured in the laboratory frame. Neglecting the aberration of directions in transforming from the atom's frame to the laboratory frame, the corresponding atom's frame frequencies for the absorption and emission are

$$\xi' = v' - v_0(\mathbf{v} \cdot \mathbf{n}')/c \quad (13-7a)$$

and

$$\xi = v - v_0(\mathbf{v} \cdot \mathbf{n})/c \quad (13-7b)$$

As was shown in §13-1, the joint probability of absorption of a photon (ξ', \mathbf{n}') with subsequent emission of a photon (ξ, \mathbf{n}) measured in the atom's frame is $f(\xi')p(\xi', \xi)g(\mathbf{n}', \mathbf{n}) d\xi' d\xi (d\omega'/4\pi)(d\omega/4\pi)$. Transforming this expression to the laboratory frame via equations (13-7) we can write

$$R_v(v', \mathbf{n}'; v, \mathbf{n}) = f(v' - v_0\mathbf{v} \cdot \mathbf{n}'/c)p(v' - v_0\mathbf{v} \cdot \mathbf{n}'/c, v - v_0\mathbf{v} \cdot \mathbf{n}/c)g(\mathbf{n}', \mathbf{n}) \quad (13-8)$$

where the subscript v implies that the redistribution is produced by an atom of velocity \mathbf{v} . To find the net result for the entire ensemble of atoms, we must average over the velocity distribution, which is assumed to be Maxwellian. To perform this average, introduce an orthogonal triad of reference axes $(\mathbf{n}_1, \mathbf{n}_2, \mathbf{n}_3)$, with \mathbf{n}_1 and \mathbf{n}_2 chosen to be coplanar with \mathbf{n}' and \mathbf{n} , and with \mathbf{n}_1 bisecting the angle Θ between them (see Figure 13-1). Then we may write

$$\mathbf{n}' = (\cos \frac{1}{2}\Theta)\mathbf{n}_1 + (\sin \frac{1}{2}\Theta)\mathbf{n}_2 = \alpha\mathbf{n}_1 + \beta\mathbf{n}_2 \quad (13-9)$$

and

$$\mathbf{n} = (\cos \frac{1}{2}\Theta)\mathbf{n}_1 - (\sin \frac{1}{2}\Theta)\mathbf{n}_2 = \alpha'\mathbf{n}_1 - \beta'\mathbf{n}_2 \quad (13-10)$$

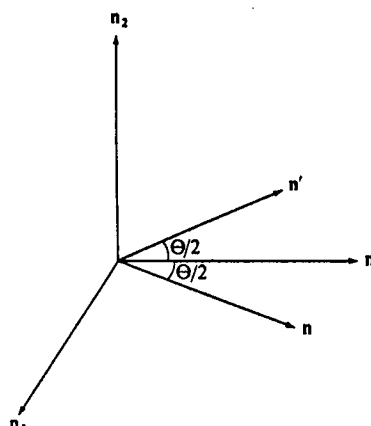


FIGURE 13-1
Coordinate axes used in calculation of redistribution function. The vectors \mathbf{n}_1 , \mathbf{n}_2 , \mathbf{n}_3 , and \mathbf{n}' are coplanar. The vector \mathbf{n}_1 bisects the angle Θ , $0 \leq \Theta \leq \pi$, between \mathbf{n}' and \mathbf{n} .

Resolve \mathbf{v} along these axes, and write $v_i = \mathbf{v} \cdot \mathbf{n}_i$; for convenience express velocities in dimensionless thermal units

$$u = v/v_{\text{thermal}} = (m_A/2kT)^{\frac{1}{2}}v \quad (13-11)$$

where m_A is the mass of an atom, and introduce the Doppler width

$$w = (v_0/c)(2kT/m_A)^{\frac{1}{2}} = v_0(v_{\text{thermal}}/c) \quad (13-12)$$

Then the Maxwellian velocity distribution [equation (5-1)] is

$$P(u_1, u_2, u_3) du_1 du_2 du_3 = \pi^{-\frac{3}{2}} \exp[-(u_1^2 + u_2^2 + u_3^2)] du_1 du_2 du_3 \quad (13-13)$$

We now average equation (13-8) against the velocity distribution of equation (13-13) to obtain

$$\begin{aligned} R(v', \mathbf{n}'; v, \mathbf{n}) &= \int_{-\infty}^{\infty} du_1 \int_{-\infty}^{\infty} du_2 \int_{-\infty}^{\infty} du_3 P(u_1, u_2, u_3) R_u(v', \mathbf{n}'; v, \mathbf{n}) \\ &= \pi^{-1} g(\mathbf{n}', \mathbf{n}) \int_{-\infty}^{\infty} du_1 e^{-u_1^2} \int_{-\infty}^{\infty} du_2 \\ &\quad \times e^{-u_2^2} f[v' - w(\alpha u_1 + \beta u_2)] \\ &\quad \times p[v' - w(\alpha u_1 + \beta u_2), v - w(\alpha u_1 - \beta u_2)] \end{aligned} \quad (13-14)$$

where the integration over u_3 has been carried out explicitly. An alternative form for R , which will prove useful, can be derived by choosing \mathbf{n}_1 to lie along \mathbf{n}' . Then $\mathbf{v} \cdot \mathbf{n}' = v_1$, while

$$\mathbf{v} \cdot \mathbf{n} = v_1 \cos \Theta + v_2 \sin \Theta = \alpha' v_1 + \beta' v_2 \quad (13-15)$$

We then find

$$\begin{aligned} R(v', \mathbf{n}'; v, \mathbf{n}) &= \pi^{-1} g(\mathbf{n}', \mathbf{n}) \int_{-\infty}^{\infty} du_1 e^{-u_1^2} f(v' - wu_1) \\ &\quad \times \int_{-\infty}^{\infty} du_2 e^{-u_2^2} p[v' - wu_1, v - w(\alpha' u_1 + \beta' u_2)] \end{aligned} \quad (13-16)$$

With the aid of these general formulae, we can now compute the redistribution functions for the various cases defined in §13-1. Note first, however, that in both Cases I and II the scattering is coherent in the atom's frame, so that

$$p(\xi', \xi) = \delta(\xi' - \xi) = \delta(v - v' + 2w\beta u_2) \quad (13-17)$$

In these cases u_1 no longer appears explicitly in the expression for p , and the integrations written above are simplified. Substituting equation (13-17) into (13-14), the integration over u_2 can now be performed explicitly (transforming to the variable $z \equiv 2w\beta u_2$ in order to preserve normalization of the Dirac

δ -function). We then obtain, for $\beta \neq 0$,

$$R_c(v', n'; v, n) = \frac{g(n', n)}{2\pi\beta w} \exp\left[-\frac{(v - v')^2}{4\beta^2 w^2}\right] \times \int_{-\infty}^{\infty} e^{-u^2} f\left[\frac{1}{2}(v + v') - wau\right] du \quad (13-18)$$

while if $\beta = 0$ we find

$$R_c(v', n'; v, n) = \pi^{-\frac{1}{2}} g(n', n) \delta(v' - v) \int_{-\infty}^{\infty} e^{-u^2} f(v' - wu) du \quad (13-19)$$

Here the subscript c denotes coherence in the atom's frame.

Exercise 13-1: Verify equations (13-18) and (13-19).

Finally, we note that the results can be written in a concise and convenient form by expressing frequency displacements from line center in Doppler units:

$$x \equiv (v - v_0)/w \quad (13-20)$$

and $x' \equiv (v' - v_0)/w \quad (13-21)$

and writing

$$R(x', n'; x, n) \equiv R(v', n'; v, n)(dv'/dx')(dv/dx) = w^2 R(v', n'; v, n) \quad (13-22)$$

to yield normalization of $R(x', n'; x, n)$ when integrated over x' and x .

RESULTS FOR SPECIFIC CASES

(a) Case I. If we substitute $f(\xi') = \delta(\xi' - v_0)$ into equation (13-18), we obtain immediately

$$R_I(v', n'; v, n) = \frac{g(n', n)}{2\pi\alpha\beta w^2} \exp\left[-\frac{(v - v')^2}{4\beta^2 w^2}\right] \exp\left[-\frac{(v + v' - 2v_0)^2}{4\alpha^2 w^2}\right] \quad (13-23)$$

Now noting that $2\alpha\beta = 2 \sin(\frac{1}{2}\Theta) \cos(\frac{1}{2}\Theta) = \sin \Theta$, that $\alpha^2 + \beta^2 = 1$, and transforming to dimensionless units via equations (13-20) through (13-22), we have

$$R_I(x', n'; x, n) = [g(n', n)/\pi \sin \Theta] \exp[-x^2 - (x' - x \cos \Theta)^2 \csc^2 \Theta] \quad (13-24)$$

Exercise 13-2: Fill in the steps required to obtain equation (13-24).

From this result, we immediately notice that, even though the scattering in the atom's frame was presumed to be strictly coherent, there is significant redistribution in the laboratory frame. This is a point of very great physical significance, as was stressed by Thomas (622). He examined the frequency dependence of scattered radiation [cf. equation (2-9)] using several simple analytical expressions for the incident intensity, and showed that in the Doppler core ($x \lesssim 3$), over which the absorption profile varies by a factor of 10^4 , the emission profile departs from the absorption profile by less than a factor of four! Thus, within the Doppler core, the assumption of complete redistribution of the scattered radiation provides an excellent approximation (it will be easy to see this using the angle-averaged redistribution functions derived in §13-2; see also Figure 13-2). This result provided much of the motivation for assuming complete noncoherence in the treatment of line formation, as was done in Chapters 11 and 12. Outside the line core, complete redistribution is not achieved as closely, and one must use the correct redistribution function. For example, in the case considered here, a simple physical argument (597) shows that the radiation in the far line-wings is about two-thirds noncoherent, and one-third coherent. On the other hand, outside the Doppler core the line-wings will often be swamped by the continuum (unless the profile has a large damping parameter), in which event the details of redistribution become less significant.

(b) Case II. Here we substitute equation (13-3) into (13-18) to obtain

$$R_{II}(v', n'; v, n) = \frac{g(n', n)}{2\pi\alpha\beta w^2} \exp\left[-\frac{(v - v')^2}{4\beta^2 w^2}\right] \left(\frac{\delta}{\pi\alpha w}\right) \times \int_{-\infty}^{\infty} e^{-u^2} \left[\left(\frac{v' + v - 2v_0}{2\alpha w} - u \right)^2 + \left(\frac{\delta}{\alpha w} \right)^2 \right]^{-1} du \quad (13-25)$$

Transforming to dimensionless frequency units via equations (13-20) through (13-22), and recalling the definition of the Voigt function $H(a, v)$ [see equation (9-34)], we obtain, finally

$$R_{II}(x', n'; x, n) = \frac{g(n', n)}{\pi \sin \Theta} \exp[-\frac{1}{2}(x - x')^2 \csc^2 \frac{1}{2}\Theta] \times H[a \sec \frac{1}{2}\Theta, \frac{1}{2}(x + x') \sec \frac{1}{2}\Theta] \quad (13-26)$$

where $a \equiv (\delta/w)$. Although this result is relatively complicated, efficient methods to evaluate $H(a, v)$ exist, and R_{II} can be calculated fairly easily. As will emerge in §13-3, R_{II} simulates nearly complete redistribution in the line core ($x \lesssim 2.5$), but becomes nearly coherent in the line wings.

Exercise 13-3: Fill in the missing steps leading to equation (13-26).

(c) Case III. Here, as was noted in equation (13-4), $p(\xi', \xi)$ is independent of ξ' . In this case equation (13-16) is particularly useful, and substituting from equations (13-3) and (13-4) we find

$$R_{III}(v', n'; v, n) = \frac{g(n', n)}{\pi} \int_{-\infty}^{\infty} du_1 e^{-u_1^2} \left(\frac{\delta}{\pi} \right) [(v' - v_0 - wu_1)^2 + \delta^2]^{-1} \\ \times \int_{-\infty}^{\infty} du_2 e^{-u_2^2} \left(\frac{\delta}{\pi} \right) \{[v - w(u_1 \cos \Theta + u_2 \sin \Theta) - v_0]^2 + \delta^2\}^{-1} \quad (13-27)$$

Converting to dimensionless units, and again using the definition of the Voigt function, we find

$$R_{III}(x', n'; x, n) = \frac{g(n', n)}{\pi^2} \sigma \int_{-\infty}^{\infty} \frac{e^{-u^2} H(\sigma, x \csc \Theta - u \ctn \Theta)}{(x' - u)^2 + a^2} du \quad (13-28)$$

where $\sigma \equiv a \csc \Theta$ and $a \equiv (\delta/w)$. This result is no longer expressible in terms of simple functions, and must be evaluated by numerical integrations (529).

Exercise 13-4: Fill in the steps required to obtain equation (13-28).

Exercise 13-5: In the limit that Compton scattering effects are negligible (i.e., $hv/mc^2 \ll 1$ where m is the mass of an electron), the scattering of radiation by electrons is coherent, $p(\xi', \xi) = \delta(\xi' - \xi)$, and grey, $f(\xi) = \sigma_e = (8\pi e^4/3m^2 c^4)$. (a) Show that the redistribution function for electron scattering is

$$R_e(v', n'; v, n) = g(n', n) \left[\frac{mc^2}{4\pi kT(1 - \cos \Theta)v^2} \right]^{\frac{1}{2}} \exp \left[\frac{-mc^2(v - v')^2}{4kT(1 - \cos \Theta)v^2} \right]$$

[See (196; 475; 161; §86)]. (b) Show that for $T = 10^4$ K, $\lambda = 4000$ Å, $\Theta = \pi/2$, the characteristic width of the above redistribution is about 10 Å. This result suggests that spectral lines in early-type stars can be significantly broadened by electron scattering (159; 475; 161, §86; 318; 39).

SYMMETRY PROPERTIES

The functions obtained above have certain symmetry properties which often may be exploited to simplify the form of the transfer equation. To obtain these, it is convenient to rewrite the general result (13-14) in terms of x and x' ; let $\tilde{f}(v - v_0) \equiv f(v)$ and $\tilde{p}(v - v_0, v' - v_0) \equiv p(v, v')$. Then from equations (13-14), and (13-20) through (13-22)

$$R(x', n'; x, n) = w^2 \pi^{-1} g(n', n) \int_{-\infty}^{\infty} du_1 e^{-u_1^2} \int_{-\infty}^{\infty} du_2 \\ \times e^{-u_2^2} \tilde{f}[w(x' - \alpha u_1 - \beta u_2)] \tilde{p}[w(x' - \alpha u_1 - \beta u_2), w(x - \alpha u_1 + \beta u_2)] \quad (13-29)$$

Now for all four cases defined in §13-1, the scattering is symmetric in the atom's frame—i.e.,

$$\tilde{f}(\xi') \tilde{p}(\xi', \xi) = \tilde{f}(-\xi') \tilde{p}(-\xi', -\xi) \quad (13-30)$$

Suppose we replace $x' \rightarrow -x'$ and $x \rightarrow -x$ in equation (13-29); if we simultaneously change the signs on u_1 and u_2 [which we may do because the integrals span the entire range $(-\infty, \infty)$], we immediately see from equation (13-30) that

$$R(-x', n'; -x, n) = R(x', n'; x, n) \quad (13-31)$$

Next, noting that replacing $n' \rightarrow -n'$ and $n \rightarrow -n$ changes the sign of α and β , and recalling that $g(n', n)$ depends only on $n' \cdot n$, it is clear from equations (13-29) and (13-30) that

$$R(-x', -n'; -x, -n) = R(x', n'; x, n) \quad (13-32)$$

and from (13-31) and (13-32) it follows that

$$R(x', -n'; x, -n) = R(x', n'; x, n) \quad (13-33)$$

Equations (13-31) through (13-33) depend only on the validity of (13-30) and hence are rather generally true. Further, because R depends only on the angle between n' and n , we may interchange them without changing R ; i.e.,

$$R(x', n; x, n') = R(x', n'; x, n) \quad (13-34)$$

Next we notice that, for coherent scattering in the atom's frame (Cases I and II), the redistribution functions depend only upon $(x + x')$ and $|x - x'|$ [cf. equations (13-23) and (13-26)]; hence x and x' may be interchanged without altering R ; i.e.,

$$R_i(x, n'; x', n) = R_i(x', n'; x, n), \quad (i = I, II) \quad (13-35)$$

Finally, a transformation from $n' \rightarrow -n'$ changes the sign of α and β in the expressions for incoming photons, hence if $g(n', n)$ is an even function of $n' \cdot n$,

$$R(-x', -n'; x, n) = w^2 \pi^{-1} g(n', n) \int_{-\infty}^{\infty} du_1 e^{-u_1^2} \int_{-\infty}^{\infty} du_2 \\ \times e^{-u_2^2} \tilde{f}[w(-x' + \alpha u_1 + \beta u_2)] \tilde{p}[w(-x' + \alpha u_1 + \beta u_2), w(x - \alpha u_1 + \beta u_2)] \quad (13-36)$$

which will reduce to (13-29) in certain cases. In particular, the integrals will be equal if $\tilde{f}(\xi') = \delta(\xi')$ or if $\tilde{f}(\xi') \tilde{p}(\xi', \xi) = \tilde{f}(-\xi') \tilde{p}(-\xi', \xi)$. The former is true for Case I, while the latter is true for Case III where $\tilde{f}(\xi') = \tilde{f}(-\xi')$

and $\tilde{p}(\xi', \xi) = \tilde{f}(\xi)$. Hence we conclude that

$$R_i(-x', -n'; x, n) = R_i(-x', n'; x, -n) = R_i(x', n'; x, n), \quad (i = I, III) \quad (13-37)$$

where the second identity follows from equation (13-33).

APPLICATIONS

The solution of the transfer equation allowing for full angle and frequency redistribution is fairly difficult, and requires techniques more powerful than those discussed in this book; both Monte Carlo methods (31; 50) and difference-equation methods (460) have been developed to handle the problem. There are a number of situations where both angular and frequency effects may become important. For example, the escape of $L\alpha$ photons from a very thick nebula depends sensitively upon the details of the scattering process, and a complete, careful treatment is required (31). In addition, when the material has a macroscopic velocity, both the absorption and emission coefficients become angle-dependent in the observer's rest frame (cf. §2-1). There then results an inextricable coupling between angles and frequencies in the transfer problem (see §14-1), and the details of the redistribution process may be of consequence; in this book, however, we shall consider only the case of complete redistribution in moving media, and will not pursue this point further. Finally, when observable angle-dependent information is available (e.g., center-to-limb variations as measured in the solar atmosphere), the possible importance of angular effects in the redistribution process must be examined. The investigations of this question conducted thus far (640; 641; 460) show that, at least for semi-infinite plane-parallel atmospheres with homogeneous layers, the differences between results obtained using angle-averaged redistribution functions and those obtained using the full angle-dependent functions are negligible. On the other hand, for optically thin media or small-scale structures (e.g., chromospheric fine-structure, spicules, etc.) the angular effects are often quite important (186), and should be considered in detail. However, these questions lie beyond the scope of this book, and will not be discussed here; rather, we now turn to the derivation of angle-averaged redistribution functions, and then to their use in radiative transfer calculations.

13-3 Angle-Averaged Redistribution Functions

As was noted in §2-1, if we assume that the radiation at any particular point in the atmosphere is essentially isotropic, then the contribution to the

emissivity from scattering processes can be written in the form

$$\eta^s(r, v) = \sigma(r) \int_{-\infty}^{\infty} R(v', v) J_{v'} dv' \quad (13-38)$$

where $J_{v'}$ is the mean intensity and $R(v', v)$ is the *angle-averaged redistribution function*

$$R(v', v) \equiv (4\pi)^{-1} \oint R(v', n'; v, n) d\omega' \quad (13-39)$$

The rationale for this approach is essentially as follows. The radiation field will depart significantly from isotropy at any given frequency only at points whose optical depths τ_v from the surface are of order unity or less; at depths $\tau_v \gtrsim 1$, the radiation field is essentially isotropic. Now a basic characteristic of non-LTE line-formation that emerged clearly in Chapter 11 is that the surface value of the source function is determined by photons contributed from over *an entire destruction length*, and over virtually all of this region the radiation field will, in fact, be isotropic. We may expect, therefore, that even at the surface where $I(\mu, v)$ shows departures from isotropy, S_v will still have a value *already fixed* by processes occurring at depths where the anisotropy is negligible; hence the value of $I(\tau_v = 0, \mu, v)$ computed from this S_v should be quite accurate. On the other hand, use of the angle-averaged functions accounts completely for the frequency-reshuffling of scattered photons, the action of which (as we saw in Chapter 11) affects crucially the photon escape-probability, and hence the thermalization process. In short, in this approach we account for the critical aspects of the redistribution process, and sacrifice information only in an area of secondary importance.

The functions defined by equation (13-39) are normalized such that

$$\int_{-\infty}^{\infty} dv \int_{-\infty}^{\infty} dv' R(v', v) = 1 \quad (13-40)$$

Integration over all emitted photons yields the absorption profile

$$dv' \int_{-\infty}^{\infty} R(v', v) dv' = \phi(v') dv' \quad (13-41)$$

while integration over all absorptions yields the *natural-excitation emission profile* [cf. equation (2-14)]

$$\psi^*(v) dv = dv \int_{-\infty}^{\infty} R(v', v) dv' \quad (13-42)$$

If $R(v', v) = R(v, v')$ (we shall find this to be true for cases I-III), then clearly $\psi^*(v) = \phi(v)$. It should be emphasized, however, that $\psi^*(v)$ is *not*, in general,

the *actual emission profile* in the line when J_v varies over the line profile (see the discussion in §13-4); that profile follows, ultimately, from the equations of statistical equilibrium and knowledge of the frequency-variation of J_v .

Two hypothetical limiting cases sometimes considered are strict coherence and complete redistribution in the *laboratory frame*. In the former circumstance we would have

$$R(v', v) = \phi(v') \delta(v - v') \quad (13-43)$$

and in the latter

$$R(v', v) = \phi(v')\phi(v) \quad (13-44)$$

Neither of these limits can actually ever be achieved. As we have seen already, even if the scattering is strictly coherent in the atom's frame it is not in the laboratory frame unless the atoms have zero velocities (impossible). Further, as we shall see below, complete redistribution in the atom's frame does not produce exactly complete redistribution in the laboratory frame. However, in the latter situation it is nonetheless found that equation (13-44) does, in fact, provide a very good approximation to reality in most cases, and hence may normally be used to describe that limit. Note in passing that, because the dependences of R on v' and on v are *separated* in equation (13-44), the true emission profile $\psi_v \equiv \psi_v^* = \phi_v$, regardless of the behavior of J_v , which justifies our earlier use of this relation [but only if equation (13-44) is actually accurate!].

GENERAL FORMULAE

The integration indicated in equation (13-39) could, in principle, be carried out directly, using each of the redistribution functions derived in §13-2. This however, turns out to be rather complicated. It is simpler to derive first a general formula, by performing the angle-average for arbitrary $f(\xi')$ and $p(\xi', \xi)$, and then to obtain specific forms for the particular cases of interest. We begin by rewriting equation (13-8), using the Doppler units defined in equations (13-11) and (13-12):

$$R_u(v', n'; v, n) = f(v' - wu \cdot n')p(v' - wu \cdot n', v - wu \cdot n)g(n', n) \quad (13-45)$$

We now wish to fix v' and v and integrate over all angle. Choose an orthonormal triad (n_1, n_2, n_3) such that $u = un_3$. Then $u \cdot n = \mu u$ and $u \cdot n' = \mu' u$, where $\mu \equiv n \cdot n_3$ and $\mu' \equiv n' \cdot n_3$. An element of solid angle may be written $d\omega = d\mu d\phi$ where ϕ is the azimuthal angle around n_3 . The phase function $g(n', n)$ can be expressed in general as $g(\mu', \mu, \phi)$. Thus, angle-averaging

equation (13-45) we have

$$R_u(v', v) = (16\pi^2)^{-1} \int_0^{2\pi} d\phi \int_{-1}^1 d\mu' f(v' - w\mu' u) \\ \times \int_{-1}^1 d\mu p(v' - w\mu' u, v - w\mu u) \int_0^{2\pi} d\phi' g(\mu', \mu, \phi') \quad (13-46)$$

Define $g(\mu', \mu) \equiv (4\pi)^{-1} \int_0^{2\pi} g(\mu', \mu, \phi') d\phi' \quad (13-47)$

Then, noting that the integral over ϕ in equation (13-46) is trivial, we have

$$R_u(v', v) = \frac{1}{2} \int_{-1}^1 d\mu' f(v' - w\mu' u) \int_{-1}^1 d\mu g(\mu', \mu) p(v' - w\mu' u, v - w\mu u) \quad (13-48)$$

For simplicity, in what follows only *isotropic scattering* in the atom's frame will be considered; in the case $g(\mu', \mu) \equiv \frac{1}{2}$ [formulae for a dipole phase function are given in (313)]. Applying this restriction we have

$$R_{A,u}(v', v) = \frac{1}{4} \int_{-1}^1 d\mu' f(v' - w\mu' u) \int_{-1}^1 d\mu p(v' - w\mu' u, v - w\mu u) \quad (13-49)$$

Although equation (13-49) is general, it is not convenient in the case of coherent scattering in the atom's frame because of complications that arise in setting the limits of integration; let us, therefore, derive a more refined formula for this case.

If the scattering is coherent in the atomic frame,

$$p(v' - w\mu' u, v - w\mu u) = \delta[v' - v - wu(\mu' - \mu)] \quad (13-50)$$

Because the range of integration for μ' and μ is only $(-1, 1)$, it is clear that for a given value of u , the singularity of the δ -function will be outside the range of integration for sufficiently large values of $|v' - v|$, and $R_{A,u}(v', v)$ will, accordingly, be zero. Physically this corresponds to the fact that an atom moving with velocity u can change a photon's frequency by *no more than* $2uw$, this maximum shift occurring if the propagation vectors of the incoming and outgoing photons lie along the velocity vector and are oppositely directed. We substitute equation (13-50) into (13-49), and consider first the integration over μ . Let $y \equiv w\mu u$, and write

$$I = (wu)^{-1} \int_{-wu}^{wu} \delta[y - (v - v' + wu\mu')] dy \quad (13-51)$$

The integral will equal $(1/wu)$ if $-wu \leq v - v' + wu\mu' \leq wu$, and will be zero otherwise. Define $\Lambda(x)$ such that $\Lambda = 1$ if $-1 \leq x \leq 1$, and $\Lambda = 0$

otherwise. Then equation (13-49) can be rewritten, using equation (13-51), as

$$R_{A,u}(v', v) = (4wu)^{-1} \int_{-1}^1 f(v' - wu\mu') \Lambda[\mu' + (wu)^{-1}(v - v')] d\mu' \quad (13-52)$$

If u is sufficiently small, then $|(v - v')/wu| > 1$ and Λ will vanish for all values of μ' . Thus there is a minimum speed u_{\min} , whose value we must determine, for which scattering from v' to v can actually occur. Define $\bar{v} \equiv \max(v', v)$ and $\underline{v} \equiv \min(v', v)$. First suppose that $v > v'$; then the requirement that the argument of the Λ -function fall in the range $(-1, 1)$ implies that $[(v - v')/wu] - 1 = [(\bar{v} - \underline{v})/wu] - 1 \leq 1$; this inequality yields

$$u_{\min} = (\bar{v} - \underline{v})/2w = |v - v'|/2w \quad (13-53)$$

But the same result is obtained by similar reasoning if we assume $v' > v$; therefore equation (13-53) is general. For $u \leq u_{\min}$, R_u will be zero. For $u > u_{\min}$, a contribution to R_u will come from part of the range of integration over μ' . To determine this range, we suppose, for definiteness, that $v > v'$. Then a contribution is obtained when

$$-1 \leq \mu' \leq 1 - [(\bar{v} - \underline{v})/wu] = 1 - [(\bar{v} - \underline{v})/wu]$$

which implies that $\bar{v} - wu \leq \underline{v} - wu\mu' \leq \underline{v} + wu$; recalling that $\underline{v} = v'$ by hypothesis, the result just stated can be rewritten as

$$\bar{v} - wu \leq v' - wu\mu' \leq \underline{v} + wu \quad (13-54)$$

If we assume instead that $v' > v$, we again obtain equation (13-54), which is, therefore, general.

Now introducing the Heaviside function $\Phi(x, x_0)$, defined such that $\Phi = 1$ when $x > x_0$ and $\Phi = 0$ when $x < x_0$, making the substitution $y \equiv v' - wu\mu'$, and using equations (13-53) and (13-54), equation (13-52) may finally be written as

$$R_{A,u}(v', v) = (4w^2u^2)^{-1} \Phi(u - |v - v'|/2w, 0) \int_{\bar{v}-wu}^{\bar{v}+wu} f(y) dy \quad (13-55)$$

Finally, the results expressed in equations (13-49) and (13-55) must be averaged over the Maxwellian velocity distribution

$$P(u) du = \pi^{-1} e^{-u^2} (4\pi u^2) du \quad (13-56)$$

From equation (13-55) we then have for *coherence* in the atom's frame (Cases I and II)

$$R_A(v', v) = (\pi^{\frac{1}{2}} w^2)^{-1} \int_{u_{\min}}^{\infty} du e^{-u^2} \int_{\bar{v}-wu}^{\bar{v}+wu} f(y) dy \quad (13-57)$$

From equation (13-49) we have, for *noncoherence* in the atom's frame (e.g., Case III),

$$R_A(v', v) = \pi^{-\frac{1}{2}} \int_0^{\infty} du u^2 e^{-u^2} \int_{-1}^1 d\mu' f(v' - w\mu' u) \times \int_{-1}^1 d\mu p(v' - w\mu' u, v - w\mu u) \quad (13-58)$$

Finally it is convenient to use Doppler units [cf. equations (13-12), (13-20), and (13-21)] and write

$$R_A(x', x) = R_A(v', v)(dv'/dx')(dv/dx) = w^2 R_A(v', v) \quad (13-59)$$

RESULTS FOR SPECIFIC CASES

(a) Case I. Here $f(y) = \delta(y - v_0)$; hence the integral over y in equation (13-57) is nonzero only if $\bar{v} + wu \geq v_0 \geq \bar{v} - wu$. This implies that u_{\min} now becomes effectively $u'_{\min} = \max(|x'|, |x|)$, which clearly satisfies the inequality $u'_{\min} \geq u_{\min}$ as given by equation (13-53). Then from equations (13-57) and (13-59)

$$R_{I,A}(x', x) = \pi^{-\frac{1}{2}} \int_{u_{\min}}^{\infty} e^{-u^2} du = \frac{1}{2} \operatorname{erfc}(u_{\min}) \quad (13-60)$$

where the complimentary error function is defined as

$$\operatorname{erfc}(x) \equiv 2\pi^{-\frac{1}{2}} \int_x^{\infty} e^{-z^2} dz \quad (13-61)$$

Substituting for u_{\min} ,

$$R_{I,A}(x', x) = \frac{1}{2} \operatorname{erfc}[\max(|x|, |x'|)] \quad (13-62)$$

This redistribution function is easy to compute from well-known approximation formulae for $\operatorname{erfc}(x)$ (4, 299); asymptotic formulae and results for dipole scattering are given in (313).

A plot of $R_{I,A}(x', x)/\phi(x')$ is shown in Figure 13-2; the curves are labeled with the incoming photon frequency x' , and give the probability for emission at frequency x , per absorption, as a function of x . We see that a photon absorbed at frequency x' will be emitted with equal probability at all x such that $-|x'| \leq x \leq |x'|$, and with exponentially decreasing probability beyond this range. It is easy to understand this result. The absorption can occur only when $\zeta \equiv 0$ in the atom's frame. Therefore atoms absorbing at frequency x' in the laboratory frame have a velocity of at least x' Doppler units. As the emissions occur with equal probability in all directions, the photons can be redistributed with equal probability over the entire range $\pm x'$.

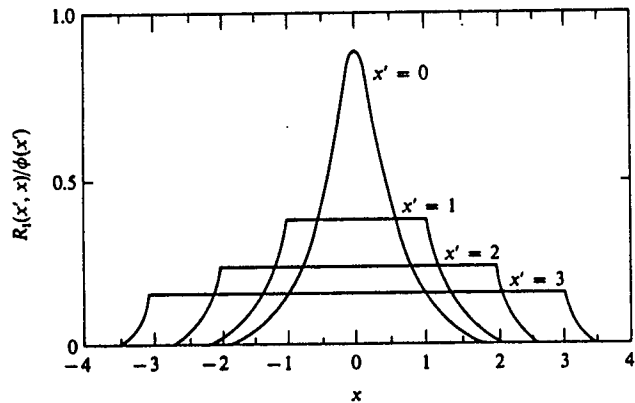


FIGURE 13-2
Probability of emission at frequency x , per absorption at frequency x' , for pure Doppler redistribution. Ordinate: $R_l(x', x)/\phi(x')$; abscissa: emission frequency x . Curves are labeled with frequency x' of absorbed photon.

(b) Case II. Substituting equation (13-3) into (13-57), we have

$$R_{II,A}(v', v) = (w^2 \pi^4)^{-1} \delta \int_{u_{min}}^{\infty} du e^{-u^2} \int_{v-wu}^{v+wu} dy [(y - v_0)^2 + \delta^2]^{-1} \quad (13-63)$$

Converting to Doppler units, writing $z = (y - v_0)/\delta = x/a$, and writing $u_{min} = \frac{1}{2}|x - x'|$ from equation (13-53) we have

$$\begin{aligned} R_{II,A}(x', x) &= \pi^{-\frac{1}{2}} \int_{|x'-x|/2}^{\infty} du e^{-u^2} \int_{(\bar{x}-u)/a}^{(\bar{x}+u)/a} dz (1 + z^2)^{-1} \\ &= \pi^{-\frac{1}{2}} \int_{|x'-x|/2}^{\infty} e^{-u^2} \left[\tan^{-1} \left(\frac{\bar{x} + u}{a} \right) - \tan^{-1} \left(\frac{\bar{x} - u}{a} \right) \right] du \end{aligned} \quad (13-64)$$

where $\bar{x} = \max(|x|, |x'|)$ and $\underline{x} = \min(|x|, |x'|)$. The asymptotic behavior of R_{II} , and results for dipole scattering, are given in (313); an accurate method for the evaluation of R_{II} is given in (6).

The redistribution function R_{II} is of great interest, for it describes the important case of scattering by a resonance line that is broadened by radiation damping, and it has been extensively studied. A plot of $R_{II,A}(x', x)/\phi(x')$ for $a = 10^{-3}$ is shown in Figure 13-3; again, the curves are labeled with the incoming photon frequency x' , and give the probability, per absorption, of a subsequent emission at frequency x . Here we see that for small x' ($x' \lesssim 3$), the curves resemble those for R_l , because most of the

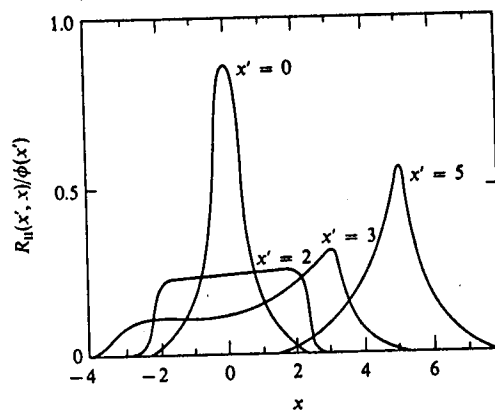


FIGURE 13-3
Probability of emission at frequency x , per absorption at frequency x' , for Doppler redistribution from a coherently scattering (in the atom's frame) Lorentz profile with $a = 10^{-3}$. Ordinate: $R_{II}(x', x)/\phi(x')$; abscissa: emission frequency x . Curves are labeled with frequency x' of absorbed photon.

emissions are from atoms absorbing at line center and moving with velocities near x' . For large x' there will be very few atoms with high-enough velocity to absorb at line center, and most emissions then come from atoms moving with low velocities and absorbing in the line-wing. As the scattering process is coherent in the atom's frame, and the appropriate atoms are nearly at rest in the laboratory frame, the scattering will be nearly coherent in the laboratory frame as well. Thus in the line-core there is Doppler redistribution and strong noncoherence, while in the wing the scattering is more nearly coherent; this dichotomy has important implications for the line-transfer problem, as we shall see in §13-4.

In early work by Jefferies and White (338), it was suggested that a simple approximation for R_{II} could be written in the form

$$R_{II,A}(x', x) \approx [1 - a(x)]\phi(x')\phi(x) + a(x)\phi(x)\delta(x - x') \quad (13-65)$$

where $a(x)$ is nearly zero for $x \lesssim 3$ and approximately unity for $x \gtrsim 3$. The original suggestion for the form of $a(x)$ is not adequate, however, and fails to meet requirements of normalization, symmetry, and wing-coherence. Nevertheless it is easy to define an appropriate function (358), and an approach of this type does simplify the calculation somewhat, although in the most precise work the correct form for R_{II} [equation (13-64)] should be used.

(c) Case III. In this case we no longer have coherence in the atom's frame, and equation (10-55) may be used without complication to give

$$\begin{aligned} R_{A,u}(v', v) &= \frac{1}{4} \int_{-1}^1 \frac{(\delta/\pi) d\mu'}{(v' - w\mu'u - v_0)^2 + \delta^2} \int_{-1}^1 \frac{(\delta/\pi) d\mu}{(v - w\mu u - v_0)^2 + \delta^2} \\ &= \frac{1}{4\pi^2 w^2 u^2} \left[\tan^{-1} \left(\frac{x' + u}{a} \right) - \tan^{-1} \left(\frac{x' - u}{a} \right) \right] \\ &\quad \times \left[\tan^{-1} \left(\frac{x + u}{a} \right) - \tan^{-1} \left(\frac{x - u}{a} \right) \right] \end{aligned} \quad (13-66)$$

Averaging over a Maxwellian velocity distribution and converting to Doppler units we have

$$\begin{aligned} R_{III,A}(x', x) &= \pi^{-\frac{1}{2}} \int_0^\infty e^{-u^2} \left[\tan^{-1} \left(\frac{x' + u}{a} \right) - \tan^{-1} \left(\frac{x' - u}{a} \right) \right] \\ &\quad \times \left[\tan^{-1} \left(\frac{x + u}{a} \right) - \tan^{-1} \left(\frac{x - u}{a} \right) \right] du \end{aligned} \quad (13-67)$$

Asymptotic formulae, results for dipole scattering, and computational methods for evaluation of R_{III} are given in (313, 212; 529).

A plot of $R_{III}(x', x)/\phi(x')$ for $a = 10^{-3}$ is shown in Figure 13-4. For small x' , most absorptions are at line center by atoms moving with velocities near x' , hence redistribution occurs with equal probability over the range $-x' \leq x \leq x'$, as was true for R_I and R_{II} . Again, for large x' most absorptions occur in the line wings of nearly stationary atoms, but now the emitted photons are completely redistributed over the absorption profile in the atom's frame, hence $R_{III}(x', x)/\phi(x') \rightarrow \phi(x)$ for $x' \gg 1$. It has, on occasion, been argued on intuitive grounds that if the redistribution process is completely noncoherent in the atom's frame, and if this is combined with random Doppler motions, then the redistribution should be completely noncoherent in the observer's frame as well; this conclusion is false, however, as is clearly shown by Figure 13-5. In fact, Doppler motions introduce a correlation between incoming and outgoing frequencies near the line core, and the deviations from complete frequency redistribution in the laboratory frame can be large. Despite these deviations, it turns out (see §13-4) that the assumption $R(x', x) = \phi(x')\phi(x)$ produces line profiles quite similar to those obtained from the exact $R_{III}(x', x)$, and in practice, the case of complete noncoherence in the atom's frame may be treated as complete noncoherence in the laboratory frame also, without serious errors.

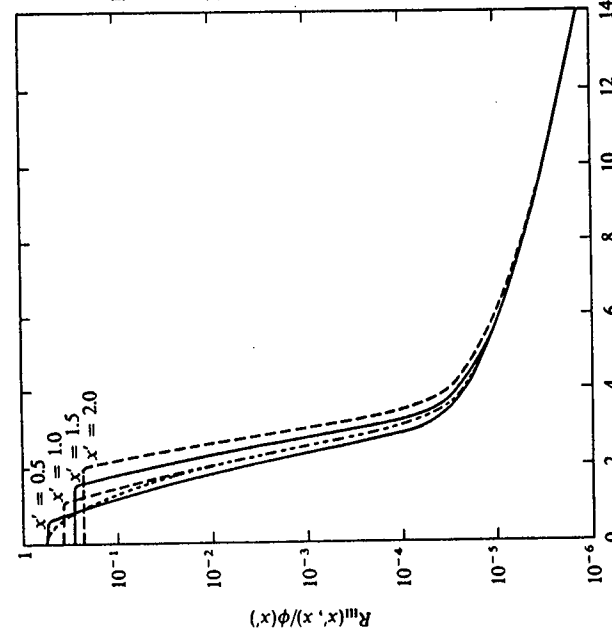
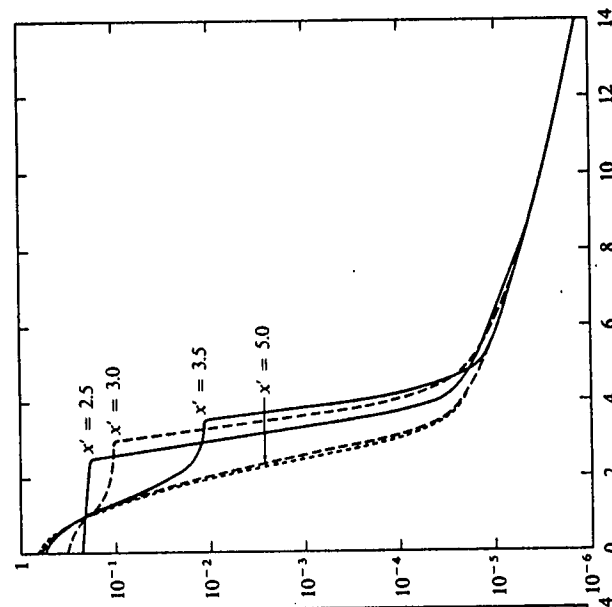


FIGURE 13-4
Probability of emission at frequency x per absorption at frequency x' for complete redistribution over a Lorentz profile in the atom's frame and Doppler redistribution in the laboratory frame, with $a = (\delta/w) = 10^{-3}$. Ordinate: $R_{III}(x', x)/\phi(x')$; note logarithmic scale. Dotted curve is the natural-excitation emission profile $\phi(x)$. Curves are labeled with frequency x' of absorbed photon. From (212), by permission.

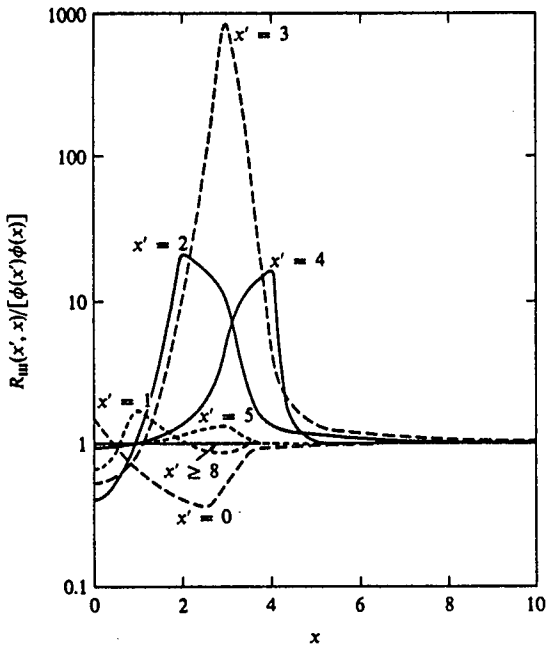


FIGURE 13-5
Ratio of actual redistribution function, for complete redistribution in the atom's frame and Doppler redistribution in the laboratory frame, $R_{III}(x', x)$, to the limiting case of complete noncoherence in the laboratory frame, $\phi(x')\phi(x)$. The absorption profile ϕ is a Voigt profile with $a = 10^{-3}$. From (212), by permission.

Exercise 13-6: Show that the angle-averaged redistribution function for scattering by electrons (under the same assumptions as employed in Exercise 13-5) is

$$R_{e, A}(v', v) = w^{-1} \operatorname{erfc}|(v' - v)/2w|$$

where $\operatorname{erfc}(x) \equiv \int_x^\infty \operatorname{erfc}(z) dz = \pi^{-1/2} e^{-x^2} - x \operatorname{erfc}(x)$

and w denotes the electron Doppler width, $w = v_0(2kT/m_e)^{1/2}/c$, which is about $43A^4$ times as large as the Doppler width of an atom of atomic weight A . See also (318) and (39).

SYMMETRY PROPERTIES

From equation (13-31) we see that, after angle-averaging, we must have

$$R(-x', -x) = R(x', x) \quad (13-68)$$

which is general so long as equation (13-30) holds. Further, by a direct extension of the arguments leading to equation (13-35) one finds

$$R_i(x', x) = R_i(x, x'), \quad (i = I, II, III) \quad (13-69)$$

The validity of this result can also be seen by inspection of equations (13-62), (13-64), and (13-67). From equation (13-69) it follows that the natural-excitation emission profile [see equation (13-42)]

$$\psi_i^*(x) \equiv \phi_i(x), \quad (i = I, II, III) \quad (13-70)$$

Exercise 13-7: Verify the result stated in equation (13-70) for Case I by direct integration of $R_{I,A}(x', x)$ over x' .

13-4 Radiative Transfer with Partial Redistribution

Consider now the problem of accounting for the effects of angle-averaged partial redistribution in spectral line formation. For simplicity we shall confine attention to a two-level atom with continuum, and develop a general method that gives a rigorous solution of the problem. (This method can be generalized easily to more complicated atomic models as well.) Next, a somewhat simpler, but less general, approach will be developed, which still treats the troublesome stimulated emission term correctly. Then a still simpler method, which treats the stimulated emission terms only approximately, will be described, and results from the application of this method in highly idealized models will be discussed. Finally, results from calculations of resonance-line profiles, using the general method, for realistic model atoms and stellar atmospheres, will be presented.

FORMULATION FOR A TWO-LEVEL ATOM

Let us examine the formation of a resonance line connecting a perfectly sharp lower level to an upper state that is broadened into a distribution of substates by both radiation damping and collisions. Denote the population of the lower level by n_1 , the total population of the upper level (summed over all substates) by n_2 , and the number of ions by n_k . The distribution of the atoms over the upper state is specified in terms of the *observer's-frame emission profile* ψ_v , defined as the fraction of all atoms in the upper state that, if they decay radiatively, emit photons of frequency v as seen in the laboratory frame. This method of counting atoms in the upper state is well-posed physically, for it describes the distribution in terms of *observables*; mathematically, ψ_v is a complicated, but unique, one-to-one mapping from the distribution of atoms over their own rest-frame frequencies ξ , and velocities v , the transformation being specified by the redistribution function

(456). Clearly ψ_v is normalized, and $n_2 = n_2 \int \psi_v dv$. We shall find it convenient to define an auxilliary variable \tilde{n}_2 such that $n_2(v) = n_2 \psi_v \equiv \tilde{n}_2(v) \phi_v$ gives the number of upper-state atoms in substates that can emit photons of frequency v ; the dominant variation of the upper-state distribution is factored out this way, and \tilde{n}_2 reflects only the departure from natural excitation.

The substate occupation number $n_2(v)$ (or, equivalently, ψ_v) is specified by a rate equation of the form

$$\begin{aligned} n_2(v)(A_{21} + B_{21}J_v + C_{21} + R_{2\kappa} + C_{2\kappa}) \\ = n_1 \left[B_{12} \int R(v', v) J_{v'} dv' + C_{12}\psi_v^* \right] + n_2^* \psi_v^*(R_{\kappa 2} + C_{2\kappa}) \end{aligned} \quad (13-71)$$

This equation has a simple physical interpretation [see also (456)]. The term on the lefthand side is the population of the substate, times the total rate of exit (a) to the ground state by spontaneous emissions, stimulated emissions and collisions, and (b) to the continuum by photoionizations and collisions. The only noteworthy term is that for stimulated emission which is *strictly coherent in both the laboratory and the atom's frame*. [This follows from the fundamental quantum-mechanical characteristics of the process (197, §62; 293, §17), in which a photon, incident upon the atom, induces an emission in such a way as to create yet another photon of *exactly the same properties*: energy (hence frequency), momentum (hence direction of propagation), and polarization. Thus a photon (v', n') in the laboratory frame undergoes a definite transformation (depending on n' and v) to (ξ', n') in the atom's frame, and creates another *identical* photon; both photons undergo *exactly the same inverse* transformation back into the laboratory frame, returning *two* photons (v', n') into the radiation field.] The terms on the righthand side describe processes of excitation to the substate $n_2(v)$, from the ground state and by recombinations from the continuum. The latter produce atoms in level 2 distributed according to the natural-excitation profile ψ_v^* ; n_2^* denotes the LTE particle density $n_2^* = n_1 n_e \Phi_2(T)$, where $\Phi(T)$ is the appropriate Saha-Boltzmann factor. For all three physically interesting cases of redistribution considered in §13-3, $\psi_v^* \equiv \phi_v$ [see equation (13-70)]. From the ground state, atoms excited by collisions are also distributed according to ψ_v^* . The radiative excitations are given by the number of absorptions of photons of frequency v' , namely $n_1 B_{12} J_{v'}$, times the joint probability $R(v', v)$ of absorbing at v' and emitting at v , summed over all v' . In the scattering process we assume that a fraction γ of all excited atoms emit coherently, and the remainder are completely redistributed in the atom's frame by elastic collisions [so that $p(\xi', \xi)$ is given by equation (13-6)]. The correct laboratory frame redistribution function in this case would be

$$R(v', v) = \gamma R_{II}(v', v) + (1 - \gamma)R_{III}(v', v) \quad (13-72)$$

but in practice it is adequate (and much easier) to use

$$R(v', v) = \gamma R_{II}(v', v) + (1 - \gamma)\phi_{v'}\phi_v \quad (13-73)$$

which assumes that complete redistribution in the atom's frame leads to complete redistribution in the observer's frame.

The rate equation for the ground state is

$$\begin{aligned} n_1 \left(B_{12} \int \phi_v J_v dv + C_{12} + R_{1\kappa} + C_{1\kappa} \right) \\ = n_2 \left(A_{21} + B_{21} \int \psi_v J_v dv + C_{21} \right) + n_1^*(R_{\kappa 1} + C_{1\kappa}) \end{aligned} \quad (13-74)$$

which has an interpretation entirely analogous to that of equation (13-71). Finally, the total number of atoms is presumed known, hence

$$n_1 + n_2 \int \psi_v dv + n_\kappa = n_{\text{atom}} \quad (13-75)$$

The required photoionization and recombination rates may be considered as given, in which event only the radiation field in the line needs to be calculated, or these rates may follow from a solution of the transfer equation in the continuum (assumed necessary for the ground state only).

The transfer equation to be solved may be written as

$$\partial^2(f_v J_v)/\partial \tau_v^2 = J_v - S_v \quad (13-76)$$

where, as usual, $d\tau_v \equiv -\chi_v dz$ and $S_v \equiv \eta_v/\chi_v$. In the line

$$\chi_v = \alpha_{12}[n_1 - (g_1/g_2)\tilde{n}_2(v)]\phi_v + X_v \quad (13-77)$$

and $\eta_v = (2hv^3/c^2)\alpha_{12}(g_1/g_2)\tilde{n}_2(v)\phi_v + E_v$ (13-78)

and in the ground-state continuum

$$\chi_v = \alpha_{1\kappa}(v)(n_1 - n_1^* e^{-hv/kT}) + X_v \quad (13-79)$$

and $\eta_v = (2hv^3/c^2)e^{-hv/kT}\alpha_{1\kappa}(v)n_1^* + E_v$ (13-80)

Here X_v and E_v represent (fixed) background opacity and emissivity sources, while $\alpha_{12} \equiv (B_{12}hv)/4\pi$.

The solution of the transfer equation is now quite complicated because the *emission profile* ψ_v is not known *a priori*, but follows from the statistical equilibrium equations (13-71) through (13-75). Unlike the case of complete redistribution, where only the ratio (n_2/n_1) is required to specify the source function [cf. equation (11-4)] and hence only one statistical equilibrium equation is needed, we must now compute ψ_v , and this introduces as many equations of the form of (13-71) as are required to define this function to

the desired precision. Indeed, the situation at hand strikingly resembles that of a multiline "multiplet" problem with very strong interlocking effects, each frequency within the line playing the role of a separate transition, and the line as a whole acting as the collective photon pool. This analogy suggests that the solution can be obtained effectively by means of a complete linearization technique.

METHODS OF SOLUTION

A general and powerful method of solving equations (13-71) through (13-75), simultaneously with the transfer equations (13-76) through (13-80), is to use the complete linearization technique. We introduce a discrete set of upper-state substates specified by frequencies $\{v_j\}$, measured relative to line center. The substate populations can then be written as $n_2(v_j) = \tilde{n}_{2j}\phi_j$, and the rate equations discretized as

$$n_1 \left(B_{12} \sum_j w_j \phi_j J_j + C_{12} + R_{1\kappa} + C_{1\kappa} \right) - \sum_j w_j \tilde{n}_{2j} \phi_j (A_{21} + B_{21} J_j + C_{21}) - n_\kappa [n_e \Phi_1(T) (R_{\kappa 1} + C_{1\kappa})] = 0 \quad (13-81)$$

$$-n_1 \left\{ B_{12} \left[\gamma \sum_j \mathcal{R}_{jj}^H J_j + (1-\gamma) \phi_j \sum_j w_j \phi_j J_j \right] + C_{12} \phi_j \right\} + \tilde{n}_{2j} \phi_j (A_{21} + B_{21} J_j + C_{21} + R_{2\kappa} + C_{2\kappa}) - n_\kappa [n_e \Phi_2(T) (R_{\kappa 2} + C_{2\kappa})] = 0 \quad (13-82)$$

$$\text{and} \quad n_1 + \sum_j w_j \tilde{n}_{2j} \phi_j + n_\kappa = n_{\text{atom}} \quad (13-83)$$

Here \mathcal{R}_{jj}^H is a discrete representation of $R^H(v_i, v_j)$ in an appropriate quadrature. Writing $\mathbf{n} \equiv (n_1, \tilde{n}_{21}, \tilde{n}_{22}, \dots, \tilde{n}_{2j}, \dots, \tilde{n}_{2\kappa}, n_\kappa)^T$, where J denotes the total number of substates, equations (13-81) through (13-83) are of the form $\mathcal{A}\mathbf{n} = \mathcal{B}$.

Suppose we have an estimate of the occupation numbers \mathbf{n} for all depths; then current values of χ_v , η_v , and J_v may be computed at all frequencies in the line and continuum. We may then linearize the transfer equation in terms of δJ_v , $\delta \chi_v$, and $\delta \eta_v$, and express the latter two quantities in terms of δn_1 , the δn_{2j} 's, and δn_κ . In turn, the δn 's can be written as $\delta \mathbf{n} = \sum (\partial \mathbf{n} / \partial J_k) \delta J_k$, where the sum extends over all frequencies in the line and continuum. The derivatives $(\partial \mathbf{n} / \partial J_k)$ can be written as $(\partial \mathbf{n} / \partial J_k) = -\mathcal{A}^{-1}[(\partial \mathcal{A} / \partial J_k) \cdot \mathbf{n}]$, and explicit analytical expressions can be obtained for the derivatives $(\partial \mathcal{A} / \partial J_k)$ [see (456; 459)]. The final system of equations to be solved is of the standard Feautrier form $-\mathbf{A}_d \delta \mathbf{J}_{d-1} + \mathbf{B}_d \delta \mathbf{J}_d - \mathbf{C}_d \delta \mathbf{J}_{d+1} = \mathbf{L}_d$ where

$$\delta \mathbf{J}_d \equiv (\delta J_{1d}, \dots, \delta J_{kd}, \dots, \delta J_{Kd})^T.$$

When the system is solved, the δJ_v 's are applied to the current estimates of J_v , and the rate equations (13-81) through (13-83) are re-solved for new \mathbf{n} 's. These values are used to compute χ_v and η_v , and a formal solution of the transfer equation updates the Eddington factors f_v . The whole process is iterated to convergence. The formalism can be extended (459) to include the case of several lines from different sharp lower levels to common broadened upper levels [e.g., the Ca II H - and K -lines and infrared triplet, for which the $4s$ ground state and metastable $3d$ levels are sharp, while $4p$ is broad (see Figure 12-1)]. The convergence properties of this method are good, typically yielding a factor of 5 to 10 reduction in errors in the solution per iteration.

The method described above is effective, but is relatively expensive computationally, and it is worthwhile to explore less costly approaches (292). One of the basic problems encountered in treating partial redistribution is that the unknown emission profile appears explicitly in the stimulated emission term in χ_v , and hence in the denominator of $S_v = \eta_v / \chi_v$. However, in many astrophysical applications, particularly for ultraviolet resonance lines in solar-type atmospheres, this stimulated emission correction, which is of order $\exp(-hv/kT)$, is extremely small. In this event we may proceed by iterating the ratio $\omega_v \equiv (\psi_v / \phi_v)$ in the stimulated emission term of an analytical expression for the source function obtained from manipulation of the statistical equilibrium equations.

Consider the source function for a strict two-level atom, omitting the continuum for simplicity. Using the Einstein relations we may write the line source function as

$$S_l(v) = \frac{(2hv^3/c^2)n_2\psi_v}{(g_2/g_1)n_1\phi_v - n_2\psi_v} = \frac{(2hv^3/c^2)(g_1n_2\psi_v/g_2n_1\phi_v)}{1 - (g_1n_2/g_2n_1)\omega_v} \quad (13-84)$$

Here, and in what follows, we assume that a current estimate of ω_v is known. From equation (13-71), omitting the continuum terms,

$$(2hv^3/c^2)(g_1n_2\psi_v/g_2n_1\phi_v) = \frac{A_{21}\phi_v^{-1} \int R(v', v) J_{v'} dv' + C_{21}(1 - e^{-hv/kT})B_v(T)}{A_{21} + B_{21}J_v + C_{21}} \quad (13-85)$$

and from equation (13-74)

$$[1 - (g_1n_2/g_2n_1)\omega_v] = \frac{A_{21} + B_{21}(J_e - \omega_v J_a) + C_{21}(1 - \omega_v e^{-hv/kT})}{A_{21} + B_{21}J_e + C_{21}} \quad (13-86)$$

where $J_a \equiv \int \phi_v J_v dv$ and $J_e \equiv \int \psi_v J_v dv = \int \phi_v \omega_v J_v dv$. Defining $\epsilon' \equiv C_{21}(1 - e^{-hv/kT})/A_{21}$ we have

$$S_l(v) = \xi_v \left[\phi_v^{-1} \int R(v', v) J_{v'} dv' + \epsilon' B_v \right] \quad (13-87)$$

where

$$\xi_v = \frac{[(A_{21} + B_{21}J_e + C_{21})(A_{21} + B_{21}J_v + C_{21})]}{1 + (B_{21}/A_{21})(J_e - \omega_v J_a) + (C_{21}/A_{21})(1 - \omega_v e^{-hv/kT})} \quad (13-88)$$

Using equation (13-87) in an expression for the total source function of the form

$$S_v = [\chi_i(v)S_i(v) + \chi_c S_c]/[\chi_i(v) + \chi_c] \quad (13-89)$$

where now

$$\chi_i(v) = \alpha_{12}[n_1 - (g_1/g_2)n_2\omega_v]\phi_v + X_v \quad (13-90)$$

the transfer equation now reduces to the general form

$$\partial^2(f_v J_v)/\partial\tau_v^2 = J_v - a_v \int R(v', v) J_{v'} dv' + b_v \quad (13-91)$$

which may be solved straightaway by the standard Feautrier technique. In this method we use *current* estimates of ω_v and J_v to calculate ξ_v in equation (13-88), and of the level populations and ω_v to determine $\chi_i(v)$ in equations (13-89) and (13-90). The transfer equation (13-91) is then solved for improved values of J_v . These J_v 's are then used in equations (13-81) through (13-83) to update n_1 , $\tilde{n}_2(v)$, and n_κ , and from these, ψ , and thus ω_v . The process is then iterated to convergence. One would expect this method to work well whenever $(B_{21}J/A_{21}) \ll 1$; when stimulated emissions are very important one must use the full linearization technique described above.

RESULTS FROM IDEALIZED MODELS

A great deal of insight into the nature of partial redistribution effects can be obtained from studies similar in spirit to those described in Chapter 11, using idealized model atmospheres and atoms. To simplify the problem as much as possible, it is customary to make the additional physical assumption that the stimulated emission profile is given by ϕ_v , not ψ_v , and that the stimulated emission rate in equation (13-71) can be written as $n_2(v)B_{21}J_a$ rather than $n_2(v)B_{21}J_v$. Then the parameter ω_v defined above is identically unity, $J_e \equiv J_a$, and $\xi_v \equiv (1 + \epsilon')^{-1}$, and equation (13-87) reduces to

$$S_i(v) = (1 - \epsilon)\phi_v^{-1} \int R(v', v) J_{v'} dv' + \epsilon B_v \quad (13-92)$$

where $\epsilon \equiv \epsilon'/(1 + \epsilon')$. With this source function, the transfer equation can be solved in a single step without iteration. This approach has been used to estimate the differences between the frequency-dependent $S_i(v)$, obtained when partial redistribution effects are taken into account, and the frequency-independent

$$S_i^{CR} = (1 - \epsilon) \int \phi_v J_{v'} dv' + \epsilon B_v \quad (13-93)$$

obtained from complete redistribution, for R_{II} , R_{III} , and $R_{I\!I\!I}$ in constant-property atmospheres (53; 212; 316). The source functions $S_i(v)$ and S_i^{CR} may also be used to compute line-profiles; the errors made in calculated profiles if complete redistribution is assumed in place of an accurate redistribution function can then be assessed. An intermediate approximation is the *iterated* source function

$$S_i^{(1)}(v) \equiv (1 - \epsilon)\phi_v^{-1} \int R(v', v) J_{v'}^{CR} dv' + \epsilon B_v \quad (13-94)$$

which is evaluated using the mean intensity obtained from the complete redistribution solution based on equation (13-93). It has been found that $S_i^{(1)}(v)$ in isothermal media is nearly equal to $S_i(v)$ (316), and obviously it is much simpler to compute.

Let us first consider the case of redistribution by Doppler shifts only—i.e., $R(v', v) = R_I(v', v)$. A number of solutions for $S_i(v)$ have been obtained (316) for both finite and semi-infinite isothermal media, assuming zero continuum opacity, with $\epsilon = 10^{-4}$ and 10^{-6} . Results for variation of the source function with frequency and depth are shown in Figure 13-6 for $\epsilon = 10^{-4}$. The vertical arrows designate the frequency at which the monochromatic optical depth $\tau_x = 1$. It is clear that, at all frequencies where $\tau_x \gtrsim 1$, $S_i(x)$ essentially equals S_i^{CR} ; large deviations occur when $\tau_x < 1$, but are of little consequence because these optically thin regions do not contribute significantly to the intensity in a line profile. In fact, the line profiles computed from S_i^{CR} and from $S_i(x)$ are virtually identical; hence we conclude that for Case I the scattering process is, for all practical purposes, adequately described by the simpler assumption of complete redistribution. A similar conclusion is reached (212) for the case of complete redistribution in the atom's frame—i.e., $R(v', v) = R_{III}(v', v)$. Here the iterated source function, equation (13-94), was evaluated in an isothermal semi-infinite atmosphere, for lines with $a = 10^{-3}$, and $\epsilon = 10^{-6}$ and 6×10^{-3} . Again it is found that $S_i^{(1)}(x)$ departs from S_i^{CR} only for $\tau_x < 1$, and that emergent line profiles computed from S_i^{CR} are almost identical to those computed from the frequency-dependent function. Thus the assumption of complete redistribution provides a very useful and accurate approximation for Case III as well.

The situation for Case II (coherent scattering in a broadened profile in the atom's frame with Doppler redistribution in the laboratory frame) is quite different. Results from an isothermal atmosphere of total thickness $T = 10^6$, for a line with $a = 10^{-3}$ and $\epsilon = 10^{-4}$, given in (316), are shown in Figure 13-7. Here we see that at line center, $S_i(v)$ is near S_i^{CR} for shallow optical depths, but rises above S_i^{CR} at great depth, and thermalizes to the Planck function sooner than the complete-redistribution source function. This result is obtained because the coherent nature of the scattering process in the line-wings inhibits photon escape from the line-core, and forces more

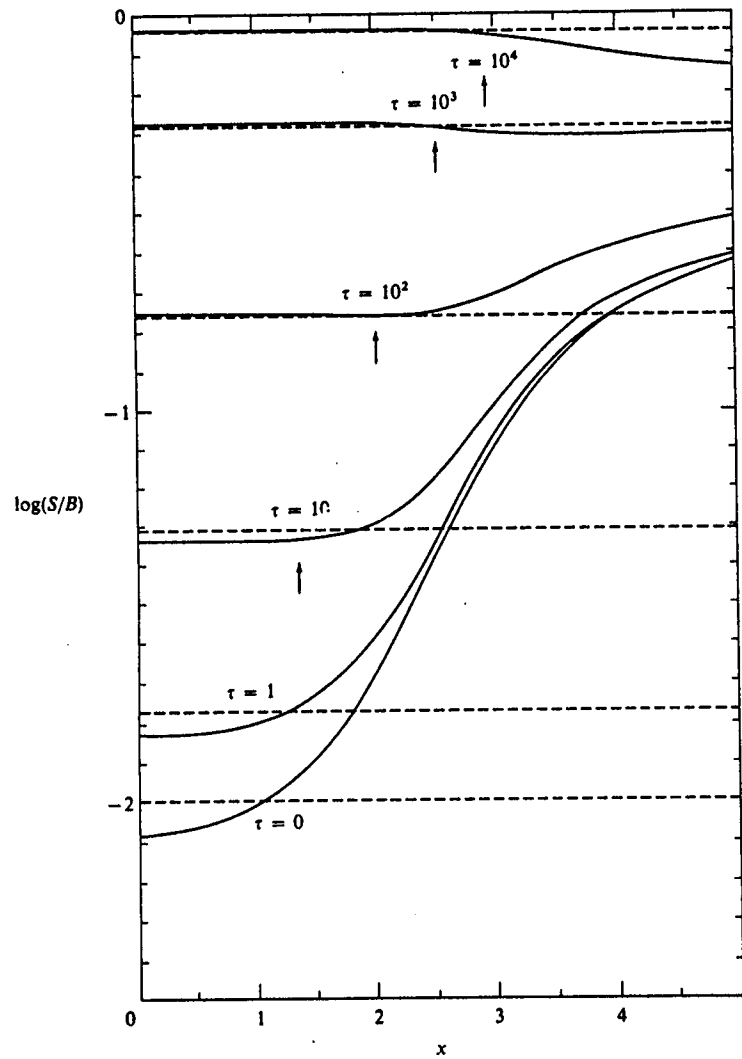


FIGURE 13-6
Source functions in an isothermal, semi-infinite atmosphere for a line with $\varepsilon = 10^{-4}$, assuming pure Doppler redistribution (case I). The vertical arrows show the frequency at which the monochromatic optical depth $\tau_x = 1$. Dashed curves: frequency-independent S_i^{CR} obtained assuming complete redistribution. Solid curves: frequency-dependent $S_i(x)$ obtained using correct redistribution function. Abscissa: displacement from line center in Doppler units. From (316), by permission.

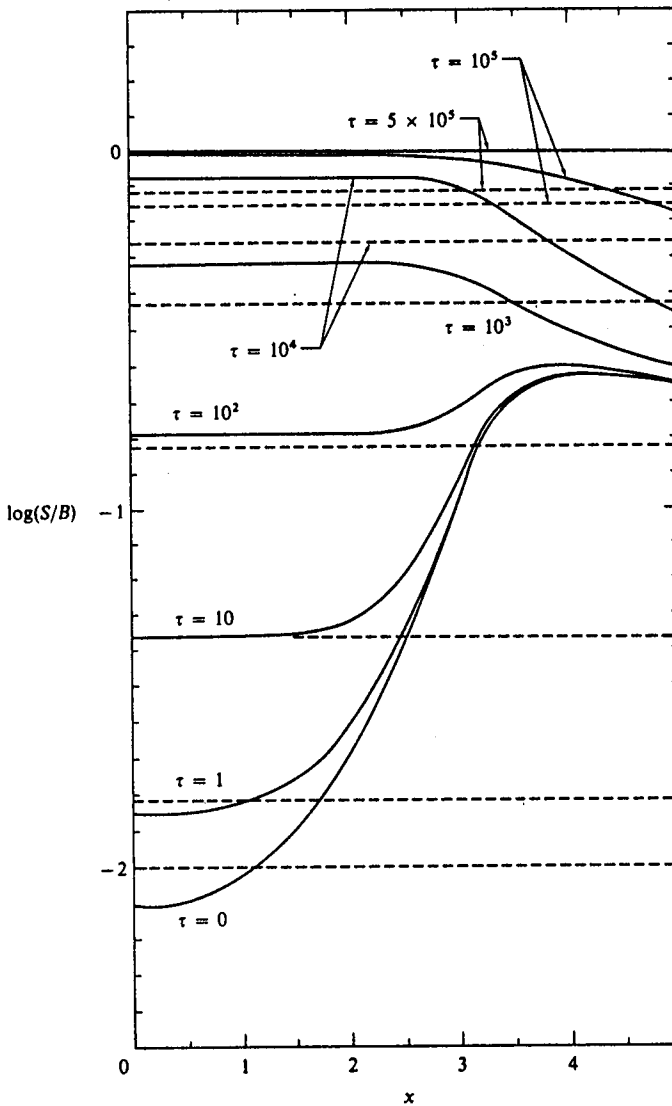


FIGURE 13-7
Source functions in an isothermal atmosphere of total thickness $T = 10^6$, for a line with $\varepsilon = 10^{-4}$ and $a = 10^{-3}$, assuming coherent scattering in a radiation-damping profile in the atom's frame, and Doppler redistribution in the laboratory frame. Dashed curves: frequency independent S_i^{CR} obtained assuming complete redistribution. Solid curves: frequency-dependent $S_i(x)$ obtained using correct redistribution function. Abscissa: frequency displacement from line-center in Doppler units. From (316), by permission.

rapid thermalization in the core by reducing the net escape probability for such photons. In contrast, in the line-wings, the frequency-dependent source function *lies substantially below* S_i^{CR} , because photons are no longer being fed into the wings from the core as efficiently. These effects are even more pronounced for finite atmospheres where S_i^{CR} may exceed $S_i(x)$ by orders of magnitude in the line wing! The emergent line profiles faithfully reflect the discrepancies between $S_i(x)$ and S_i^{CR} . Profiles for the correct source function have intensities that lie well below those for complete redistribution in the wings, and that nearly agree with the intensities predicted by coherent scattering. Although these effects will be diminished when there is an overlying continuum, we may, nevertheless, expect partial redistribution effects to be important for resonance lines formed in the outer layers of stars where densities, and thus collision rates, are low.

APPLICATION TO SOLAR AND STELLAR RESONANCE LINES

The resonance lines of many ions [e.g., those of hydrogen (particularly $L\alpha$), Ca^+ , and Mg^+] are formed in chromospheric layers of low density, and hence are rather well characterized by the redistribution function of equation (13-73) with γ almost unity. Several calculations have now been made for solar lines, using the HSRA (249) or related models, and for solar-type giants (where densities are even lower than in the sun) using realistic model atmospheres.

One of the first examples of the importance of partial redistribution effects in resonance-line formation arose from attempts to fit the observed solar chromospheric $L\alpha$ profile (645). It was found that when the line profile was computed under the assumption of complete redistribution, using models that provided accurate fits to the continuum data formed in the same atmospheric layers as the $L\alpha$ line-wing, the intensity in the calculated profile wing was *much* larger (by a factor of 5 to 6) than observed. From the first study (645) it emerged that a much better fit to the profile is obtained if the scattering is assumed to be about 93 percent coherent, and only 7 percent completely redistributed. Subsequent work showed (456) that this parameterization is equivalent to using equation (13-73) with realistic values of γ (determined from the known collisional and radiative rates), and finally, that when the full depth-dependence of the profile and redistribution functions, atomic rates, level populations, and background opacity are taken into consideration, an excellent fit to the observations is achieved (457).

An even more interesting example is provided by the solar $\text{Ca II } H$ - and K -lines, for which the earlier work (e.g., 401) assuming complete redistribution gives a good fit to the disk-center profiles, but fails to fit the observed center-to-limb variation. Calculations using a five-level atom similar to that shown in Figure 12-1 were made (570) [see also (642)] for three model atmospheres: (1) the HSRA with a depth-independent microturbulence of

4.5 km s^{-1} ; (2) the HSRA with the microturbulent velocity distribution given by (401); and (3) the same as model 1, but with the temperature structure modified to be $T_3 = \max(T_{HSRA}, 4450^\circ\text{K})$, which raises the temperature minimum by about 300°K . In all cases the full depth-variations of the line profile (allowing for radiation, van der Waals, and Stark broadening), the redistribution function, and background sources were taken into account.

The results from complete redistribution (CR) and partial redistribution (PR) computations of the double-reversal near line center (which provides vital information for diagnostics of the temperature-minimum region and the chromosphere) are strikingly different. As may be seen in Figure 13-8,

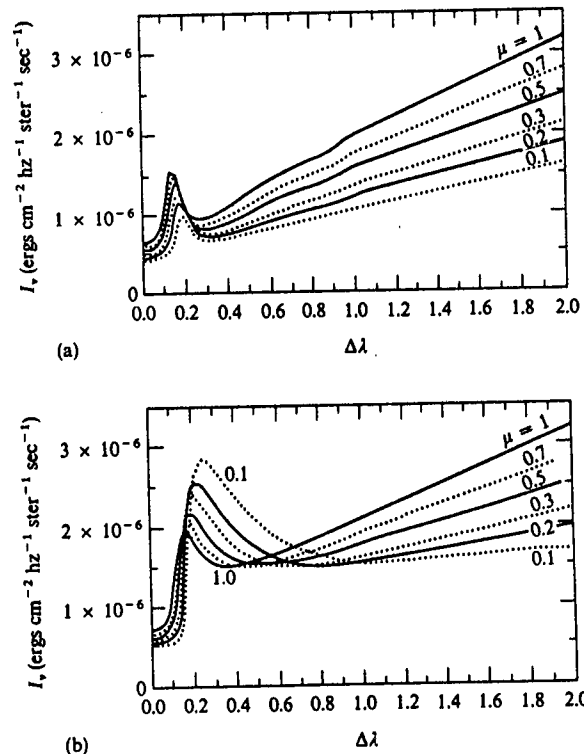


FIGURE 13-8
Ca II K -line profiles computed using the HSRA (249) model solar atmosphere with the distribution of microturbulent velocities given in (401). Ordinate: specific intensity $I(\mu, \Delta\lambda)$ in absolute units; abscissa: displacement $\Delta\lambda$ from line-center in Å. (a) Partial redistribution results; (b) complete redistribution results. Curves are labeled with μ , the cosine of the angle from disk center. From (570), by permission.

the PR profiles show uniform limb-darkening throughout the entire profile. In contrast, the CR results show limb-brightening at K_2 (the emission maximum) and no center-to-limb variation at K_1 (the minimum outside K_2); both of these results are contrary to observation. Furthermore, the wavelength position of the K_1 minimum shows a rapid center-to-limb increase for CR (again contrary to observation), while for PR the increase is much slower. The problem of limb-brightening of K_2 when CR is assumed can be overcome if a very special distribution of microturbulent velocities (27) is employed. However, neither of the problems just described for K_1 is eliminated in this way; moreover, the need for this special assumption is obviated when PR is employed.

The quantitative improvement in the comparison with the observed behavior of the K_1 feature is shown in Figure 13-9. There we see that CR produces much too rapid a rise in $\Delta\lambda(K_1)$ as $\mu \rightarrow 0$, while both models 1 and 3 yield an excellent fit to the data. Model 2 does not do as well, though it provides a better fit to certain data for K_2 (not discussed here). In part (b) of the figure we see that CR fails badly to fit the limb-darkening of K_1 intensity, while PR (with any of the three models) yields the correct center-to-limb variation (notice the logarithmic scale). Note that the absolute intensity of the K_1 feature is reduced by PR, relative to CR, for a given model (compare the open and filled circles at $\mu = 1$). This results from the essentially coherent nature of the scattering process in the K_1 feature, and is consistent with the results for R_{II} redistribution in the idealized models discussed above. One way to obtain a fit to the absolute intensity is to raise the temperature minimum by 300°K to 400°K over the HSRA value, as was done for model 3. While this change seemingly is small, it should be recalled that a change of about 100°K near T_{min} changes the energy content of that region by an amount comparable to the energy content of the entire corona (cf. §7-7.). One hesitates to conclude on the basis of one line that T_{min} must be higher than the HSRA model value; however, similar results are also obtained from an analysis of the Mg II h - and k -lines (59), and it may, in fact, be necessary to raise the empirical value of T_{min} to about 4400°K. Such an adjustment would bring the semiempirical result into harmony with the estimates of T_{min} from radiative equilibrium models, and would eliminate the difficulty described in §7-7. In any case it must be emphasized that the drop in intensity of PR relative to CR is a differential effect for a given model, and therefore will occur no matter what model is used. Thus if T_{min} is estimated from a fit to the K_1 intensity (as is sometimes done in stellar work), one must use a PR description of the scattering process, especially for giants (571), or systematic errors will be made. Finally, it is found that the PR calculation accurately reproduces the relative behavior of the H - and K -lines while CR does not.

The marked differences in the CR and PR predictions of limb-darkening and wavelength-position of K_1 can be easily understood in terms of the differences in the depth-variation of the source function S_l^{CR} , which is

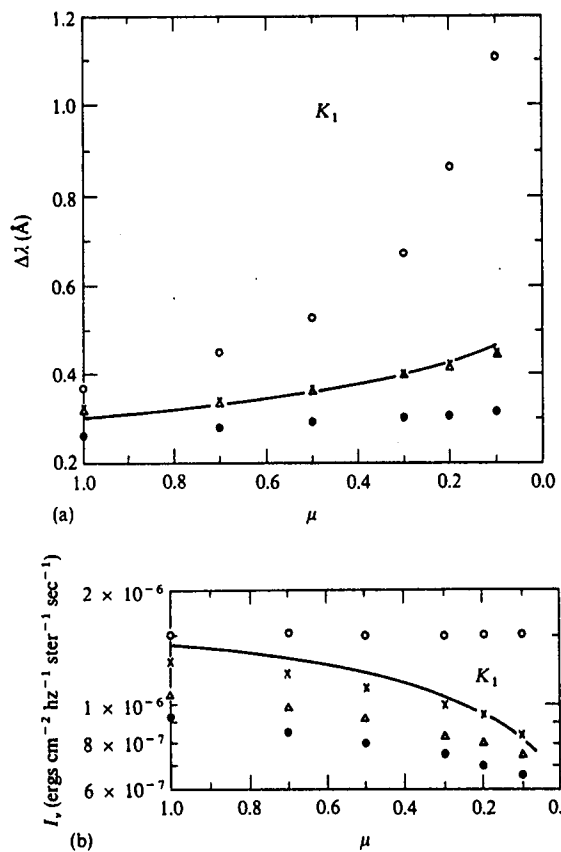


FIGURE 13-9
(a) Wavelength position of minimum intensity outside emission core, K_1 , as a function of μ , cosine of angle from disk center.
(b) Limb-darkening at K_1 ; note logarithmic units of intensity.
Open circles: complete redistribution results, model 2 (see text).
Filled circles: partial redistribution, model 2. Open triangles:
partial redistribution, model 1 (see text). Crosses: partial
redistribution, model 3 (see text). From (570), by permission.

frequency-independent, and the frequency-dependent PR source functions $S_l(v)$ shown in Figure 13-10. There we see that CR yields a unique source function that has a single absolute minimum. As one observes from center to limb, the slant-length optical depth at a particular frequency increases; if S_l^{CR} is used, this implies that the intensity at $\Delta\lambda_{K_1}(\mu = 1)$ must rise as μ decreases. The minimum S_l^{CR} will manifest itself only at some larger $\Delta\lambda$ where the material is more transparent and thus reflects the source function